

Shock Wave Modulation by Local-Disturbance/Turbulence

A dissertation submitted in partial fulfillment
for the requirement for the degree of doctor of engineering

Takahiro TAMBA

Department of Aerospace Engineering

Nagoya University

March 2018

Dissertation Committee

Akihiro Sasoh
Professor

Yasuhiko Sakai
Professor

Yoshiyuki Tsuji
Professor

Koichi Mori
Associate Professor

Akira Iwakawa
Lecturer

Acknowledgements

I would like to express my gratitude to my supervisor, Professor Akihiro Sasoh, who gave me guidance and encouraged me through my research for six years. He helped me to broaden my horizons as a researcher and to complete the present study. I am also deeply grateful to Lecturer Akira Iwakawa for his advice and encouragement, based on his experiences and PhD study. I sincerely appreciate the advice and suggestions from the manuscript committee members, Professor Yasuhiko Sakai, Professor Yoshiyuki Tsuji, and Associate Professor Koichi Mori. I owe my deep gratitude to researchers of National Institute of Advanced Industrial Science and Technology, who gave me valuable opportunities and advice, especially related to Chapter 3.

I would like to express my deep appreciation to Futamura Chemical Co. Ltd., who supported this study and provided the cellophane diaphragm that appears in Chapter 4.

I also thank all the members of Shock Wave and Space Propulsion Laboratory and Ionized Gas Dynamics Laboratory for enabling my study. I am especially indebted to Mr. Naoki Hasegawa, Mr. Takeshi Osuka, and Mr. Ryosuke Majima, who provided helpful advice and encouragement, and to Mr. Kenji Takeya, Mr. Tatsuya Harasaki, Mr. Tuan Nguyen Manh, Mr. Tatsuro Shoda, Mr. Son Pham Hoang, Mr. Masaya Kayumi, and Mr. Gaku Fukushima, who paid many efforts for the previous studies and cooperated on my work.

Finally, I would like to show my greatest appreciation to my family for their kind support, understanding, and encouragement.

Takahiro Tamba

Contents

List of Published Papers	iv
List of Figures.....	v
List of Tables	ix
Chapter 1 Introduction.....	1
1.1 Aerodynamic problems related to shock wave modulation	1
1.2 Elements of shock wave modulation and related works.....	3
1.2.1 Density/temperature disturbance	3
1.2.2 Velocity disturbance	5
1.3 Objective and structure of this thesis.....	8
Chapter 2 Effect of local disturbance on shock wave-boundary layer interaction.....	11
2.1 Study targets of shock wave-boundary layer interaction.....	11
2.1.1 Features of shock wave-boundary layer interaction	11
2.1.2 Control of shock wave-boundary layer interaction	15
2.1.3 Focus point of this chapter	16
2.2 Experimental setup	17
2.2.1 Apparatus.....	17
2.2.2 Method of spectral analysis	20
2.3 Effect of local disturbance on shock wave oscillation	22
2.3.1 Basic flow characteristics	22
2.3.2 Effect of local disturbance frequency	26
2.4 Summary of this chapter.....	31
Chapter 3 Overpressure modulation behind blast wave by local turbulent flow.....	32
3.1 Shock wave-turbulence interaction	32
3.1.1 Effect of turbulence on shock wave	32
3.1.2 Existing methods of shock wave-turbulence interaction study	35
3.1.3 Features of blast wave	38

3.2	Experimental setup	40
3.2.1	Apparatus.....	40
3.2.2	Characteristics of turbulence	44
3.2.3	Pressure signal correction.....	47
3.3	Effect of local turbulent flow on overpressure behind blast wave	52
3.3.1	Effect on pressure waveform.....	52
3.3.2	Evaluation of reproducibility and error of setup	55
3.3.3	Effect on standard deviation of peak overpressure.....	58
3.4	Summary of this chapter.....	61
Chapter 4 Development of counter-driver shock tube and planar shock wave-grid turbulence interaction		62
4.1	Method to investigate interaction between planar shock wave and isotropic turbulence	62
4.2	Operation principle of counter-driver shock tube.....	64
4.3	Technical details	69
4.3.1	Diaphragm rupture.....	69
4.3.2	Weakening of interacting shock wave	71
4.3.3	Calibration of hot-wire anemometer.....	73
4.4	Operation performance	75
4.4.1	Proof of principle.....	75
4.4.2	120 mm × 120 mm square counter-driver shock tube	81
4.5	Interaction between planar shock wave and grid turbulence.....	84
4.5.1	Experimental condition.....	84
4.5.2	Side view thickness of shock wave region	86
4.6	Summary of this chapter.....	91
Chapter 5 Conclusions.....		93
References		96

List of Published Papers

Chapter 2

Tamba, T., Pham, H. S., Shoda, T., Iwakawa, A., Sasoh, A., “Frequency modulation in shock wave-boundary layer interaction by repetitive-pulse laser energy deposition,” *Physics of Fluids*, vol. 27 (9), 091704, 2015.

Chapter 3

Tamba, T., Furukawa, D., Aoki, Y., Kayumi, M., Iwakawa, A., Sasoh, A., Matsunaga, T., Izumo, M., Sugiyama, Y., Matsumura, T., Nakayama, Y., “Field experiment of blast wave pressure modulation past a turbulent flow,” *Science and Technology of Energetic Materials*, vol. 77, No. 4, pp. 91-97, 2016.

Chapter 4

Tamba, T., Nguyen, T. M., Takeya, K., Harasaki, T., Iwakawa, A., Sasoh, A., “Counter-driver shock tube,” *Shock Waves*, vol. 25 (6), pp. 667-674, 2015.

List of Figures

Figure 2.1	Typical flow structures of the shock wave-boundary layer interaction in two-dimensional configurations.	14
Figure 2.2	Experimental apparatus.	19
Figure 2.3	Brightness history at uniform flow $(r, z) = (11 \text{ mm}, -1.7 \text{ mm})$, corresponding to Fig. 2.5 (raw data); red line is the line of best fit, found by the least squares method; processed data is the difference between raw data and the line of best fit.	21
Figure 2.4	Power spectrum density at uniform flow, corresponding to raw data and processed data in Fig. 2.3.	21
Figure 2.5	Schlieren images, without local disturbance (basic flow).	24
Figure 2.6	Power spectrum distributions, w/o local disturbance (basic flow).	25
Figure 2.7	Distributions of power spectrum density along $r = 9 \text{ mm}$, the dashed line in Fig. 2.5, w/o local disturbance (basic flow).	25
Figure 2.8	Schlieren images, w/ local disturbance by pulsed laser energy deposition; frequency of local disturbance, f_d	29
Figure 2.9	Power spectrum distributions, w/ local disturbance; frequency of local disturbance, f_d ; the contour levels are common to Fig. 2.6.	30
Figure 2.10	Distributions of power spectrum density along $r = 9 \text{ mm}$, the dashed line in Fig. 2.8, w/ local disturbance; frequency of local disturbance, f_d ; the contour levels are common to Fig. 2.7.	30
Figure 3.1	Typical waveform of blast wave.	40
Figure 3.2	Experimental setup.	42

Figure 3.3	Image of experimental field.	42
Figure 3.4	Image of blast wave source.	43
Figure 3.5	Square grid, solidity = 36%.	43
Figure 3.6	Arrangement of microphones, A-A cross section ($x = 500$ mm) in Fig. 3.2, 1 to 4 are microphone numbers.	43
Figure 3.7	Image of Arrangement of microphones, 1 to 4 are microphone numbers..	43
Figure 3.8	Characteristics of turbulence in x direction at the position of microphone 1; (a) time-averaged flow velocity, \bar{u} , (b) rms velocity fluctuation, u' , (c) integral length scale; horizontal axis x is the distance from the nozzle of turbulence generator.	46
Figure 3.9	Waveform of planar shock wave measured by microphone, $y_0(t)$	51
Figure 3.10	Typical example of blast wave measured in the case without flow; processed waveform is recovered from rough waveform by deconvolution. ...	54
Figure 3.11	Typical examples of processed pressure waveforms in one shot (with turbulence); dashed lines are rough waveforms, 1 to 4 correspond to microphone numbers in Fig. 3.6, each signal are displaced in y -direction by 0.6 kPa.	54
Figure 3.12	Distribution of standardized peak overpressure, $\Delta\overline{P}(i,j)$; the standard deviation of standardized peak overpressure, $\tilde{\sigma}_i$; j corresponds to microphone numbers in Fig. 3.6.....	60
Figure 4.1	Configuration and operation of counter-driver shock tube; left-(driver/driven), L-; right-(driver/driven), R-; incident shock wave, iSW; transmitted shock wave, tSW; contact surface, CS; post-shock flow, PSF.	68
Figure 4.2	Contours of counter flow speed, u_{2L} , and shock Mach number, M_s , on $P_{4L}/P_1 - P_{4R}/P_{4L}$ coordinates; $\gamma_{4L} = \gamma_1 = \gamma_{4R} = 1.4$, $a_{4L} = a_1 = a_{4R} = 340$ m/s.	

.....	68
Figure 4.3 Pneumatic diaphragm rupture device; length of connection tube, l_t	71
Figure 4.4 Overpressure histories obtained in preliminary experiment of weak planar shock wave generation, using R-Driver and Driven section of 120 mm \times 120 mm square CD-ST described in Section 4.4.2; porous wall was installed at $x = 5020$ mm; $P_{4R} = 50.0$ kPa, $P_1 = 43.0$ kPa.....	73
Figure 4.5 Examples of calibration curves for each T_2 , calibrated by shock waves with the shock Mach numbers of 1.05 and 1.10.....	75
Figure 4.6 Counter-driver shock tube system; pressure transducers, G1 to G6; relative delay time from L-Driver to R-Driver actuations, τ	78
Figure 4.7 Example of $x-t$ diagrams of individual driver operation; solid lines are calculated from ideal shock tube relation; cross symbols are measured.....	79
Figure 4.8 Example of $x-t$ diagram of counter-driver operation; $P_{4L} = 43.4$ kPa, $P_1 = 36.9$ kPa, $P_{4R} = 129.3$ kPa; incident and reflected expansion fans, iEF and rEF; the states in the boxes corresponds to those in Fig. 4.1; A, B, C, refer to those in Fig. 4.9; cross symbols are measured; lines are drawn based on the ideal shock tube relation.....	79
Figure 4.9 Overpressure histories measured at G2, G3, and G5 in demonstration experiment shown in Fig. 4.8 (A, B, C, refer to those in Fig. 4.8).....	80
Figure 4.10 120 mm \times 120 mm square counter-driver shock tube, electric circuit corresponds to Fig. 4.6.	83
Figure 4.11 Top view of optical system of shadowgraph/Schlieren visualization (shock tube is described in side view to indicate the position of the visualization window).....	83

Figure 4.12	Square grid, solidity = 30.6%.....	83
Figure 4.13	Example of $x-t$ diagram of an interaction experiment between planar shock wave and grid turbulence (Case 1, see Table 4.1); $P_{4L} = 68.0$ kPa, $P_1 = 43.0$ kPa, $P_{4R} = 50.0$ kPa; shock Mach number of R-tSW, $M_s = 1.01$; turbulent Mach number, $M_t = 6 \times 10^{-3}$ (estimation); interaction length, $L_i = 108$ mm; solid lines are calculated from an ideal shock tube relation; cross symbols are measured.....	85
Figure 4.14	Shadowgraph images of Case 1; $M_s = 1.01$, $M_t = 6 \times 10^{-3}$ (estimation), “broken shock” criteria was satisfied; interaction length, L_i	90
Figure 4.15	Shadowgraph images of Case 2; $M_s = 1.18$, $M_t = 6 \times 10^{-3}$ (estimation), “broken shock” criteria was not satisfied; interaction length, L_i	90
Figure 4.16	Schlieren images of Case 3; $M_s = 1.02$, $M_t = 23 \times 10^{-3}$ (estimation), “broken shock” criteria was satisfied; interaction length, L_i	90
Figure 4.17	Relationship between interaction length, L_i , and average of side view thickness of shock wave region; $M_t = 6 \times 10^{-3}$ (estimation).....	91

List of Tables

Table 3.1	Experimental conditions.	44
Table 3.2	Characteristics of turbulence in same plane, $x = 500$ mm.	46
Table 3.3	Nomenclatures in deconvolution process.	51
Table 3.4	Histories of average of overpressures in i -th shot, $\overline{\Delta P(i)}$; serial shot number, i	57
Table 3.5	Average overpressure in a day, $\overline{\Delta P}$, and standard deviation caused by reproducibility, σ_s	57
Table 4.1	Experimental conditions; turbulent Mach numbers, M_t , were estimated from an assumption of a proportional relationship between $\overline{u_{2L}}$ and u'_{2L}	86

Chapter 1

Introduction

1.1 Aerodynamic problems related to shock wave modulation

In compressible fluid dynamics and associated applications, there exist many unsolved problems related to shock waves, behind which high pressure fields follow. For example, an airplane in supersonic flight generates shock waves around its body. Although demands for sustainable commercial supersonic transport are increasing in the rapidly growing air transportation, problems caused by the generation of the shock waves interfere with its development. For fundamental research, it is required to understand the behavior of shock wave and the variation in pressure behind it correlated to the motion of shock wave under relevant fluid dynamics conditions. In addition, based on the knowledge, it is also an important subject to develop the methods to improve the associated aerodynamic performance. Currently, two main problems related to compressible fluid dynamics prevent the realization of the next generation supersonic transport. One of these problems is poor fuel consumption efficiency due to large wave drag (Bushnell, 2003) and inadequate engine performance (Strack and Morris, 1988). Wave drag is particular to supersonic flight because it is induced by a high pressure field behind the shock waves over the airplane body. Because airflow into engines of the airplane is decelerated and compressed through shock waves appearing at its engine intake, engine performance in supersonic flight is also closely related to the behavior of

the shock waves (Gnani et al., 2016). The other problem is the generation of sonic boom, which causes an intense noise when the shock wave propagates to the ground (Maglieri et al., 2014). Some field measurements reported that the noise level of the sonic boom was affected by natural conditions of the atmosphere, including temperature and velocity disturbances (Hubbard et al., 1964; Kane, 1967); therefore, the sonic boom evaluation under the actual atmospheric conditions has a considerably high priority as well as its mitigation.

Another example of the problems related to shock waves is the evaluation of the aerodynamic impacts of explosion over the surroundings, which include architecture and human bodies. As is known well, shock wave generated by an explosion damages the structures of buildings and human tissues, especially the brain and lungs (Ullah et al., 2017; Plurad, 2011). Even in the far field, it causes a broad range of damage to the society (Needham, 2010). The pressure behind shock wave can be affected by fluctuations in the ambient atmosphere, which are usually present in a random manner. To evaluate and suppress such hazards in the far field, it is necessary to investigate the effects of random disturbances on the pressure field behind the shock wave. This problem shares a common fluid dynamics feature with the sonic boom problem as the sonic boom induced by a supersonic airplane is greatly influenced by natural atmospheric turbulence. To tackle these problems, they are defined from the common viewpoints of compressible fluid dynamics.

The common feature underlying these problems is the relationship between the behavior of a shock wave and the modulation of pressure behind it. Hereafter, in this thesis, this problem will be referred to as “shock wave modulation.” Behind a shock wave, a high pressure field, which is “post-shock pressure,” exists. The pressure ratio of the

post-shock pressure to the pressure in front of the shock wave is determined by a “shock Mach number,” which is the Mach number of the shock wave relative to the flow in front of it (Landau and Lifshitz, 1987). A high post-shock pressure can cause a large sonic boom and poor aerodynamic performance in supersonic transport, as well as severe damages from the explosion.

In principle, such a post-shock pressure can be modulated by introducing a disturbance to the shock wave system. It is irrelevant whether this disturbance is natural in fluid dynamics or artificial. Under certain circumstances, a disturbance can increase the complexity of the phenomenon, while in other cases it can be used to control the shock wave flow. Therefore, it is important to investigate the interaction between shock wave and characterized disturbance in a quantitative manner, in order to resolve the aerodynamics problems mentioned above. In the following section, we categorize disturbances into two elements, which are density/temperature and velocity disturbances, in terms of their characteristics.

1.2 Elements of shock wave modulation and related works

1.2.1 Density/temperature disturbance

One of the elements that affect shock waves is density/temperature disturbance. Under a constant pressure, density and temperature are related by an equation of state and cannot be separated as independent parameters. The density/temperature disturbance appears when a gas is heated by inputting energy to it. As the speed of sound is proportional to the square root of the temperature of its medium, it is higher in a locally-heated region than in the surroundings.

When a shock wave interacts with a locally-heated region, the shock wave deforms due to the difference of the propagation speeds inside and outside of the region, thus mitigating post-shock pressure. Hence, previous studies reported that wave drag caused by the high post-shock pressure could be reduced by the interaction with local heated regions, which could be generated by discharge (Satheesh and Jagadeesh, 2008; Schulein et al., 2011; Erdem et al., 2013) or laser energy deposition (Sperber et al., 2012; Hong et al., 2014). The mitigation of post-shock pressure can be also achieved using local density/temperature gradient. The region with a local density/temperature gradient obtains vorticity by the interaction with the shock wave, thus mitigating the post-shock pressure associated with the deformation of the shock wave (Adelgren et al., 2005; Kim et al., 2011). Although a large effect on the post-shock pressure modulation can be expected by the interaction, the effectiveness of the modulation should be considered because the huge power input to the gas causes an increment of fuel consumption.

Introduction of density/temperature disturbance is also investigated as a method of local flow control using the shock wave interaction. Girgis et al. reported the possibility to input steering moment to a vehicle using the modulation of the post-shock pressure caused by the interaction with local heated region (Girgis et al., 2006). This effect can be applied to the sonic boom problem. The mitigation of the sonic boom by the interaction with local heated region was experimentally and numerically demonstrated by Furukawa et al. and Potapkin and Moskvichev, respectively (Furukawa et al., 2016; Potapkin and Moskvichev, 2014). Moreover, the interaction with the density/temperature disturbance is effective to control the shock wave-boundary layer interaction, which is described in the next section. Osuka et al. input local density/temperature disturbance generated by repetitive pulsed laser energy deposition to the shock wave-boundary layer interaction

region (Osuka et al., 2014). They showed the capability of laser energy deposition to suppress the separation caused by the shock wave-boundary layer interaction.

1.2.2 Velocity disturbance

Velocity disturbance is another element which can cause the shock wave modulation. When the local flow velocity upstream of a shock wave varies, the relative shock Mach number also varies, thus causing post-shock pressure modulation. Velocity disturbance can be classified into two types: gradual and methodical flow velocity change, and velocity fluctuation with random behavior. We can point to the boundary layer as an example of the former, and turbulence as the latter.

In the boundary layer developed over a wall in supersonic flow, even a subsonic region can appear near the shock wave. In this case, a strong interaction, called “shock wave-boundary layer interaction,” appears and the shock wave terminates at a sonic point (Dolling, 2001; Clemens and Narayanaswamy, 2014). The interaction induces an adverse pressure gradient and causes boundary layer separation. The motion of the separated region and that of the shock wave couple each other, and the shock wave oscillates at relatively low frequency, which is characterized by the Strouhal number of 0.01 to 0.03 (Erengil and Dolling, 1991a and 1991b; Dussauge et al., 2006; Clemens and Narayanaswamy, 2014). The motions of the separated region and the associated shock wave are affected by the upstream and downstream flow states (Souverain et al., 2010b). In the strong interaction, which consists of a fully separated flow with a large recirculation region, the motion of the interacted region is dominated by the instability of the downstream separated flow. In the weak interaction, in which the separated region is small

or does not appear, the motion is correlated with the structure of the upstream turbulent boundary layer. The clear origin of such low frequency unsteadiness has not yet been revealed because it is difficult to distinguish the two effects of the upstream and downstream flows.

Another topic related to the shock wave-boundary layer interaction is its control. The shock wave-boundary layer interaction is caused by the velocity disturbance due to the boundary layer; however, it can be controlled by introducing artificial disturbances in the upstream boundary layer. For the purpose of controlling the shock wave-boundary layer interaction, the performance of various devices attached on the wall to passively generate disturbances in the upstream boundary layer have been investigated: cavity (McCormick, 1993), vortex generators (McCormick, 1993; Barter and Dolling, 1995 and 1996), and micro-ramps (Saad et al., 2012). Because the effectiveness of these passive methods is limited, active control methods have been investigated for further capability. Some researchers have succeeded in weakening the separation shock wave using localized arc filament plasma actuators (Webb et al., 2013; Quan et al., 2014) and pulsed arc discharge (Wang et al., 2009). In terms of the effect on the oscillation frequency of the shock wave, the availabilities of air jet vortex generators (Souverein et al., 2010a) and a pulsed-plasma-jet vortex generator driven by discharge (Narayanaswamy et al., 2012) were reported. Although the main function of these control methods was to introduce velocity disturbance, they also have an aspect of density/temperature disturbance. These control mechanisms have also been investigated; however, there remain some difficulties because of the complex nature of the shock wave-boundary layer interaction.

Velocity disturbance can also appear in a free field. A local jet formed in uniform flow is also a result of velocity disturbance and affects the characteristics of the shock

wave. The local jet has two aspects: inducements of mean flow velocity and velocity fluctuation. When we focus on the mean flow velocity of the local jet, it causes local variation in the relative shock Mach number in the jet and outer flow. Ribner et al. observed the modulation of the waveform due to the interaction with the local jet (Ribner et al., 1973). They also reported that the modulation of the overpressure and the rising time of the shock wave depended on the direction of the jet, which corresponds to the variation in the relative shock Mach number.

Turbulence is one type of velocity disturbance and is associated with random motion of the fluid. The interaction with velocity fluctuation in turbulent flow, including that in the local jet, leads to the mutual modulation of not only the shock wave but also the turbulence. From the view of the effect on the turbulence, Kitamura et al. conducted an interaction experiment between grid turbulence and a spherical shock wave (Kitamura et al., 2017). Barre et al. investigated the interaction with a planar shock wave generated by the Mach effect in a supersonic wind tunnel on compressible grid turbulence (Barre et al. 1996 and 1998). A shock tube was also applied for the investigations of the interaction between planar shock waves and grid turbulence (Keller and Merzkirch, 1990; Honkan and Andreopoulos, 1992; Honkan et al., 1994; Agui et al., 2005). These studies reported the effects of the interaction on the characteristic scales and the root-mean-square (rms) velocity fluctuation of turbulence. For the effect of the interaction on the shock wave, some experimental studies can be cited. Lipkens and Blackstock reported that the rise time and the distribution of the peak overpressures of the shock wave increased as a result of the interaction with velocity fluctuation (Lipkens and Blackstock, 1998). From the Schlieren visualization of the interaction, Kim et al. obtained a correlation between the modulation of the peak overpressure and that of the wave front of the shock wave (Kim

et al., 2010). Dosanjh reported that the wave front of the planar shock wave fluctuated by the interaction with grid turbulence using shadowgraph visualization (Dosanjh, 1956). Xanthos et al. showed that the variation of the post-shock pressure of the planar shock wave increased by the interaction with grid turbulence (Xanthos et al., 2002). Sasoh et al. and Inokuma et al. found a correlation between the modulation of the peak overpressure of the shock wave and the characteristics of grid turbulence (Sasoh et al., 2014; Inokuma et al., 2017). These studies reported that the interaction with velocity fluctuation caused the modulation of the post-shock pressure and the associated shock wave front; however the quantitative investigation of this effect on shock wave has not been performed yet due to limitations of the experimental setup. In recent years, some studies using direct numerical simulation reported that significant modulation of the shock wave front with topology change could occur when a relatively weak shock wave interacted with isotropic turbulence (Lee et al., 1993; Larsson and Lele, 2009; Larsson et al., 2013). These modulations were calculated on the conditions which are nearly beyond the scope of the previous experimental investigations; hence, it is necessary to expand the experimental condition and to evaluate the effect of turbulence interaction on the shock wave.

1.3 Objective and structure of this thesis

The results of the previous studies showed that a shock wave was greatly modulated when it interacted with density/temperature or velocity disturbances. These interactions increase the complexity of the phenomena related to the shock wave, and thus increase the difficulty in solving the engineering problems mentioned above. On the other hand, however, the previous studies also suggested the possibility to control the post-shock

pressure using the interactions between shock wave and disturbance. Therefore, to resolve the shock-related problems, it is necessary to evaluate the impact of the interactions with disturbances on the shock wave modulation.

The objective of the present thesis is to investigate the modulations of the shock wave front and the pressure field behind it in the presence of local disturbance or turbulence. In Chapters 2 to 4, the effects of various types of disturbances on shock waves are experimentally evaluated by changing their characteristics.

In Chapter 2, the effects of local disturbance on the shock wave-boundary layer interaction are investigated. In this research, the shock wave naturally oscillates on a laboratory coordinate system by the interaction with the boundary layer, similar to the previous studies (Erengil and Dolling, 1991a and 1991b; Dussauge et al., 2006). Local density/temperature and velocity disturbance is input only at a single location with a single repetition frequency to the upstream boundary layer of the interaction region. The interaction is strongly affected by the upstream flow state in the weak interaction (Souverein et al., 2010b); therefore, the effect of the artificial disturbance on the oscillation frequency of the shock wave is evaluated.

In Chapter 3, the overpressure modulation behind the blast wave by a local turbulent flow is investigated. In this chapter, the element of disturbance is velocity fluctuation that is input in a local region using a simple fan and grid combination; its effects on the pressure field behind a weak blast wave are investigated. The blast wave is propagated across a relatively long distance in the order of several meters in an outdoors field to weaken the shock wave and minimize the curvature effects. As a result, in this study the “broken shock” criteria proposed in the numerical study (Larsson et al., 2013) is almost satisfied with a quasi-planar blast wave.

Chapter 4 describes the development of a counter-driver shock tube to investigate planar shock wave and grid turbulence interaction. A new facility called a “counter-driver shock tube,” which has two counter-driver sections, is developed. Shock wave generation with temporal control is achieved by an active rupture system using a pneumatic cylinder, and operation test of the counter-driver shock tube is conducted. In this facility, planar shock wave-grid turbulence interaction, which is suitable for quantitative investigation, can be conducted under various conditions: not only the strengths of the shock wave and grid turbulence, but also the interaction length, which has not been focused on in both experimental and numerical studies (Dosanjh, 1956; Larsson et al., 2013). Using the counter-driver shock tube, the effects of quasi-isotropic velocity disturbance, i.e. grid turbulence, on the wave front of a planar shock wave are investigated.

Chapter 2

Effect of local disturbance on shock wave-boundary layer interaction

2.1 Study targets of shock wave-boundary layer interaction

The shock wave-boundary layer interaction often occurs on airplanes and rockets in supersonic/hypersonic flights. The interaction induces unsteady behaviors of the shock wave and causes many aerodynamic problems, such as local thermal/structural load, buffet on the airfoil, and unsteady flow in the supersonic/hypersonic engine intake (Clemens and Narayanaswamy, 2014). To resolve the problems, the characteristics of the shock wave-boundary layer interaction as well as its control methods has been investigated for over 50 years.

2.1.1 Features of shock wave-boundary layer interaction

Figure 2.1 shows typical flow structures of the shock wave-boundary layer interaction in two-dimensional configurations: compression ramp and reflected shock wave. Although the shock wave-boundary layer interaction appears in various configurations, such as two/three-dimensional compression ramp, sharp/blunt fin, and reflected shock wave, the natural physics is common for each configuration (Clemens and Narayanaswamy, 2014). Therefore, the flow structure of the interaction is described based on the compression ramp configuration (Fig. 2.1 (a)). Here, the shock wave is fixed on a

laboratory coordinate system. In supersonic flow, the convection of streamlines, which is caused by a ramp in this case, generates an oblique shock wave referred to as “ramp-induced shock wave.” The strength of the ramp-induced shock wave is determined by the flow Mach number, M_∞ , and the angle of the ramp. The boundary layer developed over the wall because of viscosity. The flow velocity in the boundary layer is relatively low, and even subsonic region exists. Therefore, the subsonic region in the boundary layer propagates the high-pressure field behind the ramp-induced shock wave upstream. Because it enhances the inverse pressure gradient in the boundary layer, the high pressure due to the ramp-induced shock wave can cause boundary layer separation with the recirculation motion of the trapped fluid. The separated region also bends the streamline upward and forms a separation shock wave, which is partially integrated with the ramp-induced shock wave. As the relative shock Mach number of the separation shock wave becomes less than one near the wall because of the low-speed boundary layer, the “shock foot,” which is the closest point of the separation shock wave to the wall, is degenerated into compression waves. The similar structure appears in the reflected shock wave configuration (Fig. 2.1 (b)). In this case, an incident shock wave from a wedge reflects on the wall and forms a reflected shock wave, which induces the separation by the interaction with the boundary layer.

As a remarkable feature of the shock wave-boundary layer interaction, it was reported that the separation shock wave oscillates with the pulsation of the separated region (Erengil and Dolling, 1991a and 1991b; Dussauge et al., 2006; Souverein et al., 2010b). This unsteady motion can be characterized by the low-frequency motion of the shock wave, known as the low-frequency unsteadiness (Clemens and Narayanaswamy, 2014). The dominant frequency of the shock wave oscillation is one or two orders lower

than that of the pressure fluctuation of the upstream turbulent boundary layer and the downstream separated flow, and the spectrum of the low-frequency oscillation spreads in a relatively broad band (Erengil and Dolling, 1991a). Further, the length amplitude of the shock wave oscillation is correlated to the oscillation peak frequency, such that the unsteady motion can be characterized by the Strouhal number of 0.01 to 0.03 regardless of the configuration (Clemens and Narayanaswamy, 2014). However, the origin of the low-frequency motion has not been understood well.

To reveal the origin of the low-frequency unsteadiness, many studies have been conducted. The possible causes of the low-frequency unsteadiness are from the upstream boundary layer and the downstream separated flow. Erengil et al. reported a correlation between the motion of the shock wave and the pressure variations in the upstream boundary layer (Erengil et al., 1991b). They also found that the motion of the separation shock wave correlated with the ensemble-averaged pressure histories in the separated flow (Erengil et al., 1991a). Beresh et al. obtained a correlation between the velocity fluctuation in the upstream boundary layer and the shock wave motion: the positive velocity fluctuation correlated with the downstream shock motion, and vice versa (Beresh et al., 2002). Dupont et al. reported the strong coherence between the low-frequency pressure fluctuation of the shock foot and the pressure fluctuation near the reattached point located downstream of the separated region (Dupont et al., 2006). They also suggested that the three-dimensional structures of the separation can affect the unsteadiness. Ganapathisubramani et al. also found a correlation between the velocity fluctuation in the upstream boundary layer and the separation point fluctuation, which represented the shock wave motion (Ganapathisubramani et al., 2009). Estruch et al. showed that the dominant frequency of the pressure fluctuation in the separated region

was relatively high, which was in the same order of that in the upstream boundary layer (Estruch et al., 2010). Therefore, they suggested that the low-frequency unsteadiness was caused by the separation mechanism of the upstream boundary layer. Souverein et al. concluded that the primary driving source of the low-frequency motion depended on the strength of the interaction: the weak interaction and the strong interaction (Souverein et al., 2010b). In the weak interaction, in which no separation or small separated region existed, the motion was correlated with the fluctuation in the upstream turbulent boundary layer. In the strong interaction, in which large separated region existed, the instability in the downstream separated flow became predominant. For the latter case, Pirozzoli and Grasso investigated the reflected shock wave configuration using direct numerical simulation (Pirozzoli and Grasso, 2006). They suggested the existence of a feedback mechanism driven by acoustic waves, which were generated by the interaction between the incident shock wave and the separated flow. However, it is difficult to identify the origin of the low-frequency unsteadiness, especially in strong interaction because the behavior of the downstream separated flow is also affected by the upstream condition.

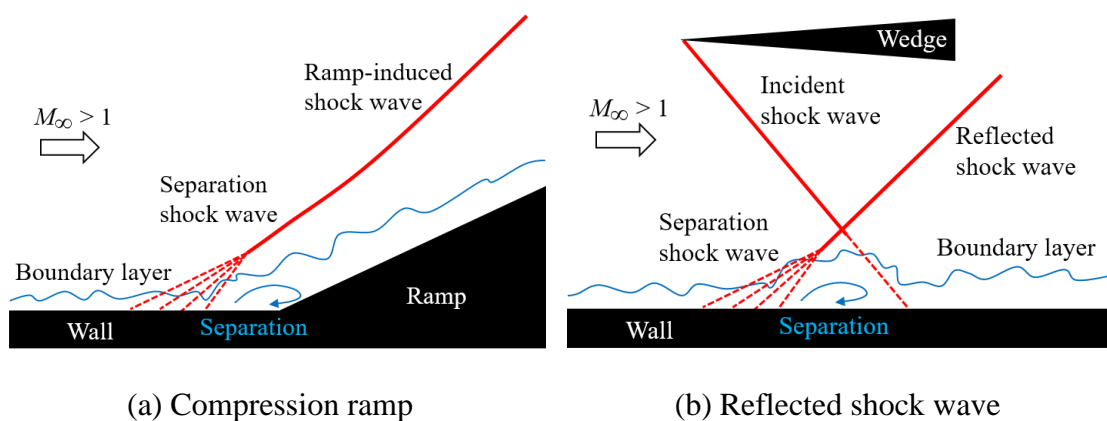


Figure 2.1 Typical flow structures of the shock wave-boundary layer interaction in two-dimensional configurations.

2.1.2 Control of shock wave-boundary layer interaction

To control the shock wave-boundary layer interaction, researchers have examined the control performance of passively generated upstream disturbances by attaching devices in the upstream boundary layer. McCormick et al. installed a passive cavity in the upstream boundary layer and reported the reduction in the total pressure loss through the shock system. (McCormick, 1993). They also showed that the vortex generators in the upstream boundary layer suppressed the separation caused by the interaction. Barter and Dolling attached vortex generators in the upstream boundary layer (Barter and Dolling, 1995 and 1996). They reported that the device reduced the length amplitude of the separation shock oscillation and the pressure fluctuation near the separation point. In this study, they also showed that the oscillation frequency of the shock wave was modulated to a higher frequency by the vortex generators. Saad et al. installed micro-ramps in the upstream boundary layer and performed the suppression of the flow separation caused by the shock wave-boundary layer interaction (Saad et al., 2012). Although these passive methods can modify the flow field, they have limited effectiveness: they perform well in a limited, specific condition, and the amplitude of the disturbances cannot be tuned to the flow conditions.

In contrast, active control methods to artificially supply upstream disturbances such as energy deposition and jet injection are more flexible in terms of flow control. Webb et al. and Quan et al. installed localized arc filament plasma actuators in the shock wave-boundary layer interaction region (Webb et al., 2013; Quan et al., 2014). Wang et al. implemented pulsed arc discharge to control the interaction region (Wang et al., 2009). By using these devices, the weakening of the separation shock wave was reported. Souverein et al. installed air jet vortex generators in front of a boundary layer separation

point, and reported that the oscillation frequency of the shock wave was increased by 50% (Souverein et al., 2010a). Using a pulsed-plasma-jet vortex generator driven by discharge, Narayanaswamy et al. modulated the shock wave oscillation to the actual operating frequency of the device (Narayanaswamy et al., 2012). In these methods the amplitude of the disturbances can be tuned; however, the devices act on the fluids only around them. On the flexibility of the point of application, laser energy deposition has an advantage because it can induce local disturbance at a distant point. Im et al. reported that the boundary layer separation was suppressed by the local disturbance generated by pulsed laser energy deposition and it triggered the instability of the boundary layer (Im et al., 2016). Osuka et al. demonstrated that the boundary layer separation in a Mach 1.92 flow was suppressed by the supply of local disturbance generated by repetitive pulsed laser energy deposition (Osuka et al., 2014). Although they paid little attention to the oscillation frequency of the shock wave, repetitive pulsed laser energy deposition is also promising for the control because of its flexibility as well as capability: any size of disturbance can be artificially supplied at any point with any frequency using repetitive pulsed laser energy deposition.

2.1.3 Focus point of this chapter

The shock wave-boundary layer interaction has remarkable characteristics to be revealed as typified by the unsteady motion of the shock wave. The shock wave motion in the interaction is strongly affected by fluctuations in the upstream boundary layer in the weak interaction, therefore, it is important to evaluate the effect of upstream disturbance on the interaction. On the other hand, using repetitive pulsed laser energy

deposition, local disturbance is input to the shock wave-boundary layer interaction in a regular manner. The element input by this method is both density/temperature and velocity; however, the characteristics of upstream disturbance can be controlled by tuning the input energy and the frequency of the pulsed laser energy deposition.

Therefore, in this chapter, the effects of local disturbance supplied in the upstream boundary layer by repetitive pulsed laser energy deposition on the shock wave-boundary layer interaction are discussed. The shock wave-boundary layer interaction is induced on an axisymmetric nose-cylinder-flare model such that the shock wave naturally oscillates on a laboratory coordinate system. As shown in the following section, the structure of the shock wave-boundary layer interaction in this study is three-dimensional; however, it is quite similar to that of the two-dimensional compression ramp configuration described in Fig. 2.1 (a).

2.2 Experimental setup

2.2.1 Apparatus

Figure 2.2 shows the experimental setup. The experiment was conducted in an in-draft supersonic wind tunnel with an $80 \times 80 \text{ mm}^2$ square cross-section, of which the flow Mach number was 1.92. In the test section, the static pressure and the static temperature were 13.8 kPa, and 162 K, respectively. Supply of local disturbance was performed using a Nd:YVO₄ laser (HD40I-E, Edgewave; wavelength 1064 nm, repetition frequency up to 100 kHz, average power up to 400 W). The laser pulse, of which initial spot area was 6 mm \times 6 mm square, was expanded to 15 mm \times 15 mm square by a concave and convex lenses. The laser pulse was focused at 24 mm upstream of the model by a GRADIUM®

lens with the focal length of 60 mm through a BK7 window. At the focus point, laser breakdown was induced, and the gas heated by the laser pulse rapidly expanded until the pressure of it became equal to the ambient pressure. After the expansion, a high temperature and low density region separated by a contact surface was formed. Hereafter, we will refer to the region as a “laser-heated bubble.” The energy of each pulse, E_p , was set to 7.4 mJ at a laser pulse repetition frequency, f_d , of 30 kHz and $E_p = 6.7$ mJ at $f_d = 60$ kHz. f_d corresponds to the frequency at which the disturbance generated by the laser energy deposition enters to the shock wave-boundary layer interaction region. This difference of E_p was caused by the characteristics of the laser device. Using a ratio $f_d E_p / (\rho U^3 A / 2)$ between an input laser power and a total flow power, which was adopted for the analysis in the previous study (Iwakawa et al., 2017), the input laser power was 2.0% of the total flow power at $f_d = 30$ kHz, under the assumptions that the area A was the cross-sectional area of the wind tunnel and the loss of the pulse energy was negligible. When E_p decreases by 10%, i.e. $E_p = 6.7$ mJ, the ratio becomes 1.8%, which is almost the same value to the ratio when $E_p = 7.4$ mJ. Therefore, in this study, we believe that the difference of E_p in this order did not have such an important impact on the experimental results that is presented hereafter. A high-speed camera (HPV-X, Shimadzu Co.; 400×250 pixels, 256 frames) was used to record the Schlieren images at a rate of 200,000 frame/s. The temporal resolution was improved by synchronizing camera exposure with the irradiation of an incoherent laser with a pulse duration of 100 ns (CAVILUX smart, Cavitar Ltd.; wavelength 640 nm). Unsteady behavior of the density field was analyzed using grayscale Schlieren images sequentially recorded, as described in Section 2.2.2.

The experimental model had an axisymmetric shape composed of a hemisphere nose

with a diameter of 10 mm, a circular cylinder, and a conical flare with an apex angle of 24 deg.. The diameter and the length of the cylinder segment were 10 mm and 20 mm, respectively. In this study, cylindrical coordinates (r, z) are defined as shown in Fig. 2.2. The model was placed in the supersonic wind tunnel using a sting. The sting and the wind tunnel wall did not affect the flow field. The flow field around the intersection between the cylinder and the flare was of particular interest in this study. A shock wave was induced by the flare and it interacts with boundary layer developed on the cylinder. The detail structure of the interaction on this model is described in Section 2.3.1.

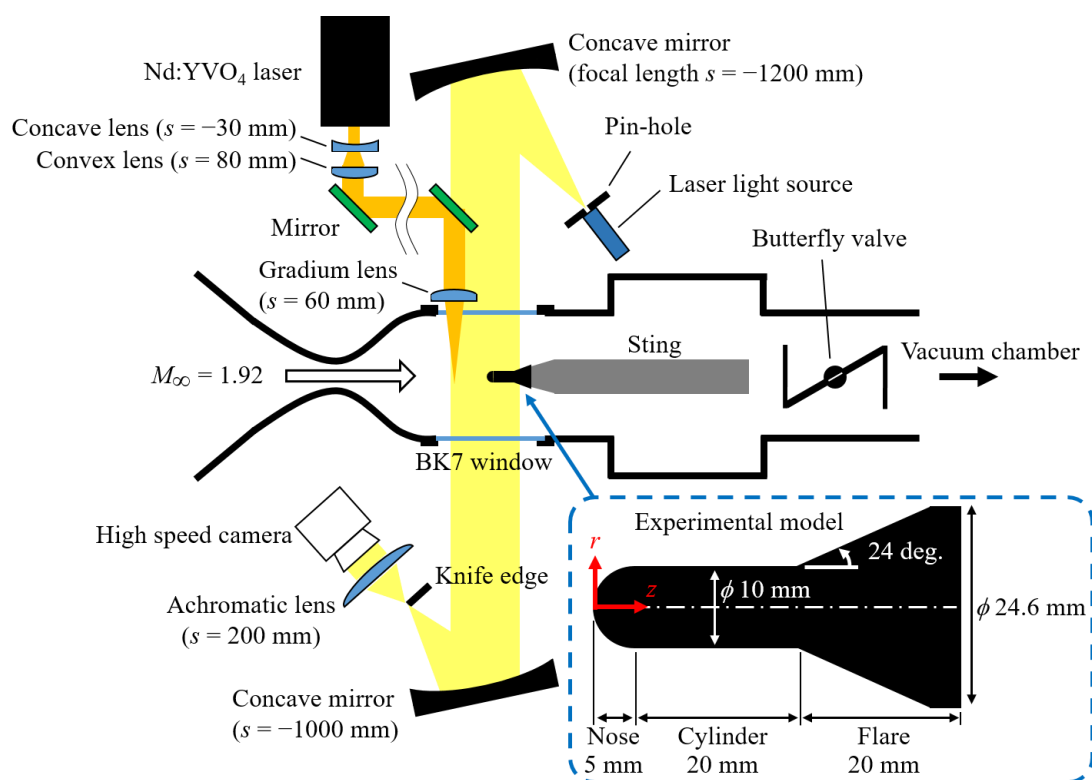


Figure 2.2 Experimental apparatus.

2.2.2 Method of spectral analysis

In this study, frequency analysis was conducted based on the power spectrum of each pixel calculated using the fast Fourier transform (FFT) from an 8-bit brightness history of the Schlieren images.

Figure 2.3 shows an example of temporal brightness history obtained at a uniform flow location $(r, z) = (11 \text{ mm}, -1.7 \text{ mm})$ in the case without local disturbance (basic flow, see Fig. 2.5). The entire recording time of the Schlieren images for each run was $1280 \mu\text{s}$. Hereafter, the brightness history obtained from the Schlieren images is referred to as “raw data.” In the experiments, the output power of the light source was set to its maximum, accordingly its intensity decreased as the capacitor voltage decreased. As a result, at each point the brightness of the raw data decreased in proportion to the elapsed time as shown in Fig. 2.3. This was caused by the light source performance, not fluid dynamics behavior. The time constant of the brightness decay, which was defined by the record length, was approximately 1 ms , corresponding to a frequency of 1 kHz . To eliminate the effect of the decay of the light source intensity, the variation component of the brightness history was extracted. This variation component, which is referred to as “processed data”, was obtained by taking the difference between the raw data and its line of best fit calculated using the least squares method.

From the temporal brightness histories, power spectrum densities were calculated by using FFT. Figure 2.4 shows examples of the power spectrum densities calculated from the raw data and the processed data in Fig. 2.3. The analysis frequency range was $0.78 - 100 \text{ kHz}$, which was determined by the framing rate and the entire record time of the camera. Hereafter, the frequency of the spectral analysis is referred to as f_s . In the case of the raw data, the low frequency regime was considerably limited: the spectrum of this

brightness decay was spread over a wide low-frequency range. In contrast, in the case of the processed data, the low-frequency spectrum due to the brightness decay was suppressed. Therefore, in the following sections, fluid dynamics behaviors are analyzed based on the spectrum of the processed data.

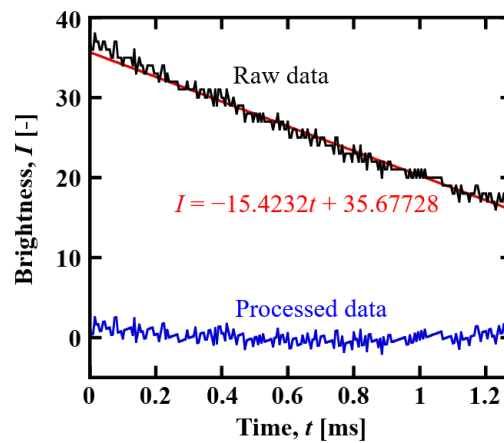


Figure 2.3 Brightness history at uniform flow $(r, z) = (11 \text{ mm}, -1.7 \text{ mm})$, corresponding to Fig. 2.5 (raw data); red line is the line of best fit, found by the least squares method; processed data is the difference between raw data and the line of best fit.

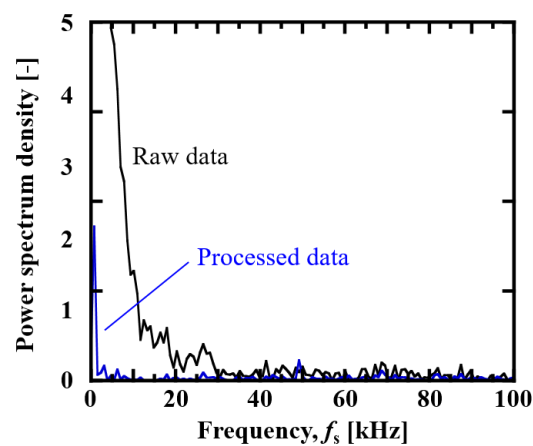


Figure 2.4 Power spectrum density at uniform flow, corresponding to raw data and processed data in Fig. 2.3.

2.3 Effect of local disturbance on shock wave oscillation

2.3.1 Basic flow characteristics

Figure 2.5 shows the Schlieren images without local disturbance, with the interval of $10 \mu\text{s}$. In Fig. 2.5, a bow shock was formed in front of the hemisphere nose. A boundary layer developed along the cylinder and interacted with a shock wave induced by the flare, which is hereafter referred to as a “flare shock.” In Fig. 2.5, the dark zone due to the flare shock at $r = 9 \text{ mm}$ had a thickness in the radial direction of approximately 0.4 mm . Assuming an axisymmetric flow field, this line of view at this radial location covered an azimuthal angle of 34 degrees . Therefore, the present image processing could not capture asymmetric behavior whose characteristic azimuthal angle was larger than this value. However, in the present analysis the primary interest is the response of the flare shock in the frequency domain. Although the distribution of oscillation amplitude might not be completely symmetric, the frequency modulation characteristics of the shock wave oscillation in its fundamental mode should have been held at any azimuthal location.

Along the cylinder surface, the boundary layer stayed thin and could not easily be observed in the Schlieren images. However, the foot of the flare shock, which without the shock wave-boundary layer interaction should have been extended to the flare corner at $(r, z) = (5 \text{ mm}, 25 \text{ mm})$, was dispersed to a couple of compression waves for $z < 28 \text{ mm}$. As seen in the sequence of the Schlieren images, this dispersed portion exhibited unsteady behavior, which was likely caused by the interaction, and then induced oscillation of the flare shock for $z > 28 \text{ mm}$.

Figure 2.6 shows spatial distributions of the power spectra, which were obtained from brightness histories in sequential frames. In the figure, color contours of an

integrated power spectrum in the range of 27.5 kHz to 32.5 kHz and 57.5 kHz to 62.5 kHz are displayed. The contour levels are common to all of the figures, including Fig. 2.9. In the Schlieren images, a shock waves was recognized as a “dark” line with a finite thickness, which was caused both by the spatial integration through an almost axisymmetric phenomenon and by the spatial resolution of the present optical system. If a shock wave fluctuates within a spatial amplitude smaller than the effective thickness of its Schlieren image, the corresponding power spectrum does not appear.

In this case, the flare shock oscillation did not have any strong peak spectrum of around 30 or 60 kHz, as seen in Fig. 2.6. However in Fig. 2.7 it had broad spectra, which was consistent with the previous study (Erengil and Dolling, 1991a). As seen in Fig. 2.5, near the wall surface, the flare shock foot became dispersed into compression waves, which had finite density gradients. The power spectrum in this “dispersed” region could not be well resolved. However, the oscillation behavior of the flare shock which should have been influenced by the dispersed the shock wave-boundary layer interaction region could be clearly diagnosed. Figure 2.7 shows one-dimensional distributions of power spectrum density along $r = 9$ mm. In the plot, spectra of the flare shock oscillation was clearly seen. Even without local disturbances, the flare shock oscillation was observed. The spectrum of this oscillation seemed to have a peak lower than 10 kHz, however the clear dominant frequency could not be captured in this study because of the limitation of the frequency resolution.

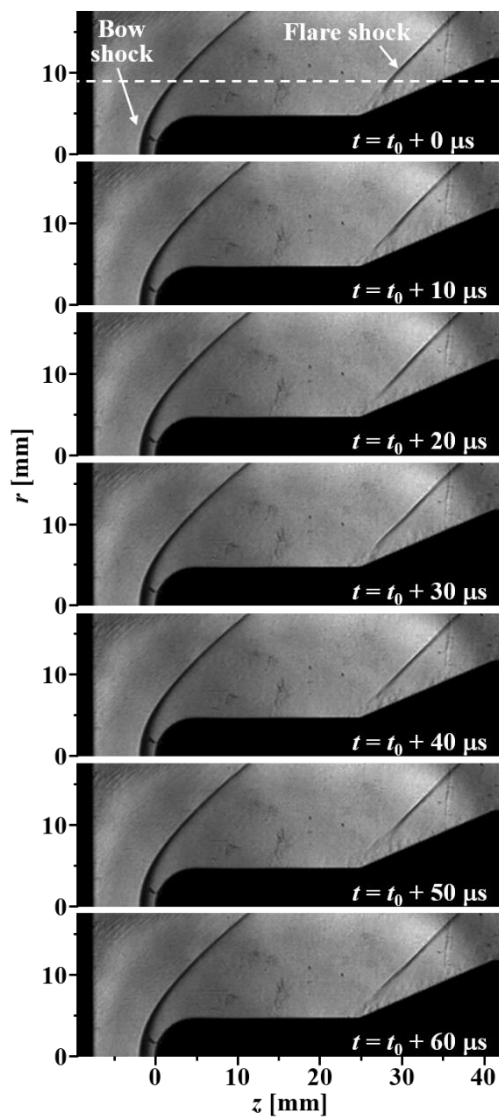


Figure 2.5 Schlieren images, without local disturbance (basic flow).

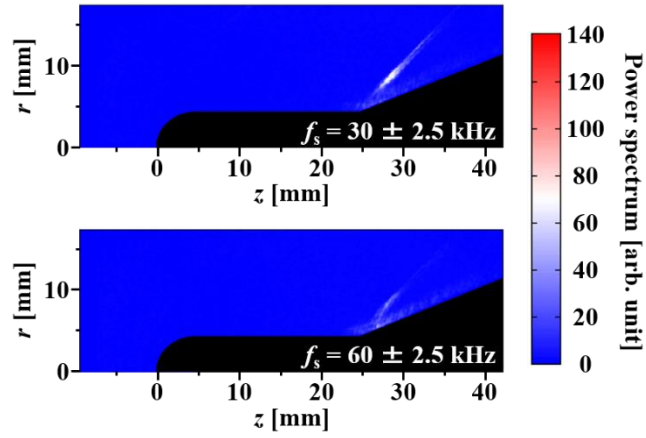


Figure 2.6 Power spectrum distributions, w/o local disturbance (basic flow).

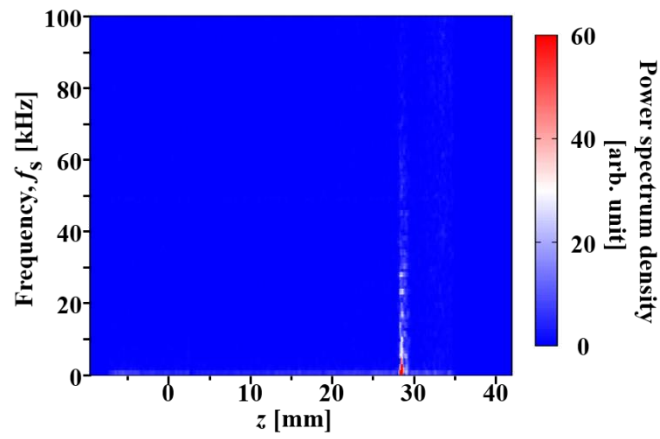


Figure 2.7 Distributions of power spectrum density along $r = 9$ mm, the dashed line in Fig. 2.5, w/o local disturbance (basic flow).

2.3.2 Effect of local disturbance frequency

Figure 2.8 shows the Schlieren images with local disturbances at $f_d = 30$ and 60 kHz, with the interval of 10 μ s. Figures 2.9 and 2.10 describe spatial distributions of the power spectra and one-dimensional distributions of power spectrum density along $r = 9$ mm, respectively. The contour levels of Figs. 2.9 and 2.10 are common to Figs. 2.6 and 2.7, respectively.

In the case with local disturbances at $f_d = 30$ kHz, a laser pulse was focused and a laser-heated bubble was generated after laser-induced breakdown at $(r, z) = (0 \text{ mm}, -24 \text{ mm})$. The bubble, which had an almost spherical shape, entered the bow shock layer. As seen in Fig. 2.8 (a), due to the baroclinic effect, which caused by the interaction between the density change across the bubble and the pressure change across the bow shock, a vortex ring was generated in the bow shock layer (Kim et al., 2011). Therefore, a density/temperature and velocity disturbance was supplied to the shock wave-boundary layer interaction region by the laser energy deposition. When a vortex ring arrived around the flare corner, the flare shock bent. The deformation of the wave front propagated upwards over time and then the flare shock restored its straight shape. These processes were repeated at about 30 μ s intervals; the associated frequency of the shock wave deformation was equal to f_d , at which the disturbance were supplied to the interaction region. In the case of $f_d = 30$ kHz, as seen in Figs. 2.9 (a) and 2.10 (a), in the bow shock layer a spectrum of $f_s = 30$ kHz became dominant because the bow shock was deformed when each laser-heated bubble entered it. The power spectrum of $f_s = 60$ kHz at the bow shock was also strong as the second harmonic. The flare shock foot oscillated as each vortex ring arrived with the same frequency as that of f_d . Therefore, the flare shock foot also had a strong spectrum of 30 kHz. The reason why the oscillation frequency at f_d

became dominant is beyond the scope of this study. However, as a possible mechanism, the suppression of the boundary layer separation by the disturbance can be pointed out, as mentioned by Osuka et al. (Osuka et al., 2014). In the case with local disturbances, weak line spectra with a constant frequency separation were obtained; they were the beat spectra caused by the radiation emission from the laser-induced breakdown and camera exposure. In Fig. 2.10 (a), for example, the camera framing rate of 200 kHz and $f_d = 30$ kHz yielded a fundamental beat of 10 kHz. These line spectra were merely artifact, and did not reflect any fluid dynamics phenomena.

The most remarkable modulation was observed in the case with local disturbance at $f_d = 60$ kHz. The shock wave-boundary layer interaction also induced fluctuations of the flare shock, which propagated downstream along the flare shock (Figure 2.8 (b)). It is of particular importance to note that, these fluctuations did not correspond to the repetition frequency of the local disturbance. The flare shock oscillation spectra did not have a peak of $f_s = f_d = 60$ kHz, as seen in Figs. 2.9 (b) and 2.10 (b). Instead, a wide spectrum of $f_s < 20$ kHz, as seen in Fig. 2.10 (b), became strongest. In addition, the high frequency component of the broad spectrum spread in the case without local disturbance was weakened. An important discovery here is that the flare shock foot oscillation was stabilized owing to the supply of local disturbances of the high repetition frequency, 60 kHz, with the clear frequency modulation.

In this study, the new combination of the light source and the high-speed camera could be used for commercial product demonstration purposes for only a short period of time. Therefore, besides the experiments presented above, further experiments for $f_d = 10, 20,$ and 40 kHz were conducted using an existing optical arrangement (Osuka et al., 2014). As a result, with $f_d = 30$ kHz and lower, the spectrum of the flare shock oscillation

at the frequency equal to f_d became dominant. On the other hand, as was presented for $f_s = 60$ kHz in Figs. 2.9 (b) and 2.10 (b), with $f_d = 40$ kHz and higher, the spectrum of f_d was weak and the flare shock oscillation was modulated to the low frequency range.

According to Osuka et al., the residence time of a vortex ring in the bow shock layer was evaluated for up to $40 \mu\text{s}$ (Osuka et al., 2014). Therefore, with $f_d > 25$ kHz, more than two vortex rings coexisted in the shock layer, see Fig. 2.8 (b). When f_d is close to 25 kHz, two vortex rings did not contact each other and acted independently because the thickness of the shock layer was greater than that of the vortex rings. However, when f_d is high enough, these two vortex rings should have interacted and combined with each other although it is hardly observed in the present Schlieren visualization. This scenario should have also been repeated for succeeding vortex rings. Upstream from the bow shock, the flow speed equaled 490 m/s. The separation distance between laser-heated regions was 8 mm, which was greater than the diameter of the laser-heated region by about four times. However, after the laser-heated regions entered the shock layer, the separation distance became much shorter because the flow speed in the shock layer was much lower. Therefore, the influence of the successive disturbed elements became linked together in the bow shock layer and the following boundary layer, thereby drastic frequency modulation should have occurred. This seems to be a reasonable cause for this frequency modulation, and moreover is expected to be useful in practical application to moderate the performance of flow devices.

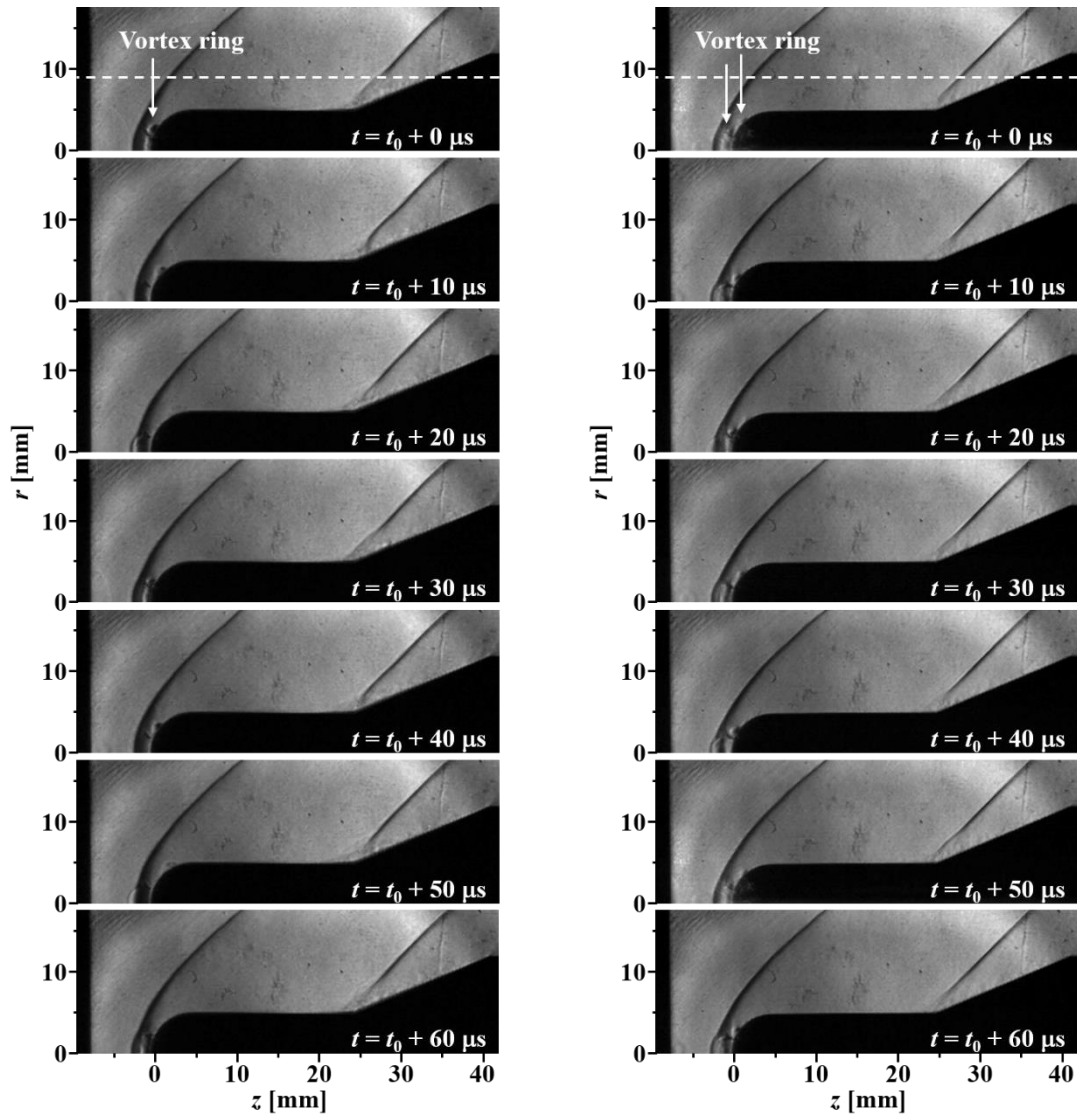
(a) w/ local disturbance, $f_d = 30$ kHz.(b) w/ local disturbance, $f_d = 60$ kHz.

Figure 2.8 Schlieren images, w/ local disturbance by pulsed laser energy deposition; frequency of local disturbance, f_d .

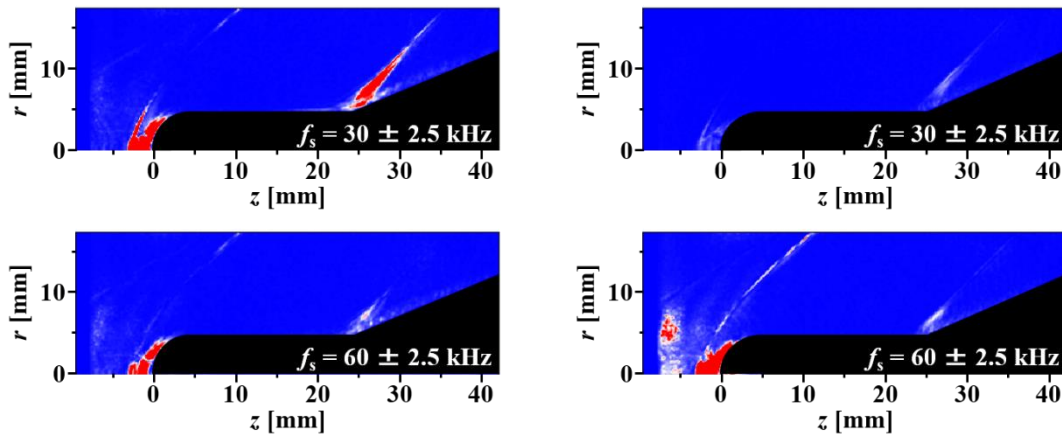
(a) w/ local disturbance, $f_d = 30$ kHz.(b) w/ local disturbance, $f_d = 60$ kHz.

Figure 2.9 Power spectrum distributions, w/ local disturbance; frequency of local disturbance, f_d ; the contour levels are common to Fig. 2.6.

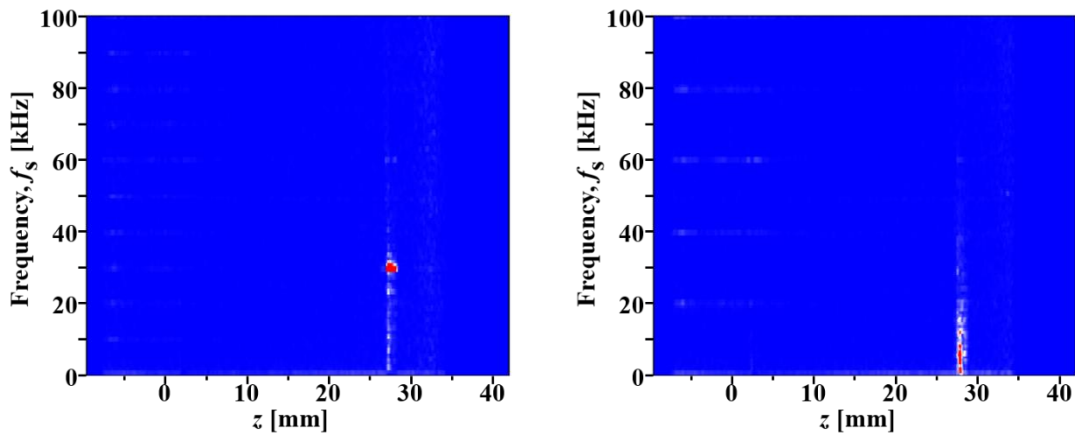
(a) w/ local disturbance, $f_d = 30$ kHz.(b) w/ local disturbance, $f_d = 60$ kHz.

Figure 2.10 Distributions of power spectrum density along $r = 9$ mm, the dashed line in Fig. 2.8, w/ local disturbance; frequency of local disturbance, f_d ; the contour levels are common to Fig. 2.7.

2.4 Summary of this chapter

In this chapter, the effects of local disturbance on the shock wave oscillating driven by the shock wave-boundary layer interaction were investigated. In this study, local density/temperature and velocity disturbance was repetitively supplied to the interaction region.

- In the case without local disturbance, the shock wave oscillated by the interaction with the boundary layer. Although a clear dominant oscillation frequency of the shock wave could not be resolved, oscillation spectra was observed at the position of the shock wave: strong spectra lower than 10 kHz and weak spectra spread over broad frequency range.
- In the case with local disturbance, the dominant frequency of the shock wave oscillation was modulated. However the mode of the frequency modulation differed by the supplying frequency of the local disturbance, f_d .
 - In the case that the frequency of the local disturbance, f_d , was 30 kHz and lower, in which disturbed elements independently entered to the interaction region, the shock oscillation exhibited the strongest peak at the supplying frequency of the local disturbance.
 - In the case that the frequency of the local disturbance, f_d , was 40 kHz and higher, the flare shock oscillations experienced a drastic frequency modulation towards a much lower domain with the spectrum of f_d vanishing. In this case, successive disturbed elements, which interacted and connected each other, were drifted along the model.

Chapter 3

Overpressure modulation behind blast wave by local turbulent flow

3.1 Shock wave-turbulence interaction

In Chapter 2, we investigated the effects of local disturbance input at a single location in a regular manner on the shock wave-boundary layer interaction. In contrast, the interaction between shock wave and disturbance input in a certain volume is the subject of the study in this chapter. The disturbance here is random velocity fluctuation, and the effects of interaction with the fluctuation on the shock wave are experimentally evaluated.

3.1.1 Effect of turbulence on shock wave

There universally exists velocity fluctuation in fluids as turbulence. When velocity fluctuation interacts with a shock wave, it affects the characteristics of the shock wave owing to the variation of the relative shock Mach number induced by the upstream velocity fluctuation. Ribner et al. reported that the modulation of the overpressure and the rising time of the shock wave depended on the direction of the upstream local flow velocity (Ribner et al., 1973). Kim et al. observed the relationship between the modulation of the overpressure and that of the shock wave front from Schlieren visualization (Kim et al., 2010). To summarize these studies, the effects of upstream local flow velocity on a

shock wave are as follows: when the upstream flow velocity of the shock wave is locally greater than the mean flow velocity, the overpressure of the shock wave increases and its rising time decreases, while the wave front falls back from the average. In contrast, when the upstream flow velocity of the shock wave is less than the mean flow velocity, the overpressure of the shock wave decreases and the rising time increases, while the wave front precedes. The same effects of the upstream local flow velocity on the shock wave front have been reported by some researchers who studied the interaction with a single vortex (Hollingsworth and Richards, 1955; Dosanjh and Weeks, 1965).

Turbulence has velocity fluctuation and these effects locally and randomly appear on a shock wave when it interacts with turbulence. Therefore, the interaction between a shock wave and turbulence should be statistically investigated. In this context, previous studies focused on the variation of the pressure field behind the shock wave when it interacted with turbulence. Lipkens and Blackstock reported that the interaction with a slit jet increased the rise time and decreased the peak overpressure of the shock wave, on average (Lipkens and Blackstock, 1998). They also showed that the standard deviations of the rise time and the peak overpressure increased with the interaction. Ukai et al. also reported the increase in the standard deviation of the peak overpressure of the shock wave with the distortion of the wave front (Ukai et al., 2016). Xanthos et al. found that the variation in the static pressure behind the planar shock wave was increased by the interaction with grid turbulence (Xanthos et al., 2002). Sasoh et al. showed that the standard deviation of the peak overpressure of the shock wave that interacted with grid turbulence had a positive correlation with the amplitude of the upstream velocity fluctuation (Sasoh et al., 2014). Inokuma et al. reported that the modulation of the peak overpressure of the shock wave caused by the interaction with grid turbulence was related

to the turbulent motion with the order of the integral length scale (Inokuma et al., 2017). However, there are some technical problems in the previous studies to quantitatively investigate the shock wave-turbulence interaction, as described in Section 3.1.2.

Some studies using direct numerical simulation reported that significant modulations of the shock wave front could appear as a result of the interaction with isotropic turbulence (Lee et al., 1993; Larsson and Lele, 2009; Larsson et al., 2013). The upstream velocity fluctuation of turbulence caused local and random modulation of the wave front: at some points the wave front preceded and at other points it fell back from the average. Larsson and Lele named the regime “wrinkled shock” (Larsson and Lele, 2009). They also showed that the impact of the turbulence interaction on the shock wave modulation varied according to the strength of the velocity fluctuation relative to the shock wave. When the amplitude of the velocity fluctuation was sufficiently strong relative to the shock wave, the relative shock Mach number of the shock wave could locally be less than one. In this case, the shock wave locally degenerated to compression waves such that the wave front was broken. Such a regime with topology change of the shock wave front is the so-called “broken shock” (Larsson and Lele, 2009). Using the relative shock Mach number, M_s , and turbulent Mach number, M_t , some criteria of the “broken shock” have been suggested by the following studies: $M_t^2 > 0.1(M_s^2 - 1)$ by Lee et al. (Lee et al., 1993), $M_t^2 \gtrsim 0.06(M_s^2 - 1)$ by Larsson and Lele (Larsson and Lele, 2009), and $M_t \gtrsim 0.6(M_s - 1)$ by Larsson et al. (Larsson et al., 2013). In this thesis, the criteria $M_t \gtrsim 0.6(M_s - 1)$ proposed by Larsson et al. (Larsson et al., 2013) is used for the analysis because it is the most severe condition for the “broken shock” regime. However, these studies were conducted at conditions almost beyond those of experimental studies: although Sasoh et al. and Inokuma et al., who investigated the interactions with grid

turbulence, conducted their studies under the conditions of $M_t \lesssim 0.6(M_s - 1)$, conducting the experimental study fully in the “broken shock” criteria is difficult because of the limitations of facilities (Sasoh et al., 2014; Inokuma et al., 2017).

3.1.2 Existing methods of shock wave-turbulence interaction study

Many researchers have reported the modulation of shock wave through the interaction with turbulence, as shown in Section 3.1.1. The previous studies reported the modulation of the post-shock pressure by the turbulence interaction and its correlation with the characteristics of turbulence. However, quantitative evaluation is not enough, especially in experimental studies. One of the main reasons is the difficulty in realizing the shock wave-turbulence interaction while controlling the strength of the shock wave and the characteristics of the turbulence independently, although the previous studies have been conducted using various setups.

A shock tube is one of the strong facilities that can be used to investigate the interaction between shock wave and turbulence, because a planar shock wave and grid turbulence, which are suitable for quantitative evaluations, can be applied to experiments. In this method, nearly isotropic turbulence, which is generated from a grid by disturbing the uniform flow behind an incident shock wave, interacts with a reflected shock wave formed by the reflection of the incident shock wave at the end wall of the shock tube. Dosanjh used a shock tube and reported that the fluctuation, which represented small, local deformations of the wave front, appeared on the planar shock wave by the interaction with grid turbulence (Dosanjh, 1956). Keller and Merzkirch found that

turbulence was amplified by the interaction with the reflected shock wave in a shock tube experiment (Keller and Merzkirch, 1990). However, the experimental conditions were quite limited because the shock wave and grid turbulence were not independent. Although some researchers installed porous walls as the end walls of shock tubes to weaken the reflected shock wave that interacted with the grid turbulence, a strong shock wave could not be applied and the strength of the weakened reflected shock wave depended on the porosity of the porous wall (Honkan and Andreopoulos, 1992; Honkan et al., 1994; Xanthos et al., 2002; Agui et al., 2005).

Barre et al. installed a pair of shock generators in a supersonic wind tunnel to induce a planar shock wave by Mach effect (Barre et al., 1996 and 1998). Using the planar shock wave, they investigated the effect of the interaction with the shock wave on compressible grid turbulence generated by a grid placed in the supersonic wind tunnel, in front of the planar shock wave. In this case, however, the strength of the planar shock wave was determined by the designed Mach number of the supersonic wind tunnel, and the grid induced not only grid turbulence but also shock and expansion waves, which disturbed the upstream flow. Lipkens and Blackstock realized the interaction between a planar shock wave and a local jet by using a reflected shock wave from a parabola (Lipkens and Blackstock, 1998). However, the region where the shock wave could be regarded as a planar shock wave was quite limited because of the effect of expansion waves propagating from the edge of the parabola. In addition, when a local jet was used as a turbulent source, it was difficult to define the characteristics of turbulence because they locally varied in the jet.

A decaying shock wave, like a blast wave described in the next section, was also applied to the investigation. Bass et al. and Ukai et al. conducted interaction experiments

between shock waves from supersonic free-flight models and atmospheric turbulence/air jet (Bass et al., 1987; Ukai et al., 2016). Ribner et al. used a hemisphere shock wave generated by an open-end shock tube and a local jet (Ribner et al., 1973). Kim et al. investigated the effect of the interaction between a spherical shock wave generated by laser-induced breakdown and a local jet (Kim et al., 2010). Some researchers installed an open-end shock tube in a closed-loop wind tunnel to investigate the interaction between a spherical shock wave and grid turbulence (Sasoh et al., 2014; Inokuma et al., 2017; Kitamura et al., 2017). In those methods, the strength of the shock wave can be adjusted for the investigation; however, the shock wave was rapidly attenuated near the explosion point or an equivalent point to that.

In contrast, a blast wave generated by explosion becomes relatively weak in far field. Although the non-planarity effect cannot be ignored near the explosion point, the radius of curvature of the blast wave becomes larger when the blast wave propagates a sufficient distance in the field. If this is applied to the study of the turbulence interaction, the blast wave can be regarded as a weak quasi-planar shock wave in the interaction region. In this method, the sufficient state can be realized to investigate the characteristics of the rising of the shock wave. However, a large experimental setup is necessary as the blast wave has to propagate a sufficient distance from the explosion point. Therefore, in this study, an interaction experiment between a quasi-planar blast wave, which propagated a distance of several meters, and a local turbulent flow was conducted in the field. Using the local turbulent flow with a certain cross-section, homogeneity of the turbulence can be expected to a certain degree. The purpose of this chapter is to investigate the effect of the local turbulent flow on the pressure field behind the weak blast wave.

3.1.3 Features of blast wave

A blast wave is a shock wave accompanied by an expansion region behind it, which typically appears after the explosion or a similar action. The sources of the blast wave include compressed gas, chemical reaction, nuclear reaction, and plasma generation by discharge or laser-induced breakdown. Figure 3.1 shows a typical waveform of a blast wave, the so-called “Friedlander waveform” (Friedlander, 1946; Goel et al., 2012). The waveform of the blast wave can be divided into two durations: positive pressure duration and negative pressure duration, in which the overpressures of the blast wave are greater and less than the ambient pressure, respectively. To consider the load caused by the blast wave, the impulse, which is the integral of the overpressure in each duration, is often used as a parameter along with the overpressure (Goel et al., 2012). The equation of the Friedlander waveform, which gives the relationship between the overpressure, $\Delta P(t)$, and time, t , can be written as

$$\Delta P(t) = \Delta P_{\text{peak}} \left(1 - \frac{t}{t_1}\right) e^{-b\frac{t}{t_1}} \quad (3.1)$$

where ΔP_{peak} is the peak overpressure, t_1 is the duration of the positive pressure, and b is a constant (Goel et al., 2012). The blast wave is generally spherical, therefore the overpressure of the blast wave attenuates with the cube of the propagation distance, r , which is equal to the radius of curvature of the blast wave (Kleine et al., 2005). ΔP_{peak} is also affected by the released energy, w , therefore Eq. (3.1) can be written in Eq. (3.2).

$$\Delta P(t) = \Delta P_{\text{peak}}(w, r) \cdot \left(1 - \frac{t}{t_1}\right) e^{-b\frac{t}{t_1}} \quad (3.2)$$

Introducing the scaled distance, $z = r/w^{\frac{1}{3}}$, a similarity rule holds between the peak overpressure and the scaled distance, z (Held, 1983).

As well as flame, poisonous gases, and debris, a blast wave induced by explosion

has the potential to damage the structures of buildings and cellular tissues of human bodies. Since blast wave can propagate to relatively large distances in comparison with the others, it causes various types of damages over a broad area. Near the explosion point, where the overpressure of the blast wave is the order of 10 – 100 kPa or more, the blast wave causes catastrophic damages to buildings, including the collapse of structures (Ullah et al., 2017). In this overpressure range, the blast wave also harms the human body: the brain and lungs, which are critical parts of the body, are physically damaged (Chafi et al., 2010; Plurad, 2011). When hazardous materials are stored in tanks and so on, the blast wave that propagates from far field can damage the storage area and lead to other explosions caused by the leakage of the materials (Cozzani et al., 2004). This phenomenon, called the “domino effect,” can occur when the overpressure of the trigger blast wave is several kilopascals. In this pressure range, the tympanic membrane of human ear is also damaged by the blast wave because of its sensitivity (Plurad, 2011). In addition, Moochhala et al. suggested that neurons in the brain could degenerate from exposure to the blast wave, and the degeneration caused deterioration in performance (Moochhala et al., 2004). When blast wave propagates further away, the overpressure of the blast wave attenuates to the order of 1 kPa. Even in this case, the blast wave can cause damages such as window breakage (Needham, 2010). To estimate and avoid these damages, the evaluation of blast wave accounts for important part in the risk assessment of explosion. In reality, velocity fluctuation often exists on the ray of blast wave as natural wind in the atmosphere, and it can affect the characteristics of the blast wave. For an accurate assessment, it is necessary to evaluate the effect of velocity fluctuation on the overpressure of the blast wave, however few studies have been conducted with the consideration of velocity fluctuation. Therefore, the investigation of the effect of

turbulence interaction on the blast wave also has a large impact on the risk assessment of explosion.

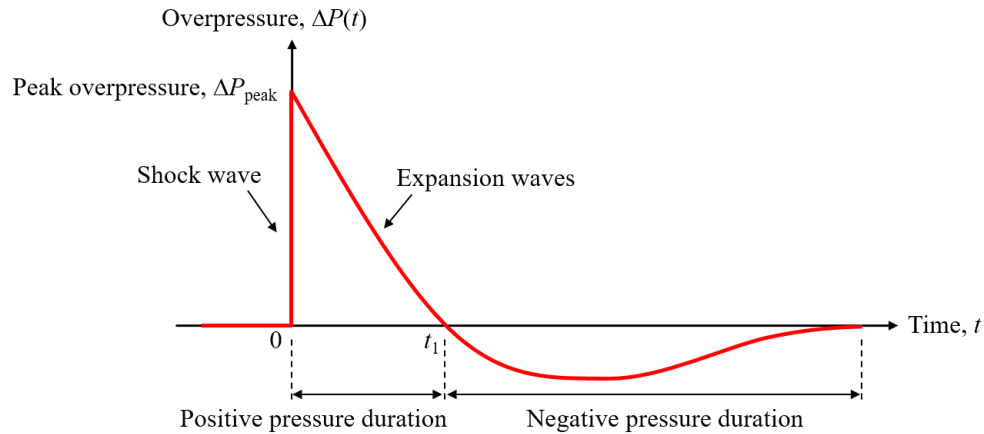


Figure 3.1 Typical waveform of blast wave.

3.2 Experimental setup

3.2.1 Apparatus

Figure 3.2 shows the experimental setup, and Fig. 3.3 shows the image of the experimental field. The experiments were conducted in a field located in the premises of the National Institute of Advanced Science and Technology in Tsukuba, Japan. The area of the experimental field was $20 \times 15 \text{ m}^2$. Blast wave sources and a turbulence generator were set in the field, and the pressure waveforms of blast waves were measured using microphones. Moreover, a natural wind anemometer (Windworks, Field Pro) was installed at the top of the turbulence generator to measure the speed of natural wind.

Figure 3.4 shows the image of the blast wave source. A paper tube filled with a report composition (KP : Al : S = 65 : 19 : 16) of 0.5 g was held by a fuse at a height of 1000 mm from the ground and 6000 mm from the grid, as also shown in Fig. 3.2. The report

composition was ignited by the combustion of a fuse head using an electric signal, and blast wave was generated.

The turbulence generator was composed of a blower (SF-45MS-1VP, Suiden; fan diameter 450 mm), a duct having a square cross section, and a square grid, as shown in Fig. 3.2. The height of the central axis of the turbulence generator was set to 1000 mm, which was the same as that of the blast wave sources. The flow induced by the blower was contracted and passed through the 600-mm strait duct. Then the flow was blown down through the nozzle having a square cross section of $340 \times 340 \text{ mm}^2$ in a direction opposite to that of the blast wave in order to increase the interaction distance. A square grid was set on the nozzle to disturb the flow passing through the grid. Figure 3.5 shows the schematics of the square grid. The grid was composed of $10 \times 10 \text{ mm}^2$ square pillars, which crossed each other at intervals of 50 mm. The solidity of the grid was 36%.

The pressure waveforms of the blast waves were measured using four microphones (4939-A-011, Brüel & Kjær; frequency range 4 Hz – 100 kHz). Figure 3.6 shows the arrangement of the microphones, and Fig. 3.7 shows its image. The microphones were supported by holders and symmetrically installed in the path of a local turbulent flow induced by the turbulence generator in a direction opposite to that of the blast wave, as also shown in Fig. 3.2. The microphone heads were located at a distance of 500 mm from the grid, and the interval between the microphones was 150 mm. The signals obtained from the microphones were amplified using an amplifier and measured by a digital memory scope in an observatory.

The experiments were conducted over two days. The experimental conditions are described in Table 3.1. To evaluate the effect of the local turbulent flow induced by the turbulence generator on the blast waves, the blast wave sources were exploded when the

natural wind, speed monitored using the natural wind anemometer, was 0.0 m/s. In the experiments, five shots were performed in Day 1, and three shots were performed in Day 2, for the case where the blast waves propagated without the local turbulent flow (referred to as “without flow”). Furthermore, ten shots were performed in Day 1, and seven shots were performed in Day 2, for the case where the blast waves propagated through the local turbulent flow induced by the turbulence generator (referred to as “with turbulence”).

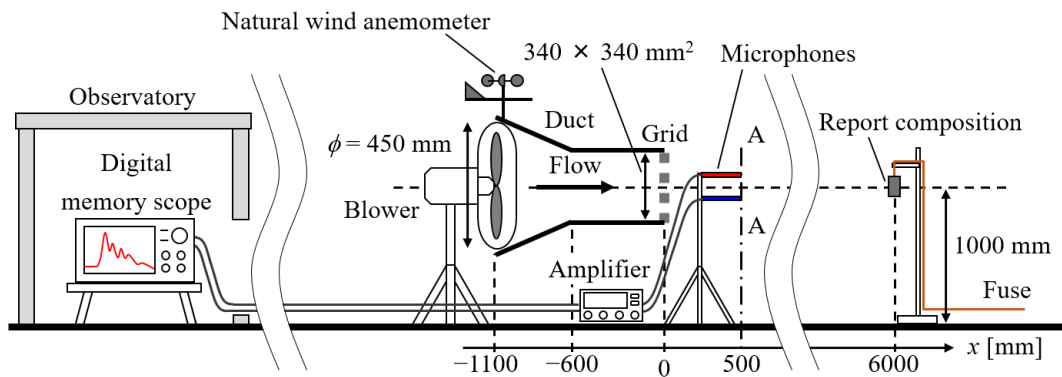


Figure 3.2 Experimental setup.

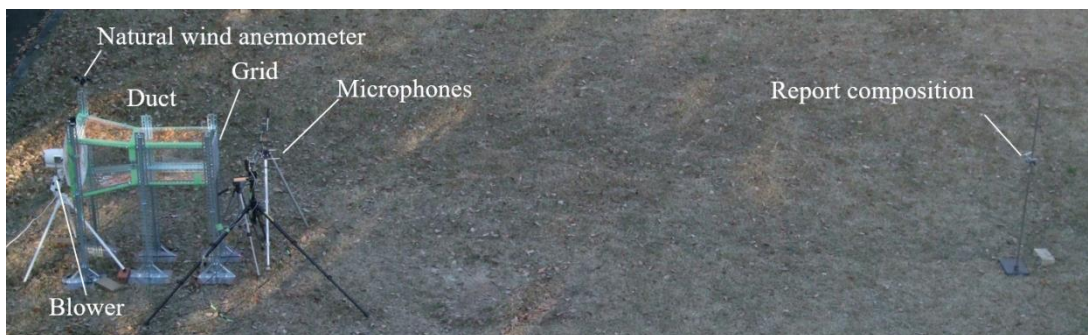


Figure 3.3 Image of experimental field.

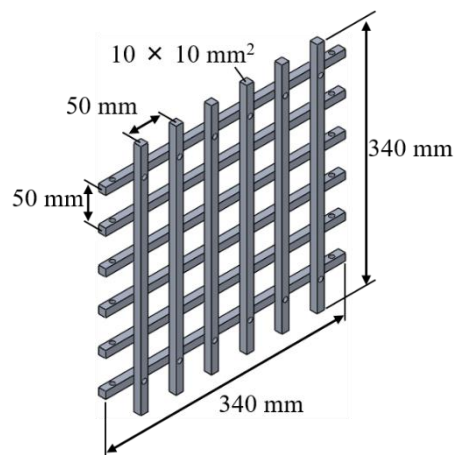
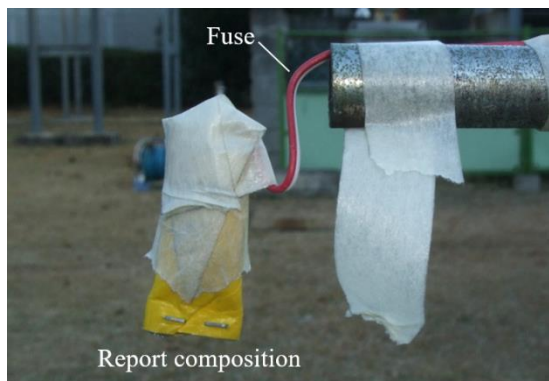


Figure 3.4 Image of blast wave source. Figure 3.5 Square grid, solidity = 36%.

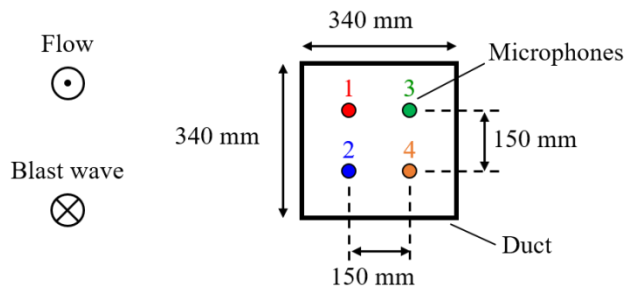


Figure 3.6 Arrangement of microphones, A-A cross section ($x = 500$ mm) in Fig. 3.2, 1 to 4 are microphone numbers.

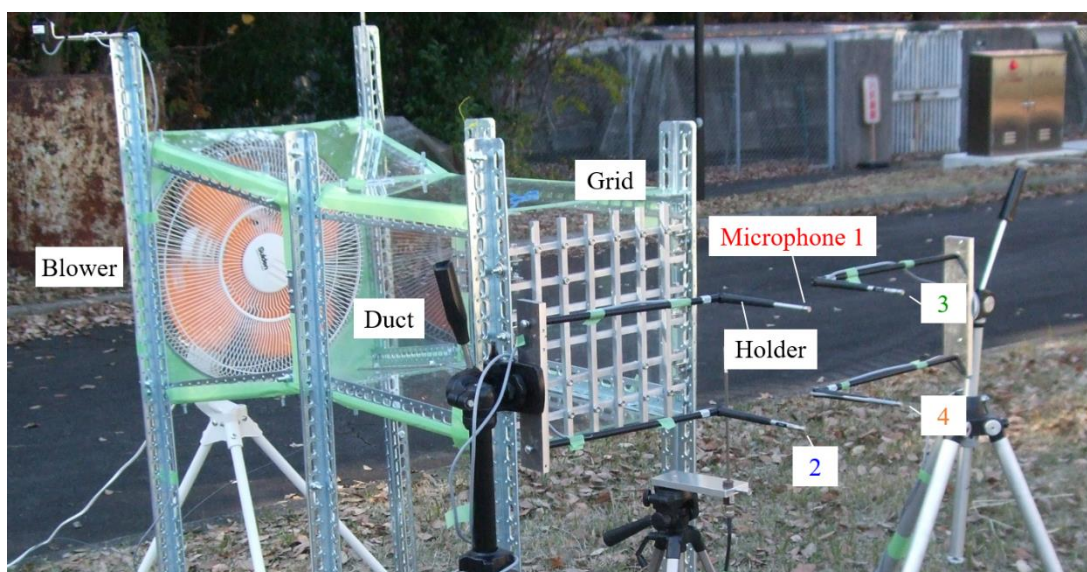


Figure 3.7 Image of Arrangement of microphones, 1 to 4 are microphone numbers.

Table 3.1 Experimental conditions.

	Day 1 : December 3, 2014	Day 2 : December 4, 2014
Weather	Sunny	Cloudy
Atmospheric pressure [kPa]	101.0 – 101.2	100.7 – 100.8
Temperature [°C]	11 – 17	11 – 13
Humidity [%]	26 – 29	~ 68
Natural wind [m/s]	0.0	0.0
Shot number : without flow / with turbulence	5 / 10	3 / 7

3.2.2 Characteristics of turbulence

The characteristics of the local turbulent flow induced by the turbulence generator were obtained from the flow velocity measurement using a hot-wire anemometer (Model 1011, KANOMAX JAPAN Inc.) with an I-type probe (0251R-T5, KANOMAX JAPAN Inc.; tungsten wire, diameter 5 μm , length 2 mm) in an indoor laboratory. The hot-wire anemometer was calibrated by varying the flow velocity under the assumption of incompressible fluid. Figure 3.8 shows the distribution of turbulent characteristics in the flow direction. To obtain the characteristics, the probe of the hot-wire anemometer was set at the position of the microphone 1 (see Figs. 3.6 and 3.7) and swept in a parallel direction to the central axis of the turbulence generator.

Figure 3.8 (a) shows that the time-averaged flow velocity \bar{u} decreased as the distance from the nozzle increased. In contrast, Fig. 3.8 (b) presents that the rms velocity fluctuation u' was about 0.8 m/s. It did not vary greatly in the range of $500 \text{ mm} < x < 2000 \text{ mm}$. When the speed of sound in the atmosphere was $a_\infty = 340 \text{ m/s}$, the turbulent Mach number was $M_t = \sqrt{3/2} u' / a_\infty \approx 2.9 \times 10^{-3}$, under the assumption of

isotropic turbulence. The integral length scale, which represents the average vortex scale in turbulence, was calculated from the rms velocity fluctuation. At the position of the microphone 1 ($x = 500$ mm), the integral length scale was 77 mm. As shown in Fig. 3.8 (c), although the integral length scale decreased as the distance from the nozzle increased, it was still 58 mm at $x = 2000$ mm.

Table 3.2 shows the characteristics of the turbulence measured at the positions of the four microphones and the central axis of the nozzle, in the same plane at $x = 500$ mm. Although the time-averaged flow velocities at the four microphones were $\bar{u} = 4.0 - 4.8$ m/s, whereas that at the central axis of the nozzle was lower, $\bar{u} = 2.9$ m/s, due to the blockage on the rotation axis of the fan. It indicated the distribution of the mean flow velocity in the same plane. A possible reason of the mean flow velocity distribution even at each microphone position is the setting error of the blower. In contrast, the rms velocity fluctuation at the central axis of the nozzle was $u' = 0.7$ m/s. The value was close to those observed at the positions of the four microphones, which ranged between 0.6 – 0.9 m/s. The result represented that the variation of the flow states at each position was not noticeable in terms of the velocity fluctuations.

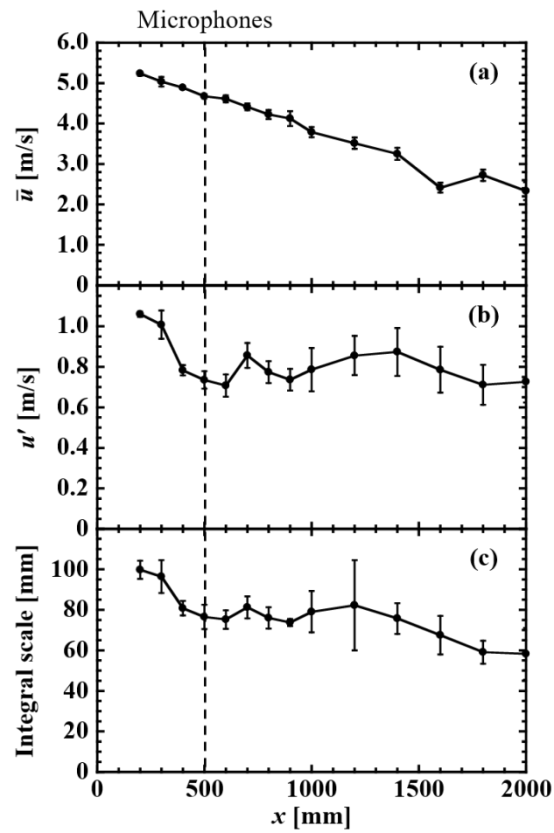


Figure 3.8 Characteristics of turbulence in x direction at the position of microphone 1; (a) time-averaged flow velocity, \bar{u} , (b) rms velocity fluctuation, u' , (c) integral length scale; horizontal axis x is the distance from the nozzle of turbulence generator.

Table 3.2 Characteristics of turbulence in same plane, $x = 500$ mm.

Position	Time-averaged flow velocity \bar{u} [m/s]	rms velocity fluctuation u' [m/s]
Central axis of nozzle	2.9	0.7
microphone 1	4.8	0.7
microphone 2	4.0	0.6
microphone 3	4.3	0.6
microphone 4	4.6	0.9

3.2.3 Pressure signal correction

A typical fast-response pressure transducer is composed of a thin metal diaphragm and a quartz disk or a capacitor. When a waveform of a shock wave is measured using the pressure transducer, a device function that originates from the mechanical oscillation of the sensor caused by an impact of the shock wave is convoluted to a signal of the pressure waveform. To obtain the original waveform, it is necessary to calibrate and remove the device function, which is artifact. Therefore, the waveforms measured by the microphones were corrected through a deconvolution process (Inoue et al., 1991; Sasoh et al., 2014) by using numerical Laplace transform (Wilcox, 1978) to recover the pressure waveforms.

Table 3.3 shows the nomenclatures in the deconvolution process. Using a shock tube, the device function of the microphones was obtained from overpressure measurement behind a planar shock wave. Figure 3.9 shows the waveform of the planar shock wave measured by the microphone. The device function can be calculated using the following method. A waveform measured by a microphone in the shock tube experiment, $y_0(t)$, can be described in Eq. (3.3) using the device function of the microphone, $h(t)$, and an ideal waveform of the planar shock wave, $x_0(t)$. Equation (3.4) shows the Laplace transform corresponding to Eq. (3.3).

$$y_0(t) = \int_{-\infty}^{\infty} h(\tau)x_0(t - \tau)d\tau \quad (3.3)$$

$$Y_0(s) = H(s)X_0(s) \quad (3.4)$$

where $X_0(s)$, $Y_0(s)$, and $H(s)$ are the Laplace transform of $x_0(t)$, $y_0(t)$, and $h(t)$, respectively. When we assume that $x_0(t)$ is a Heaviside function in a finite range of $t \leq T$ as shown in Eq. (3.5), $X_0(s)$ can be written in Eq. (3.6) using ΔP_0 , which is the

overpressure of the planar shock wave corresponding to $x_0(t)$.

$$x_0(t) = \begin{cases} 0 & (t \leq 0) \\ \Delta P_0 & (0 \leq t \leq T) \end{cases} \quad (3.5)$$

$$X_0(s) = \frac{\Delta P_0}{s} \quad (3.6)$$

In discrete form, time, t_m , complex, s_k , and angular frequency division, $\Delta\omega$, are described as follows, respectively:

$$t_m = (2m - 1)\Delta t = (2m - 1)\frac{T}{2(2n)} = \frac{(2m - 1)T}{4n} \quad (3.7)$$

$$s_k = \begin{cases} \alpha + j(2k - 1)\Delta\omega & (k > 0) \\ \alpha + j(2k + 1)\Delta\omega & (k < 0) \end{cases} \quad (3.8)$$

$$\Delta\omega = \frac{\pi}{T} \quad (3.9)$$

Following Wilcox (Wilcox, 1978),

$$\alpha = \frac{2\pi}{T} = 2\Delta\omega \quad (3.10)$$

From Eqs. (3.6) and (3.8),

$$X_0(s_k) = X_0(k) = \frac{\Delta P_0}{\alpha + j(2k - 1)\Delta\omega} \quad (3.11)$$

$Y_0(s)$ can be written as follows using the discrete Laplace transform:

$$\begin{aligned} Y_0(s) &= \sum_{m=1}^{2n} y_0(t_m) e^{-s_k t_m} (2\Delta t) \\ &= \frac{T}{2n} \sum_{m=1}^{2n} y_0(t_m) e^{-s_k t_m} \end{aligned} \quad (3.12)$$

$$Y_0(k) = \frac{T}{2n} \sum_{m=1}^{2n} e^{-\alpha t_m} y_0(t_m) e^{-j \frac{(2k-1)(2m-1)}{4n} \pi} \quad (3.13)$$

$$\operatorname{Re}[Y_0(k)] = \frac{T}{2n} \sum_{m=1}^{2n} e^{-\alpha t_m} y_0(t_m) \cos \left\{ \frac{(2k-1)(2m-1)}{4n} \pi \right\} \quad (3.14)$$

$$\operatorname{Im}[Y_0(k)] = -\frac{T}{2n} \sum_{m=1}^{2n} e^{-\alpha t_m} y_0(t_m) \sin \left\{ \frac{(2k-1)(2m-1)}{4n} \pi \right\} \quad (3.15)$$

Using Eqs. (3.4), (3.11), (3.14) and (3.15), the Laplace transform of the device function, $H(k)$, can be obtained in the form of Eqs. (3.16) and (3.17).

$$\operatorname{Re} \left[\frac{1}{H(k)} \right] = \frac{\Delta P_0 \{ \alpha \operatorname{Re}[Y_0(k)] - (2k-1) \Delta \omega \operatorname{Im}[Y_0(k)] \}}{\{ \alpha \operatorname{Re}[Y_0(k)] - (2k-1) \Delta \omega \operatorname{Im}[Y_0(k)] \}^2 + \{ \alpha \operatorname{Im}[Y_0(k)] + (2k-1) \Delta \omega \operatorname{Re}[Y_0(k)] \}^2} \quad (3.16)$$

$$\operatorname{Im} \left[\frac{1}{H(k)} \right] = \frac{-\Delta P_0 \{ \alpha \operatorname{Im}[Y_0(k)] + (2k-1) \Delta \omega \operatorname{Re}[Y_0(k)] \}}{\{ \alpha \operatorname{Re}[Y_0(k)] - (2k-1) \Delta \omega \operatorname{Im}[Y_0(k)] \}^2 + \{ \alpha \operatorname{Im}[Y_0(k)] + (2k-1) \Delta \omega \operatorname{Re}[Y_0(k)] \}^2} \quad (3.17)$$

In the measurement of a blast wave, the Laplace transform of a measured waveform of the blast wave, $Y(s)$, can also be obtained in the same way.

$$Y(s) = H(s)X(s) \quad (3.18)$$

$$Y(s) = \int_0^{\infty} y(t) e^{-st} dt \quad (3.19)$$

$$Y(k) = \frac{T}{2n} \sum_{m=1}^{2n} e^{-\alpha t_m} y_0(t_m) e^{-j \frac{(2k-1)(2m-1)}{4n} \pi} \quad (3.20)$$

The Laplace transform of the original waveform of the blast wave, $X(k)$, is written in Eq. (3.21).

$$X(k) = \operatorname{Re}[X(k)] + j \operatorname{Im}[X(k)] \quad (3.21)$$

Using Eqs. (3.16) – (3.18),

$$\operatorname{Re}[X(k)] = \operatorname{Re}[Y(k)]\operatorname{Re}\left[\frac{1}{H(k)}\right] - \operatorname{Im}[Y(k)]\operatorname{Im}\left[\frac{1}{H(k)}\right] \quad (3.22)$$

$$\operatorname{Im}[X(k)] = \operatorname{Re}[Y(k)]\operatorname{Im}\left[\frac{1}{H(k)}\right] + \operatorname{Im}[Y(k)]\operatorname{Re}\left[\frac{1}{H(k)}\right] \quad (3.23)$$

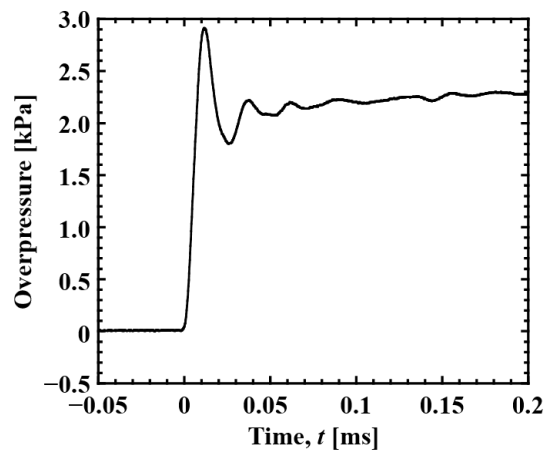
Finally, the inverse discrete Laplace transform is applied to $X(k)$ to recover the original waveform of the blast wave, $x(t_m)$.

$$\begin{aligned} x(t_m) &= \frac{2e^{\alpha t_m}}{T} \operatorname{Re} \left[\sum_{k=1}^n X(k) e^{j \frac{(2k-1)(2m-1)}{4n} \pi} \right] \\ &= \frac{2e^{\alpha t_m}}{T} \sum_{k=1}^n \left\{ \operatorname{Re}[X(k)] \cos \frac{(2k-1)(2m-1)}{4n} \pi \right. \\ &\quad \left. - \operatorname{Im}[X(k)] \sin \frac{(2k-1)(2m-1)}{4n} \pi \right\} \end{aligned} \quad (3.24)$$

In this study, the microphones were not set in a completely symmetrical orientation because of the difficulty of the field experiment; this resulted in spatial errors of approximately 10 mm. These errors caused differences in the arrival times of the blast waves at each microphone. Therefore, the time at which the blast wave arrived at each microphone was set to $t = 0$ initially, such that the origins of the time axis of each waveform were unified. In this study, the arrival time of the blast wave was defined as the time when the pressure gradient dP/dt was maximum. Then, the waveforms that unified the standard of the time axis were deconvoluted in the range $-0.1 \leq t \leq 1.7$ ms, and fitted by B-spline functions.

Table 3.3 Nomenclatures in deconvolution process.

Symbol	Definition	Laplace transform
k, m	Integer	
t, t_m	Time, Time in discrete	
s, s_k	Complex, Complex in discrete	
$2n$	Number of time step	
ΔP_0	Overpressure of planar shock wave	
$\Delta\omega$	Angular frequency division	
α	Coefficient	
$h(t)$	Device function of microphone	$H(s)$
$x_0(t)$	Ideal waveform of planar shock wave	$X_0(s)$
$y_0(t)$	Measured waveform of planar shock wave	$Y_0(s)$
$x(t)$	Original waveform of blast wave	$X(s)$
$y(t)$	Measured waveform of blast wave	$Y(s)$

Figure 3.9 Waveform of planar shock wave measured by microphone, $y_0(t)$.

3.3 Effect of local turbulent flow on overpressure behind blast wave

3.3.1 Effect on pressure waveform

Figure 3.10 shows typical examples of a measured waveform in the case without flow (“rough waveform,” corresponding to $y(t)$ in Section 3.2.3), and the waveform recovered from the rough waveform by the deconvolution process (“processed waveform,” corresponding to $x(t)$ in Section 3.2.3). In the rising of the blast wave, the rough waveform had an overshoot, which was caused because an impact of the blast wave was suddenly applied to the microphone. However, by using the deconvolution process, the processed waveform recovered the original waveform similar to the Friedlander waveform (Friedlander, 1946; Goel et al., 2012), which is particular to blast wave (see Fig. 3.1). The undershoot just before the rising of the blast wave was caused by the limitation of the record length of the waveform: the function should be integrated in the range between $-\infty$ and ∞ in the definition of the Laplace transform, however in reality, each waveform was discretely integrated in the finite temporal range. The effective rise time, which is the duration between the time to be 10% of the peak overpressure and the time to be 90% of that, of the processed waveform was 9 μs . The value was consistent to the frequency range of up to 100 kHz. The Mach number of the blast wave calculated from the peak overpressure of the processed waveform was $M_s = 1.003$. As the turbulent Mach number of the interacted local turbulent flow was $M_t \approx 2.9 \times 10^{-3}$ as shown in Section 3.2.2, the condition of $M_t \gtrsim 0.6 (M_s - 1)$, in which “broken” wave front was suggested in the numerical study (Larsson et al., 2013), was almost satisfied. In the following sentence, we will discuss the effect of turbulence by using the processed

waveforms.

Figure 3.11 shows typical examples of pressure waveforms in the case with turbulence. The four pressure waveforms were recovered from rough waveforms, which are drawn in dashed lines, measured in the same shot. In comparison to the case without flow (Fig. 3.10, processed waveform), significant modulations of the waveforms occurred just after the rising of the waveforms. Although the effective rise times of waveforms 1 to 4 were 8 to 10 μs , waveform 1 and 2 took a significant amount of time to attain its peak from the start of rising. In waveform 1 it took 18 μs for the overpressure reached a maximum; in waveform 2, 29 μs . This period was two to three times longer than the effective rise time. In waveform 3 and 4, the periods were 9 μs and 10 μs , respectively, which were comparable to the effective rise time. In addition, the peak overpressures were also affected by the turbulence. The peak overpressure of waveform 2 was 0.502 kPa, which was relatively lower. In contrast to waveform 2, waveform 4 had a strong peak overpressure, which was 0.737 kPa, just after the rising. This result was consistent with the general tendency of the shock wave modulation caused by the interaction with velocity fluctuation: relatively large upstream flow velocity of the shock wave induces the increment of the overpressure and the decrease of the rising time, and vice versa. Therefore it indicated that the blast wave was locally modulated by the local velocity fluctuation in the turbulence. In addition, the overpressures in the expansion waves region were also modulated. In waveform 4, the overpressure suddenly decreased with downward convex just after the peak overpressure, similar to the case without flow (Fig. 3.10). On the other hand, in waveform 1 to 3, the overpressure in the expansion waves region maintained relatively high pressure for a longer duration compared to waveforms 4. In particular, waveform 1 had a local peak behind the peak overpressure. This

modulation also appeared locally, only in the case with turbulence. It suggested that the turbulence also affected the overpressure in the region of the expansion waves behind the shock wave.

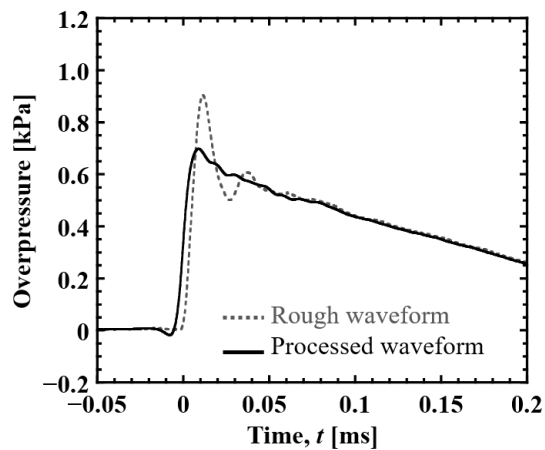


Figure 3.10 Typical example of blast wave measured in the case without flow; processed waveform is recovered from rough waveform by deconvolution.

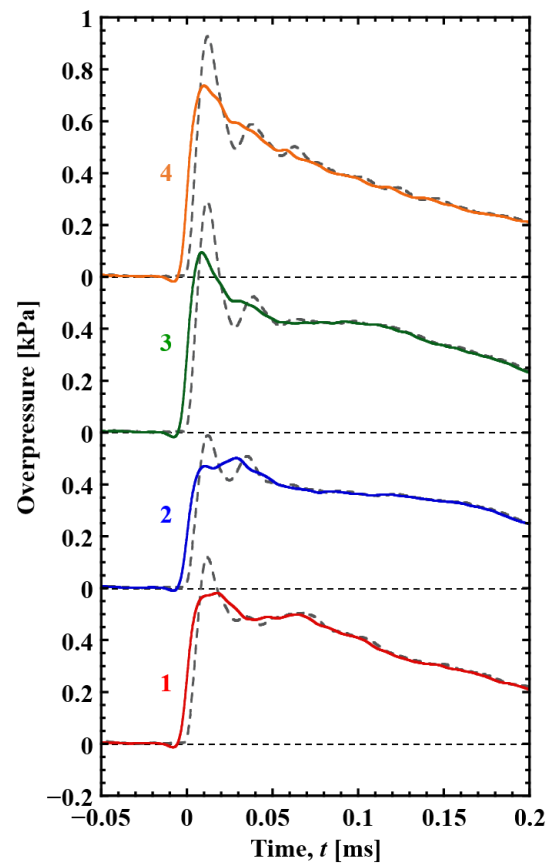


Figure 3.11 Typical examples of processed pressure waveforms in one shot (with turbulence); dashed lines are rough waveforms, 1 to 4 correspond to microphone numbers in Fig. 3.6, each signal are displaced in y -direction by 0.6 kPa.

3.3.2 Evaluation of reproducibility and error of setup

As this study was conducted in a field, experimental data were affected by uncertainty of the location of a blast wave source. In this section, the influences of associated errors will be evaluated.

Let i be the serial shot number of shot ($1 \leq i \leq N$), j be the microphone number ($1 \leq j \leq K$, $K = 4$). Also, let $\Delta P(i, j)$ be the peak overpressure in the i -th shot and at the microphone j . In the case without flow, the shots of $1 \leq i \leq 5$ were performed in Day 1 and those of $6 \leq i \leq 8$ were performed in Day 2. In addition, in the case with turbulence, the shots of $1 \leq i \leq 10$ were performed in Day 1 and those of $11 \leq i \leq 17$ were performed in Day 2 (see Table 3.4). The average overpressures in the i -th shot, $\overline{\Delta P(i)}$, is given by Eq. (3.25).

$$\overline{\Delta P(i)} = \frac{1}{K} \sum_{j=1}^K \Delta P(i, j) \quad (3.25)$$

Let the shots that were conducted in a day be $m \leq i \leq n$. The average overpressure in the day, $\overline{\Delta P}$, and the standard deviation caused by the reproducibility, σ_s , are given by Eqs. (3.26) and (3.27), respectively.

$$\overline{\Delta P} = \frac{1}{n - m + 1} \sum_{i=m}^n \overline{\Delta P(i)} \quad (3.26)$$

$$\sigma_s = \sqrt{\frac{1}{n - m + 1} \sum_{i=m}^n \{\overline{\Delta P(i)} - \overline{\Delta P}\}^2} \quad (3.27)$$

Table 3.4 shows the histories of $\overline{\Delta P(i)}$ for each condition. Table 3.5 shows $\overline{\Delta P}$ and σ_s in the case without flow and with turbulence, respectively. In the case without flow, Table 3.5 (a) shows that the difference between the values of $\overline{\Delta P}$ for Day 1 and Day 2 was approximately 0.1 kPa. The cause of the difference was that the relative positions of

each microphone for the blast wave source had small errors over the two days. Moreover, even for the same day, $\overline{\Delta P(i)}$ varied for each shot, and σ_s was 7% of $\overline{\Delta P}$ in maximum, as shown in Tables 3.4 (a) and 3.5 (a), respectively. The primary cause for σ_s was uncertainty in the mass of the report composition, the direction and position of the paper tube in which the report composition was contained. In the case with turbulence, Table 3.5 (b) shows that $\overline{\Delta P}$ was greater than that in the case without flow for the same day because the propagation through the counter flow caused an increment in the relative Mach number. Under this condition, σ_s was less than 9% of $\overline{\Delta P}$ in maximum. Although the ratio of σ_s for $\overline{\Delta P}$ was 30% greater than that in the case without flow, the result indicated that $\overline{\Delta P}$ in this case had reproducibility equal to that in the case without flow.

Table 3.4 Histories of average of overpressures in i -th shot, $\overline{\Delta P(i)}$; serial shot number, i .

(a) without flow			(b) with turbulence		
i	day	$\overline{\Delta P(i)}$ [kPa]	i	day	$\overline{\Delta P(i)}$ [kPa]
1	Day 1	0.715	1	Day 1	0.629
2		0.687	2		0.769
3		0.654	3		0.726
4		0.676	4		0.718
5		0.583	5		0.719
6	Day 2	0.720	6		0.673
7		0.798	7		0.576
8		0.794	8		0.698
			9		0.618
			10		0.591
			11	Day 2	0.806
			12		0.897
			13		0.889
			14		0.945
			15		0.933
			16		0.935
			17		0.875

Table 3.5 Average overpressure in a day, $\overline{\Delta P}$, and standard deviation caused by reproducibility, σ_s .

	(a) without flow		(b) with turbulence	
	Day 1 ($1 \leq i \leq 5$)	Day 2 ($6 \leq i \leq 8$)	Day 1 ($1 \leq i \leq 10$)	Day 2 ($11 \leq i \leq 17$)
$\overline{\Delta P}$ [kPa]	0.663	0.771	0.672	0.897
σ_s [kPa]	0.045	0.036	0.062	0.044

3.3.3 Effect on standard deviation of peak overpressure

In this section, the effect of the local turbulence on the blast wave is evaluated. To extract the effect only of the turbulence, $\Delta P(i, j)$ is standardized by $\overline{\Delta P(i)}$ in each shot. The standardized peak overpressure, $\widetilde{\Delta P(i, j)}$, is given by Eq. (3.28).

$$\widetilde{\Delta P(i, j)} = \frac{\Delta P(i, j)}{\overline{\Delta P(i)}} \quad (3.28)$$

The average of the entire $\widetilde{\Delta P(i, j)}$ is unity. Using Eq. (3.28), the standard deviation caused by the local modulation of the standardized peak overpressures, $\tilde{\sigma}_t$, is given by Eq. (3.29).

$$\tilde{\sigma}_t = \sqrt{\frac{1}{KN} \sum_{i=1}^N \sum_{j=1}^K \{\widetilde{\Delta P(i, j)} - 1\}^2} \quad (3.29)$$

Figure 3.12 shows the distributions of $\widetilde{\Delta P(i, j)}$ in each shot and at each microphone. The gray belts in Fig. 3.12 represent the width of $2\tilde{\sigma}_t$. In the case without flow (Fig. 3.12 (a)), the standard deviation in $\widetilde{\Delta P(i, j)}$ was relatively small, $\tilde{\sigma}_t = 0.016$, which was 2% of the average of the entire $\widetilde{\Delta P(i, j)}$. One of possible reasons why $\tilde{\sigma}_t$ was not zero is that it was affected by the turbulence induced by the natural wind before performing the shot, and the non-uniform distribution of atmospheric temperature. However, the result indicated that the blast waves propagated almost uniformly.

In contrast, in the case with turbulence, Fig. 3.12 (b) shows that $\widetilde{\Delta P(i, j)}$ greatly scattered in each shot and at each microphone. Focusing on the individual peak overpressures, $\widetilde{\Delta P(i, j)}$ at each microphone greatly varied for different shots, and the variations in each microphone were obviously larger than those in the case without flow. For example, at the microphone 1, $\widetilde{\Delta P(i, 1)}$ was greater than the average $\overline{\widetilde{\Delta P(i, j)}} = 1$ when $i = 2, 5, 7, 8, 12, 13, 14$ and 17, while $\widetilde{\Delta P(i, 1)}$ was less than the average in the

other shots. In addition, the relationships between the magnitude of each $\Delta\overline{P}(i, j)$ also varied shot by shot because of the turbulence interaction. For example, in the case without flow, every $\Delta\overline{P}(i, 1)$ were greater than $\Delta\overline{P}(i, 4)$ in a same shot. However, in the case with turbulence, this relationship did not hold: $\Delta\overline{P}(i, 1)$ was greater than $\Delta\overline{P}(i, 4)$ when $i = 2, 5, 7, 12$ and 16 , while $\Delta\overline{P}(i, 1)$ was less than $\Delta\overline{P}(i, 4)$ in the other shots. The inversion of $\Delta\overline{P}(i, j)$ randomly appeared between each microphone, and its pressure difference in a same shot also varied shot by shot in random manner. As described in Section 3.3.1, the local modulations of the peak overpressure were caused by the local difference of the upstream flow velocity of the blast wave: relatively large upstream flow velocity induced higher peak overpressure than the average, and vice versa. These local difference of the upstream flow velocity randomly existed in turbulent flow, therefore such peak overpressure modulation appeared in random manner. As a result, the standard deviation in $\Delta\overline{P}(i, j)$ was $\tilde{\sigma}_t = 0.110$, which was 11% of the average of the entire $\Delta\overline{P}(i, j)$. This value was quite large compared to the value obtained in the case without flow; $\tilde{\sigma}_t$ in this case was 7 times larger than that without flow.

On the other hand, $\Delta\overline{P}(i, j)$ obtained at each microphone had non-negligible deviations. For example, most of $\Delta\overline{P}(i, 2)$ in Day 1 and $\Delta\overline{P}(i, 3)$ in Day 2 were distributed in the region less than $\Delta\overline{P}(i, j) = 1.0$, which is the average of the entire $\Delta\overline{P}(i, j)$. In contrast, most of $\Delta\overline{P}(i, 4)$ in Days 1 and 2 were greater than $\Delta\overline{P}(i, j) = 1.0$. It can be explained by the following reason; the installation error of the blower in the turbulence generator caused non-uniformity of the average flow, which affected the relative Mach numbers of the blast waves. In practice, the distortion of the averaged flow velocity was observed in the measurement of the turbulence characteristics conducted in an indoor laboratory, as shown in Table 3.2. However, the results mentioned above clearly

indicated that the peak overpressure of the blast waves were locally and randomly modulated by the interaction with the local turbulent flow.

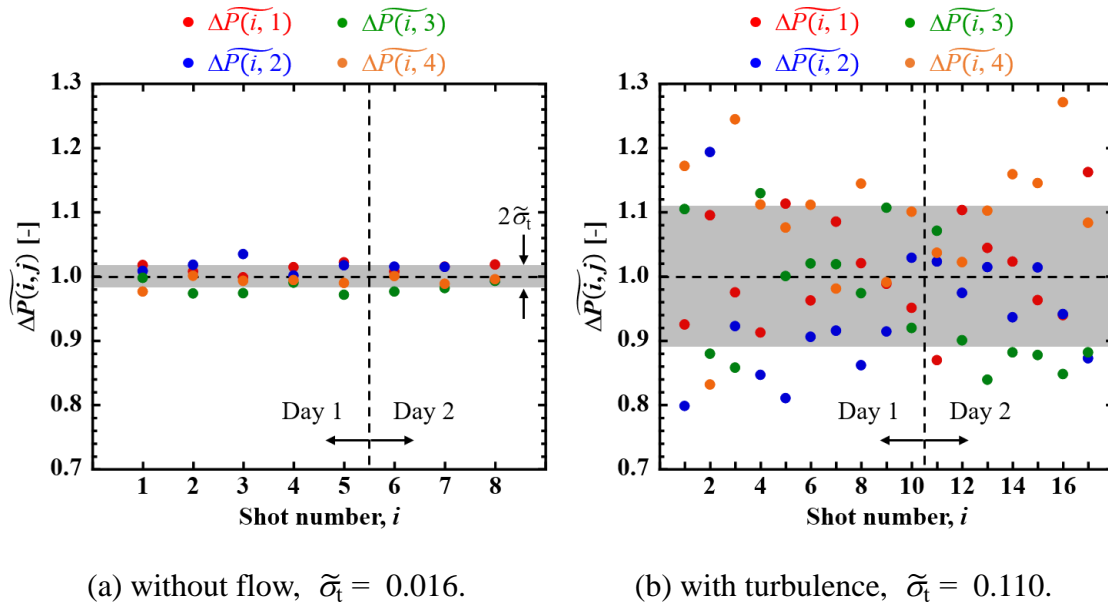


Figure 3.12 Distribution of standardized peak overpressure, $\Delta\overline{P}(i, j)$; the standard deviation of standardized peak overpressure, $\tilde{\sigma}_t$; j corresponds to microphone numbers in Fig. 3.6.

3.4 Summary of this chapter

In this chapter, the effect of the interaction with a local turbulent flow on the overpressure of the weak blast wave with large curvature radius was investigated.

- An experimental system for the investigation was developed in a field. Using the system, multipoint pressure measurements were conducted in the case without flow and with turbulence, in which the condition of “broken shock” criteria was almost satisfied.
- The modulation of the pressure field behind the blast wave caused by the interaction with local turbulent flow were observed. It indicated that the peak overpressure of the blast waves were modulated through the interaction with the local turbulent flow.
- The pressure waveforms without flow were similar to the Friedlander waveform. The standard deviation in peak overpressure was 2% of the ensemble average of the peak overpressure.
- With local turbulent flow, the pressure waveforms were modulated: the peak overpressure and the period to reach its peak overpressure from the start of the rising were randomly and locally varied shot by shot. The standard deviation due to the effect of the turbulence interaction was 11% of the average of the standardized peak overpressure, which was 7 times larger than that without flow.

Chapter 4

Development of counter-driver shock tube and planar shock wave-grid turbulence interaction

4.1 Method to investigate interaction between planar shock wave and isotropic turbulence

To investigate phenomena related to turbulence, grid turbulence, which is nearly isotropic in a certain region, has been generally applied (Roach, 1987). For fundamental investigation of the interaction between a shock wave and turbulence, it is also suitable to utilize the combination of a planar shock wave, which is not decay with propagation distance, and grid turbulence. However, it is difficult to apply both of them to the experimental investigation of the shock wave-turbulence interaction, as shown in Section 3.1.2. In Chapter 3, a quasi-planar blast wave, of which the attenuation was negligible, was applied to the evaluation using a large scale system, however expansion waves followed the shock wave front and there still exists difficulty in usage of grid turbulence in such a field. Some researchers used shock tubes to evaluate the effects of the interactions on a shock wave and grid turbulence (Dosanjh, 1956; Keller and Merzkirch, 1990). The grid turbulence was generated by disturbing uniform flow behind an incident shock wave that passed through a grid, and it interacted with a reflected shock wave

formed by the shock wave reflection on the end wall of the shock tube. Although the interaction between a planar shock wave and grid turbulence was realized in the shock tubes, the experimental conditions were quite limited because the shock wave and the grid turbulence were not independent. However, a shock tube has the potential to become an useful facility to investigate the shock wave-turbulence interaction if we overcome the limitation using some techniques.

A shock tube is a basic tool for experimentally investigating shock wave phenomena. It utilizes the beneficial characteristic that a shock wave is naturally stable (Landau and Lifshitz, 1987). A planar shock wave can be generated in a straight tube (a “shock tube”), which is separated into high-pressure and low-pressure sections. In the low-pressure section, a planar shock wave of interest propagates after the separation between the low- and high-pressure sections is removed. Some effort has gone into further extending the function of a shock tube to investigate the interactions between a shock wave and various flows. Barbosa et al. constructed a “bifurcated” shock tube in which the low-pressure or driven section was bifurcated and then re-unified at the test section (Barbosa and Skews, 2002). The interaction of two planar shock waves colliding with each other at a controlled incident angle was investigated. Some researchers installed porous end walls in the low-pressure sections of shock tubes to weaken the reflected shock wave for the interaction with grid turbulence (Honkan and Andreopoulos, 1992; Honkan et al., 1994; Xanthos et al., 2002; Agui et al., 2005). Weakening the strength of the reflected shock wave by the porous end walls, they succeeded to extend the experimental conditions of the interaction. However, in these studies, the conditions of the interacting shock waves or flows depended on the operation condition of a single driver and the porosity of the porous end wall. Thus, their experimental conditions were still restricted, especially stronger shock

wave than the incident shock wave could not be applied. To set the conditions of the interacting flows independently, two independent drivers are necessary.

In many cases, shock tube operation is initiated by rupturing a diaphragm, which is usually made of plastic or metal depending on the pressure difference of the operation. If it has a single driver, temporal control of the diaphragm rupture is not necessary. The diaphragm can be ruptured by manually driving a needle through it or by using a so-called “double diaphragm” (Oertel, 1966), in which the gas in a middle-pressure section is manually released. However, when two drivers are used, temporal control of the two driver operations is necessary.

Therefore, we develop a shock tube, which has two counter driver sections with a temporally controlled actuation system. Hereafter, we will refer to the shock tube as a “counter-driver shock tube (CD-ST).” Using two counter-drivers, the interaction between a planar shock wave and a counter turbulent flow can be realized while controlling their conditions independently. Moreover, in this facility, we can also control the interaction length by adjusting the actuation timing of the drivers, although its effect has not been investigated yet in both experimental and numerical studies. This chapter describes the development of the CD-ST, and interaction experiments between planar shock wave and grid turbulence conducted using the CD-ST are discussed.

4.2 Operation principle of counter-driver shock tube

Figure 4.1 schematically illustrates the configuration and operation of the CD-ST. (a) Initially, the inside of a straight tube is subdivided into three sections: “L (left)-Driver,” “Driven,” and “R (right)-Driver.” As shown in Fig. 4.1(a), the initial state of each section

is labelled as “4L,” “1,” and “4R,” respectively. The ends of the Driven section have separators to the L-Driver and the R-Driver sections. The separator openings are actively controlled so that the shock waves and post-shock flows from both ends meet, and their interactions are diagnosed at the test area of the Driven section. Although its basic configuration is symmetrical, in this study, we consider that the L-Driver starts first, followed by the R-Driver. (b) After the separator for the L-Driver section opens, a right-running, incident shock wave, L-iSW, propagates in the Driven section, and its post-shock flow, L-PSF (state “2L”), follows behind L-iSW and ahead of the contact surface, L-CS. (c) After a delay time, the separator for the R-Driver section opens, a left-running, incident shock wave, R-iSW, propagates in the Driven section, and its post-shock flow, R-PSF (state “2R”), follows behind R-iSW and ahead of the contact surface, R-CS. (d) Then, the two incident shock waves collide. (e) After the collision, two transmitted shock waves, the right-running (L-tSW) and left-running (R-tSW) shock waves, are generated, along with a contact surface, CS (Glass, 1994). (f) Then, R-tSW interacts with L-PSF, and L-tSW interacts with R-PSF.

In a shock tube operation, the condition of each state is determined from the well-known shock tube relations based on the Riemann problem. Following the tradition, the states in the shock tube operation are labelled as shown in Figs. 4.1, 4.8 and 4.13. The initial operation conditions of the CD-ST are fully set by specifying the pressure, P , speed of sound, a , and specific heat, γ , in each section. P_{2L} is obtained from the implicit Eq. (4.1).

$$\frac{P_{4L}}{P_1} = \frac{P_{2L}}{P_1} \left\{ 1 - \frac{(\gamma_{4L} - 1) \frac{a_1}{a_{4L}} \left(\frac{P_{2L}}{P_1} - 1 \right)}{\sqrt{2\gamma_1 [2\gamma_1 + (\gamma_1 + 1) \left(\frac{P_{2L}}{P_1} - 1 \right)]}} \right\}^{-\frac{2\gamma_{4L}}{\gamma_{4L} - 1}} \quad (4.1)$$

Here a flow speed is designated by u . Using P_{2L} , u_{2L} and a_{2L} are given as

$$u_{2L} = a_1 \left(\frac{P_{2L}}{P_1} \right) \sqrt{\frac{\frac{2}{\gamma_1(\gamma_1+1)}}{\frac{P_{2L}}{P_1} + \frac{\gamma_1-1}{\gamma_1+1}}} \quad (4.2)$$

$$a_{2L} = a_1 \frac{P_{2L}}{P_1} \cdot \frac{\frac{\gamma_1-1}{\gamma_1+1} \frac{P_{2L}}{P_1} + 1}{\frac{P_{2L}}{P_1} + \frac{\gamma_1-1}{\gamma_1+1}} \quad (4.3)$$

The condition of the state 2R is also determined as follows.

$$\frac{P_{4R}}{P_1} = \frac{P_{2R}}{P_1} \left\{ 1 - \frac{(\gamma_{4R}-1) \frac{a_1}{a_{4R}} \left(\frac{P_{2R}}{P_1} - 1 \right)}{\sqrt{2\gamma_1 [2\gamma_1 + (\gamma_1+1) \left(\frac{P_{2R}}{P_1} - 1 \right)]}} \right\}^{\frac{2\gamma_{4R}}{\gamma_{4R}-1}} \quad (4.4)$$

$$u_{2R} = -a_1 \left(\frac{P_{2R}}{P_1} \right) \sqrt{\frac{\frac{2}{\gamma_1(\gamma_1+1)}}{\frac{P_{2R}}{P_1} + \frac{\gamma_1-1}{\gamma_1+1}}} \quad (4.5)$$

$$a_{2R} = a_1 \frac{P_{2R}}{P_1} \cdot \frac{\frac{\gamma_1-1}{\gamma_1+1} \frac{P_{2R}}{P_1} + 1}{\frac{P_{2R}}{P_1} + \frac{\gamma_1-1}{\gamma_1+1}} \quad (4.6)$$

After the collision of L-iSW and R-iSW, it is assumed that transmitted shock waves, L-tSW and R-tSW, and a contact surface, CS, are generated; the state between R-tSW and CS is labelled as "5R," and CS and L-tSW as "5L." u_{5L} and u_{5R} are given by

$$u_{5L} - u_{2R} = -a_{2R} \left(\frac{P_{5L}}{P_{2R}} \right) \sqrt{\frac{\frac{2}{\gamma_1(\gamma_1+1)}}{\frac{P_{5L}}{P_{2R}} + \frac{\gamma_1-1}{\gamma_1+1}}} \quad (4.7)$$

$$u_{5R} - u_{2L} = a_{2L} \left(\frac{P_{5R}}{P_{2L}} \right) \sqrt{\frac{\frac{2}{\gamma_1(\gamma_1+1)}}{\frac{P_{5R}}{P_{2L}} + \frac{\gamma_1-1}{\gamma_1+1}}} \quad (4.8)$$

The boundary conditions of the contact surface are

$$u_{5R} = u_{5L} \quad (4.9)$$

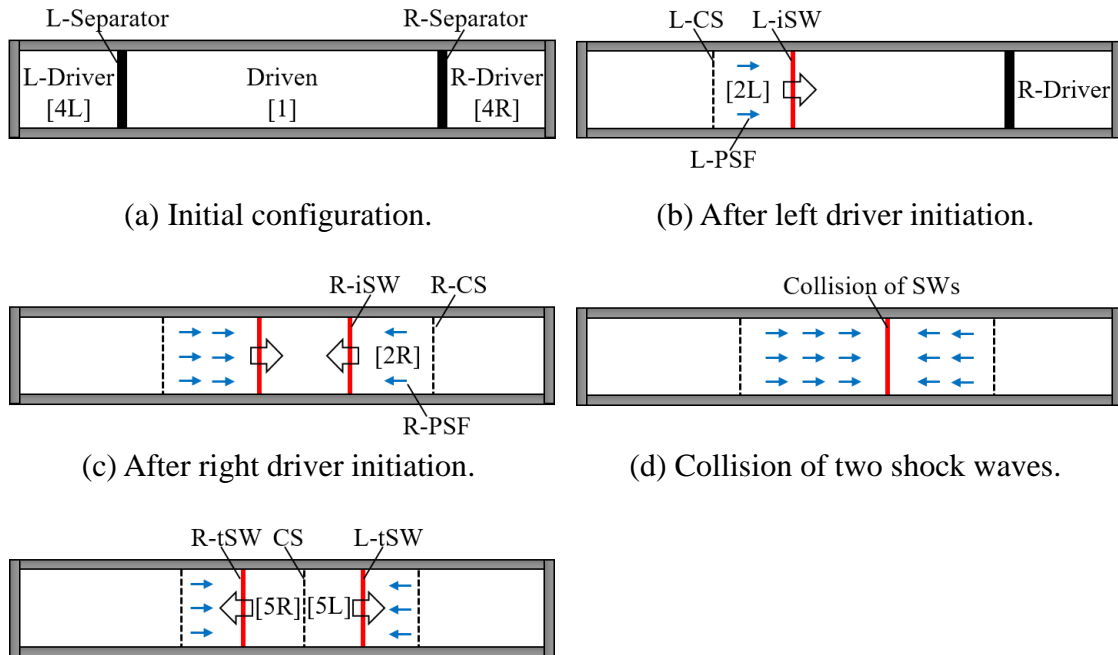
$$P_{5R} = P_{5L} \equiv P_5 \quad (4.10)$$

P_5 is uniquely determined by Eqs. (4.7) – (4.10), and the shock Mach number of R-tSW, M_s , is obtained by

$$M_s = \sqrt{\frac{\gamma_1 + 1}{2\gamma_1} \frac{P_5}{P_{2L}} + \frac{\gamma_1 + 1}{2\gamma_1}} \quad (4.11)$$

Test flow condition, that is the combination of P_{2L} , u_{2L} and M_s , is given by Eqs. (4.1), (4.2) and (4.11).

Figure 4.2 shows the operation map of the CD-ST in $P_{4L}/P_1 - P_{4R}/P_{4L}$ coordinate. The solid lines are contours of M_s , and the vertical broken lines indicate u_{2L} , which are calculated using the above equations. The horizontal broken line $P_{4R}/P_{4L} = 1$ corresponds to the reflected shock wave from a solid end wall in a single driver shock tube (Dosanjh, 1956; Keller and Merzkirch, 1990). The gray region, $P_{4R}/P_{4L} < 1$, can be realized by using a porous end wall in a single driver shock tube (Honkan and Andreopoulos, 1992; Honkan et al., 1994; Xanthos et al., 2002; Agui et al., 2005). However, the effective value of P_{4R}/P_{4L} is set only in a discrete manner because it depends on the porosity of the porous end wall. The region of $P_{4R}/P_{4L} > 1$ is realized by only using the CD-ST. For a value of u_{2L} , which is determined by P_{4L}/P_1 , any value of M_s can be obtained by tuning P_{4R}/P_{4L} within its operational condition.



(e) Interactions between a post-shock flow and a transmitted shock wave. The direction of the contact surface depends on the operation conditions.

Figure 4.1 Configuration and operation of counter-driver shock tube; left-(driver/driven), L-; right-(driver/driven), R-; incident shock wave, iSW; transmitted shock wave, tSW; contact surface, CS; post-shock flow, PSF.

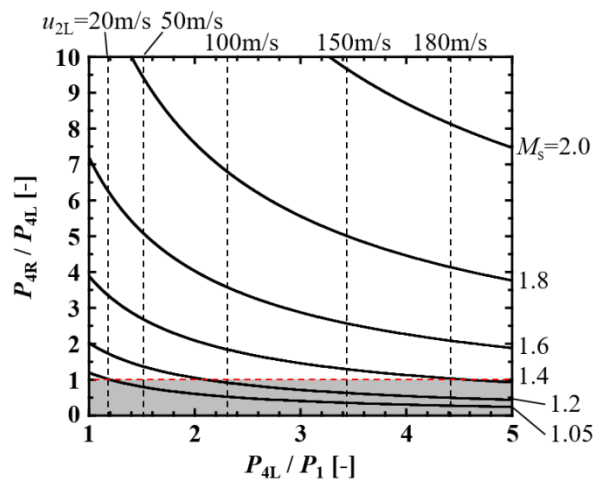


Figure 4.2 Contours of counter flow speed, u_{2L} , and shock Mach number, M_s , on $P_{4L}/P_1 - P_{4R}/P_{4L}$ coordinates; $\gamma_{4L} = \gamma_1 = \gamma_{4R} = 1.4$, $a_{4L} = a_1 = a_{4R} = 340$ m/s.

4.3 Technical details

4.3.1 Diaphragm rupture

There exist several types of shock tube drivers in which the temporal control of operation is possible. “Oguchi piston” (Oguchi et al., 1991) is useful because no diaphragm fragments are produced by a run. However, the uniformity of the post-shock flow is contaminated by the relatively slow motion of the piston (White, 1958; Simpson et al., 1967; Ikui and Matsuo, 1969; Hickman et al., 1975); the complicated flow passage past the piston worsens the performance. The mass of the separation element can be decreased by replacing the free piston with a thin rubber membranes (Yang et al., 1994 and 1996). However, with this rubber membrane, the driver and test sections are not connected in a straight tube, which induces pressure loss, flow non-uniformity, and unsteadiness. Active rupture of the diaphragm by electromagnetic force (Miller, 1977) or laser pulse (Sasoh et al., 2006) induces pressure disturbance that contaminates the test flow.

To generate ideal planar shock wave and uniform flow behind it, the following requirements should be satisfied: (1) small pressure loss, and (2) short opening time. In this study, we initiated shock tube operation by rupturing a layer (or layers) of cellophane diaphragm with a needle driven by a pneumatic piston. This method satisfied these requirements as well as the following conditions: (3) small pressure difference is allowed and large pressure difference can be covered by layering (from several kilopascals to about 30 kPa with a layer of 18- μm -thick diaphragm for $120 \times 120 \text{ mm}^2$ square cross section), and (4) simple and safe.

Figure 4.3 illustrates the pneumatic diaphragm rupture device developed in this study.

One layer (or multiple layers) of cellophane used as a diaphragm (thickness: 18 or 36 μm) was sandwiched between two shock tube flanges, and set at a driver-driven connection. O-ring seals were used at both surfaces of the diaphragm. A pneumatic piston (CJ2B10-60A or CJ2B10-60AZ, SMC Co.) was set on the center axis of the shock tube using struts. A piston rod (diameter 4 mm) was held in the cylinder with smooth contact and sufficient hermetic sealing. A stainless steel (SUS304) needle was attached to the tip of the piston rod. This needle had a diameter of 5 mm and a full apex angle of 90° . The piston rod was driven by high-pressure air (pressure 500 – 700 kPa) to a full stroke of 60 mm within 60 ms (nominal value). The driver air was supplied through two 4.0-mm (outside diameter) polyurethane tubes connected to a high-pressure air reservoir via a five-port electromagnetic valve (SY-3220, SMC Co.). Before a run (Fig. 4.3 (a)), the high-pressure air was connected to the “Pull” line, with the piston rod set at the bottom. By supplying the high-pressure air to the “Push” line (Fig. 4.3 (b)), the piston was pushed to crack the diaphragm within a period of 7 ms, which was estimated using the initial separation distance and nominal piston speed. The transition from “Pull” to “Push” was done using an electrical trigger signal to the electromagnetic valve. If the effective delay time for the diaphragm rupture was well calibrated, this diaphragm rupture operation could be synchronized with that of the other driver and various electrical instruments.

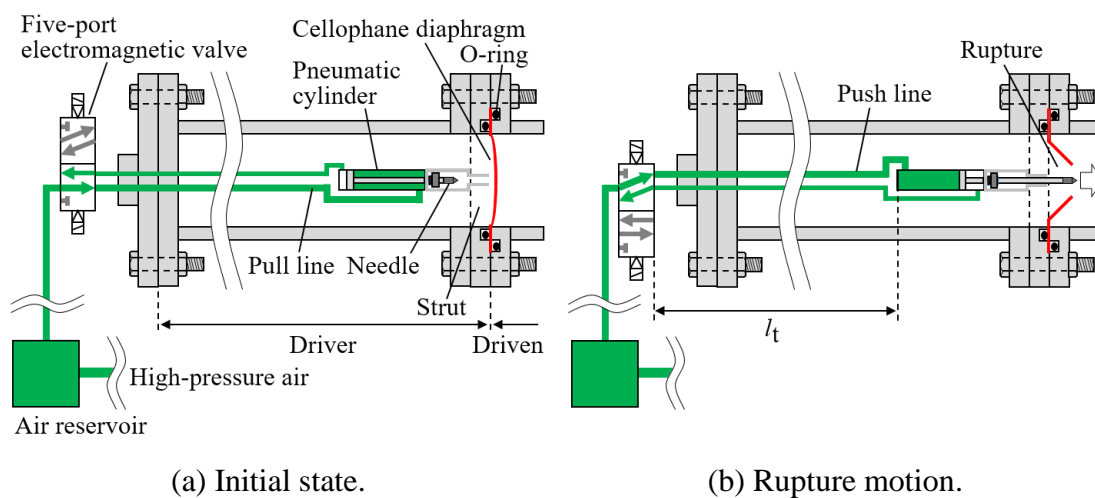


Figure 4.3 Pneumatic diaphragm rupture device; length of connection tube, l_t .

4.3.2 Weakening of interacting shock wave

The strength of the planar shock wave in a shock tube can be controlled by an initial condition, which is the ratio of driver pressure, P_4 , and driven pressure, P_1 . However, it is generally difficult to generate a weak planar shock wave in a shock tube: when P_4/P_1 is set to a small value to form a weak shock wave, the pressure difference $P_4 - P_1$ becomes too small to rupture the diaphragm and the formation of an ideal planar shock wave fails. In this study, to expand the operation condition, a method to generate a weak planar shock wave was developed using shock attenuation in a porous wall. Britan et al. reported that solid plates with holes or slit reduced the overpressure of the shock wave while the rising of the shock wave remained sharp (Britan et al., 2006). However, using a porous foam, which is compressible, the shock wave was attenuated and degenerated into compression waves (Kitagawa et al., 2006). Therefore, in this study, the porous wall was composed of layers of rigid punched plates, and its attenuation performance was evaluated in a preliminary experiment. In the experiment, 16 layers of solid punched

plates (diameter of punched hole, 1 mm; thickness of punched plate, 1 mm; solidity, 82.5%) with an interval of 1 mm were used for the porous wall.

The porous wall was installed at $x = 5020$ mm in the $120 \text{ mm} \times 120 \text{ mm}$ square CD-ST described in Section 4.4.2. Figure 4.4 shows overpressure histories obtained in the preliminary experiment to demonstrate weak shock wave generation using the porous wall. In this experiment, the shock tube was operated in a single-driver configuration using the Driven and R-Driver section. The initial condition was set to $P_{4R} = 50.0$ kPa and $P_1 = 43.0$ kPa, which was almost a minimum pressure difference to generate a planar shock wave in the shock tube. At the position before the porous wall, two shock waves, an incident shock wave and a reflected shock wave from the porous wall, were obtained (Fig. 4.4 (a)). The shock Mach number of the incident shock wave calculated from the overpressure was $M_s = 1.03$. At the position after the porous wall, a transmitted shock wave was observed (Fig. 4.4 (b)). What is important to note here is that the transmitted shock wave was obviously a planar shock wave, having a sharp rising and constant static pressure behind the shock wave. The post-shock pressure was approximately 2 kPa lower than that of the incident shock wave, and the shock Mach number calculated from the overpressure was $M_s = 1.01$, which has never been realized, until hitherto, without a porous wall.

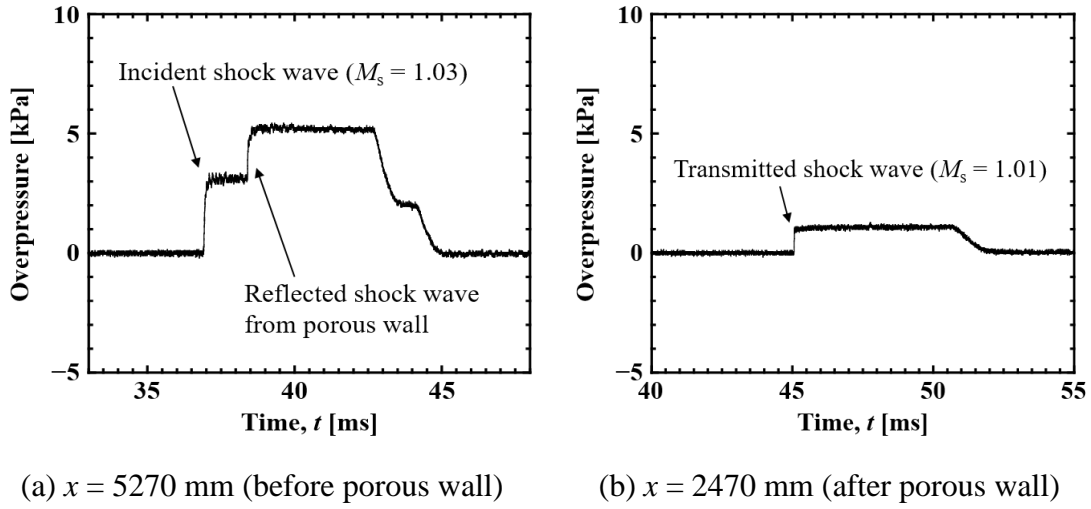


Figure 4.4 Overpressure histories obtained in preliminary experiment of weak planar shock wave generation, using R-Driver and Driven section of 120 mm \times 120 mm square CD-ST described in Section 4.4.2; porous wall was installed at $x = 5020$ mm; $P_{4R} = 50.0$ kPa, $P_1 = 43.0$ kPa.

4.3.3 Calibration of hot-wire anemometer

Constant temperature hot-wire anemometer is a useful tool for investigations of turbulence because it can detect flow velocity with high temporal resolution. For accurate measurements, it is necessary to obtain calibration curves for individual probes. However, for measurements in compressible flow, the calibration becomes difficult because the output voltage of hot-wire anemometer, E , is not only a function of velocity, U , but also density, ρ , and static temperature, T_s , of the fluid in the strict sense. The exact equation of the output is

$$E^2 = \left\{ A \left(\frac{T_f}{T_1} \right)^a + B \left(\frac{T_f}{T_1} \right)^b (\rho U)^n \right\} (T_w - T_f) \quad (4.12)$$

$$T_f = T_s + U^2 / (2C_p) \quad (4.13)$$

where T_w is the temperature of hot-wire probe, T_1 is the reference temperature, C_p is the specific heat at constant pressure, and A , B , a , b , n are constants (Briassulis et al.,

1995). To calibrate the hot-wire anemometer, Eq. (4.12) is simplified using the following assumption: if we consider the flow field behind a planar shock wave, with a constant shock Mach number, M_s , and constant ambient temperature, T_1 , the flow velocity, u_2 , and the static temperature behind the shock wave, T_2 , also become constant. It should be noted that the density behind the shock wave, ρ_2 , is the function of M_s and the initial density, ρ_1 , which is the density of the driven section.

$$\rho_2 = \rho_1 \frac{(\gamma + 1)M_s^2}{(\gamma - 1)M_s^2 + 2} \quad (4.14)$$

Substituting ρ_2 , u_2 and T_2 for ρ , U and T_s in Eqs. (4.12) and (4.13), respectively, Eq. (4.12) can be rewritten as Eq. (4.15) below.

$$E^2 = A' + B'(\rho_2 u_2)^n \quad (4.15)$$

where A' , B' and n are constant values, as described in Eqs. (4.16) and (4.17).

$$A' = A \left(\frac{T_f}{T_1} \right)^a (T_w - T_f) \quad (4.16)$$

$$B' = B \left(\frac{T_f}{T_1} \right)^b (T_w - T_f) \quad (4.17)$$

As shown Eq. (4.14), ρ_2 can be controlled by setting the initial condition of the driven section even with the constant M_s , therefore the relation between the mass flux, $\rho_2 u_2$, and the output of hot-wire anemometer, E , can be obtained. Figure 4.5 shows examples of calibration curves obtained by this method. In this chapter, a combination of a hot-wire anemometer (Model 1011, KANOMAX JAPAN Inc.) and a hand-made I-type probe was used for the measurement. The probe of the hot-wire anemometer was tungsten wire with the length $l_w = 1$ mm and the diameter $d_w = 5$ μm such that $l_w/d_w = 200$, for high frequency response and spatial resolution. When a flow with a mean flow velocity $U = 100$ m/s is measured using the probe, the maximum frequency resolution is roughly evaluated as $U/l_w = 100$ kHz. An important point to note here is that the calibration

curve should be obtained for the static temperature of the flow, where the probe of the hot-wire anemometer measures, because the constant values in Eq. (4.15) depends on the flow temperature.

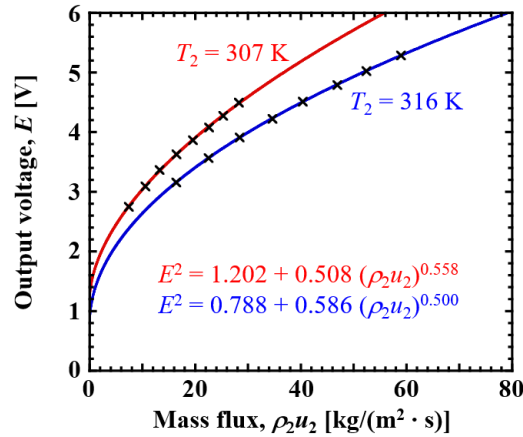


Figure 4.5 Examples of calibration curves for each T_2 , calibrated by shock waves with the shock Mach numbers of 1.05 and 1.10.

4.4 Operation performance

4.4.1 Proof of principle

Figure 4.6 shows the shock tube for the CD-ST concept demonstration and associated control and measurement systems developed in this study. Originally, the shock tube was manufactured as an ordinary single-driver device with a circular cross-section (inner diameter 70 mm). The 4015-mm-long circular tube on the left side includes the 1515-mm-long “L (left)-Driver.” To extend it, tubes with an inner square cross-section (62 mm × 62 mm) were added to the right end of the circular tube with a 200-mm-long transition section. The square tube part was subdivided into the “R (right)-Driver” section (515 mm in length) and the 1015-mm-long “Driven” section. At the test section, a pair of

acrylic windows was set for flow visualization (not used in this study). Six piezoelectric pressure transducers, G1 to G6, (either 113B27, H112A21, or HM102A18, PCB Piezotronics Inc.; rise time 1 – 2 μ s) were flush-mounted on the inner wall of the shock tube so that local shock speeds and overpressure histories could be measured.

The high-pressure air supplied to the pneumatic cylinders was set to 500 kPa in the demonstration experiment. TTL operation signals to each diaphragm rupture device was supplied from a pulse generator. Each TTL signal was sent to a photocoupler, which in turn output a 24-V signal to drive an electromagnetic valve to operate the diaphragm rupture device. The relative delay time, τ , which is the time difference between the output of each TTL signal as described in Fig.4.6, could be determined from the calibrated operation characteristics of each diaphragm rupture device. The control and measured signals were recorded in a digital memory scope.

To produce shock wave-counter flow interactions of interest at a desired location, the synchronization between the left and right driver operations needed to be well controlled. For this purpose, calibration experiments to determine an effective delay time for each diaphragm rupture device were conducted. From the moment that an operation signal from the pulse generator was output, ignoring the propagation periods for the electrical signals, there were three delay components in series that determined the effective delay time: (1) the opening time for the electromagnetic valve, τ_1 ; (2) the pressure propagation period from the electromagnetic valve to the pneumatic cylinder, τ_2 ; (3) the period for the translational motion of the piston rod, τ_3 . Here, the duration time for the diaphragm rupture itself was assumed to be negligible. The nominal value of τ_1 (= 12 ms) was given by the manufacturer, and τ_3 (= 7 ms) was estimated as mentioned in Section 4.3.1, and they are assumed to be the same in the following analysis.

The effective value of τ_2 was determined experimentally under the assumption that it was proportional to the length of the connecting tubes from the electromagnetic valve to the pneumatic cylinder, l_t . It should be noted that the l_t is greater than the length of the drivers because the tubes connect the pneumatic cylinders installed next to the diaphragms and the electromagnetic valves put outside of the drivers. In Fig. 4.7, experimentally measured shock wave diagrams are plotted with the time origin, $t = 0$, being the instant of a trigger signal from the pulse generator, and the spatial origin, $x = 0$, being the diaphragm location. The shock wave trajectory was extrapolated with a constant wave speed. The moment of diaphragm rupture, t_r , was defined as the intersection of the shock wave trajectory and diaphragm location. The jitter of t_r was less than 1.1 ms. From each diagram, τ_2 is obtained by

$$\tau_2 = t_r - \tau_1 - \tau_3 \quad (4.18)$$

It is assumed that

$$\tau_2 = k \frac{l_t}{a} \quad (4.19)$$

where k and a denote a constant and the speed of sound of the high-pressure air, respectively. Equating the value of τ_2 obtained from the operation diagrams of Fig. 4.7 using Eqs. (4.18) and (4.19) with $a = 340$ m/s and $l_t = 2.0$ m for the left driver and $l_t = 1.1$ m for the right driver, respectively, k is fitted to be 7.4 ± 0.4 .

Figures 4.8 and 4.9 present an example of a wave diagram and the pressure histories obtained in a counter-driver operation, respectively. Here, the origins of x and t are the diaphragm location for the L-Driver section and the moment of the trigger signal to the L-Driver, respectively. The relative delay time from the L-Driver to the R-Driver, τ , was set to be 20.5 ms. The transitions from compression waves to shock waves from both of the drivers occurred in the driven section. The shock Mach numbers of L-iSW and R-iSW

were 1.04 and 1.30, respectively. These two incident shock waves collide with each other at $x = 3200$ mm and $t = 62.9$ ms. In five test runs, the uncertainty (rms) in determining the location of the interaction was less than 34 mm, which was 1/169 of the whole shock tube length. At $x = 1800$ mm (G2) and $x = 2830$ mm (G3), two pressure jumps are observed, first by L-iSW (A_2 and A_3) and then by R-tSW (B_2 and B_3). At G2, after the second overpressure jump, the overpressure settles to a constant value of 33.8 kPa, and then starts to decrease due to the expansion fan from the left end, L-rEF. At G3, the pressure decrease, C_3 , after the two jumps, A_3 and B_3 , is caused by the expansion fan from the right end, R-rEF. In the plateau pressure after the second jump, at $t = 65.6$ ms, the contact surface generated in the collision between the incident shocks passes the location. In the pressure history at $x = 3330$ mm (G5), the first and second pressure jumps are due to R-iSW (A_5) and L-tSW (B_5). The pressure decrease at C_5 is due to R-rEF.

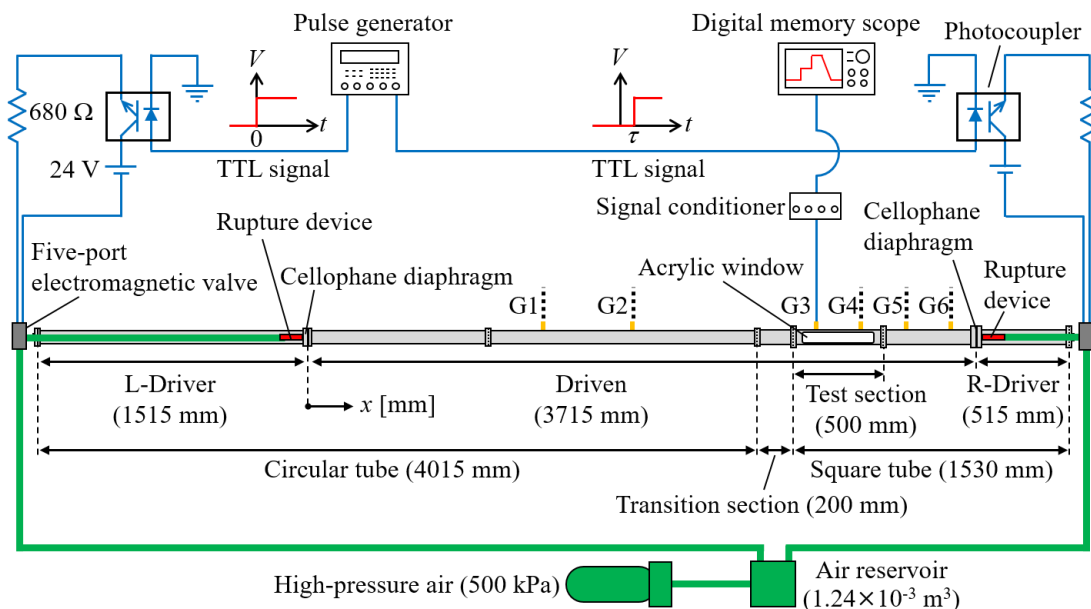


Figure 4.6 Counter-driver shock tube system; pressure transducers, G1 to G6; relative delay time from L-Driver to R-Driver actuations, τ .

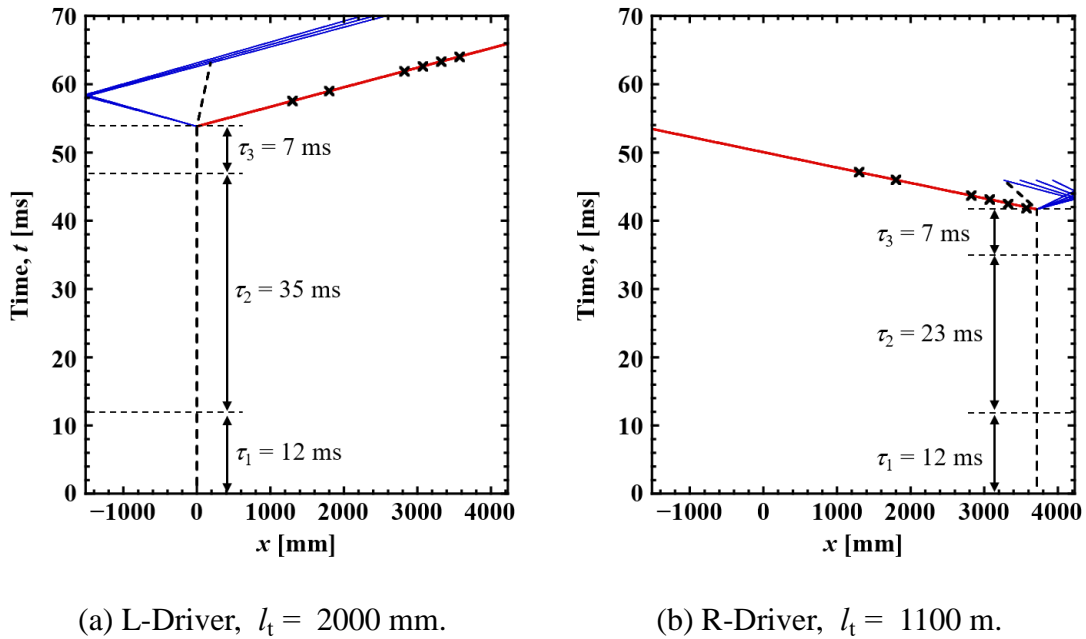


Figure 4.7 Example of $x-t$ diagrams of individual driver operation; solid lines are calculated from ideal shock tube relation; cross symbols are measured.

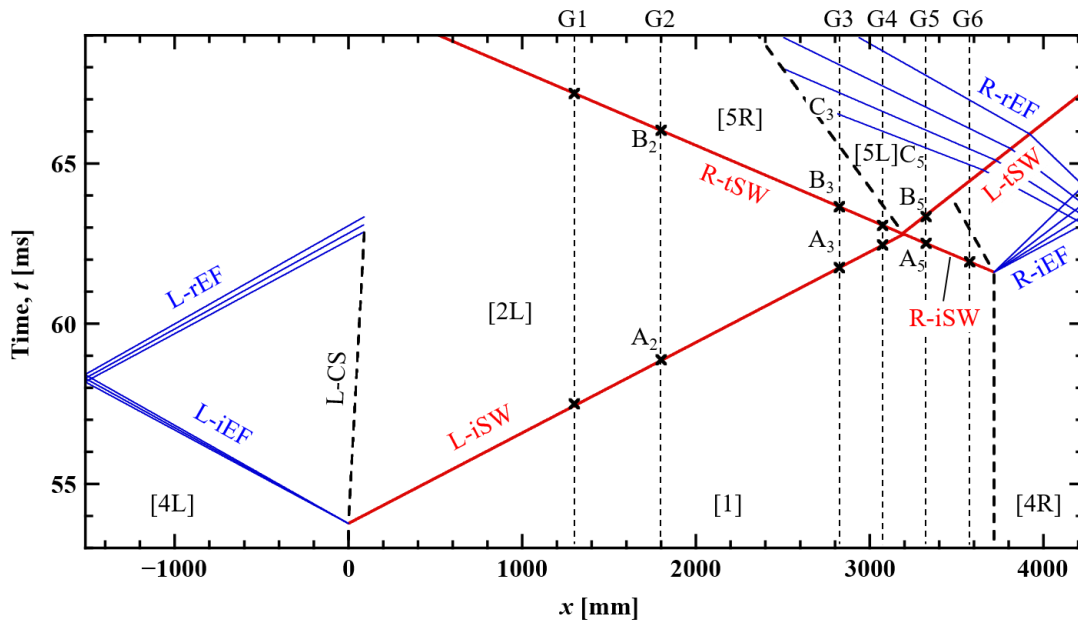


Figure 4.8 Example of $x-t$ diagram of counter-driver operation; $P_{4L} = 43.4$ kPa, $P_1 = 36.9$ kPa, $P_{4R} = 129.3$ kPa; incident and reflected expansion fans, iEF and rEF; the states in the boxes corresponds to those in Fig. 4.1; A, B, C, refer to those in Fig. 4.9; cross symbols are measured; lines are drawn based on the ideal shock tube relation.

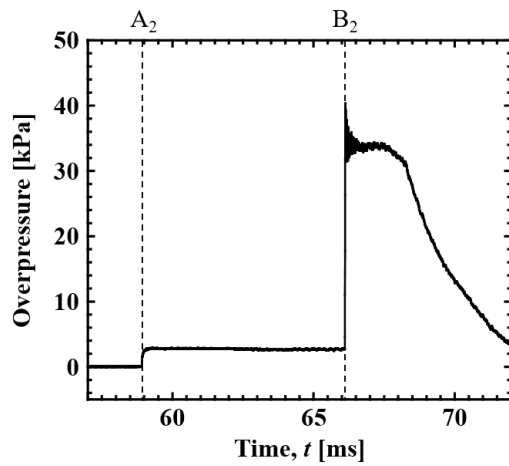
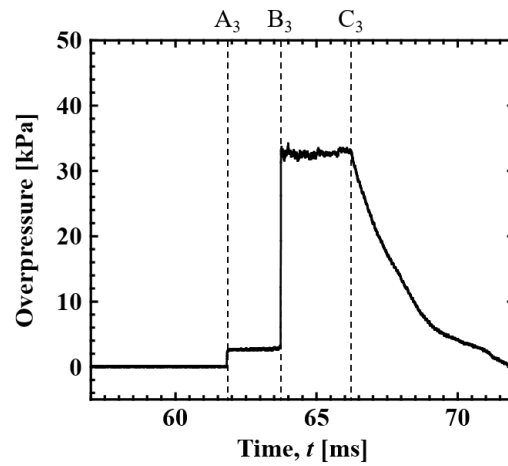
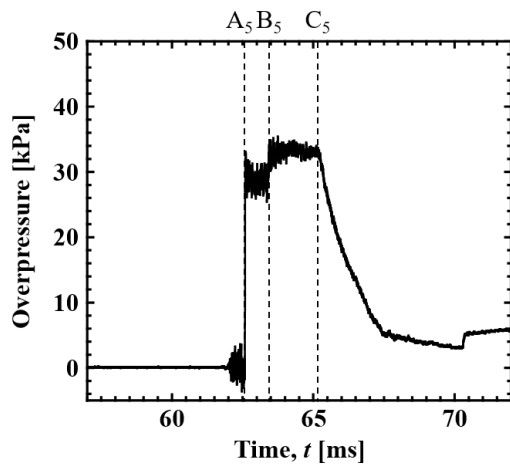
(a) G2 ($x = 1800$ mm)(b) G3 ($x = 2830$ mm)(c) G5 ($x = 3330$ mm)

Figure 4.9 Overpressure histories measured at G2, G3, and G5 in demonstration experiment shown in Fig. 4.8 (A, B, C, refer to those in Fig. 4.8).

4.4.2 120 mm × 120 mm square counter-driver shock tube

For the interaction experiments between planar shock wave and grid turbulence, a large CD-ST was constructed. Fig. 4.10 shows a typical configuration of the shock tube. The CD-ST has a total length of 10.085 m and $120 \times 120 \text{ mm}^2$ square cross section. The cross section was expanded in comparison with the shock tube described in Section 4.4.1 to minimize the effect of the boundary layer developed behind a planar shock wave. The lengths of the L-Driver, the Driven, and the R-Driver sections were 3025 mm, 6040 mm and 1020 mm, respectively. However, the shock tube was composed of a 1000-mm-long tube such that the length of each Driver and Driven section could be adjusted to satisfy experimental conditions. In each Driver section, the active rupture system described in Section 4.3.1 was installed to realize shock wave generation with temporal control. At the test section, a pair of BK7 windows with an effective diameter of 110 mm was set for flow visualization (center of the window at $x = 2470 \text{ mm}$). Figure 4.11 shows the optical system of shadowgraph/Schlieren visualization. A high-speed camera (Phantom v1211, Vision Research Inc.; $256 \text{ pixels} \times 256 \text{ pixels}$, 100 kfps) and a synchronized pulse diode laser (CAVILUX smart, Cavitar Ltd; wavelength 640 nm) were used for the visualization. In some cases of shadowgraph visualization, a half mirror was set on the light pass because the intensity of the laser light source was too high to visualize the shock wave. Piezoelectric pressure transducers (either 113A21, 113B27, or H112A21, PCB Piezotronics Inc.; rise time $1 - 2 \mu\text{s}$) were flush-mounted on the inner top wall of the shock tube for the measurement of local shock speeds and overpressure histories. The porous wall described in Section 4.3.2 was installed at $x = 5020 \text{ mm}$ to form weak planar shock waves in the cases of weak shock wave interaction.

In the interaction experiments between planar shock wave and grid turbulence

described in the following section, a square grid was installed in the shock tube at $x = 2020$ mm to form grid turbulence by disturbing L-PSF. Figure 4.12 shows the configuration of the square grid. The square grid was composed of 5×5 mm² square pillars, which crossed each other at intervals of 25 mm such that the solidity was 30.6%. The outer frame of the square grid was flush-mounted on the inner wall of the shock tube to eliminate the effect of the edge on the characteristics of the grid turbulence. By using the hot-wire anemometer calibrated by the method described in Section 4.3.3, the characteristics of the grid turbulence was obtained under a certain condition. It should be noted that the temperature of the grid turbulence was increased by a reflected shock wave from the grid (Grid-rSW in Fig. 4.13), as mentioned by Xanthos et al. (Xanthos et al., 2002). Therefore, the calibration of the hot-wire anemometer was conducted under the assumption of the temperature behind Grid-rSW. In the case that the mean flow velocity of the grid turbulence, $\overline{u_{2L}}$, was 102 m/s, the rms velocity fluctuation under the assumption of isotropic turbulence, u'_{2L} , was 4.0 m/s and the integral length scale was 11 mm at $x = 2470$ mm, i.e. at the center of the visualization window. Taking the speed of sound behind Grid-rSW as $a_{2r} = 358$ m/s, which was calculated using an ideal shock tube relation, the turbulent Mach number was $M_t = u'_{2L}/a_{2r} \approx 11 \times 10^{-3}$.

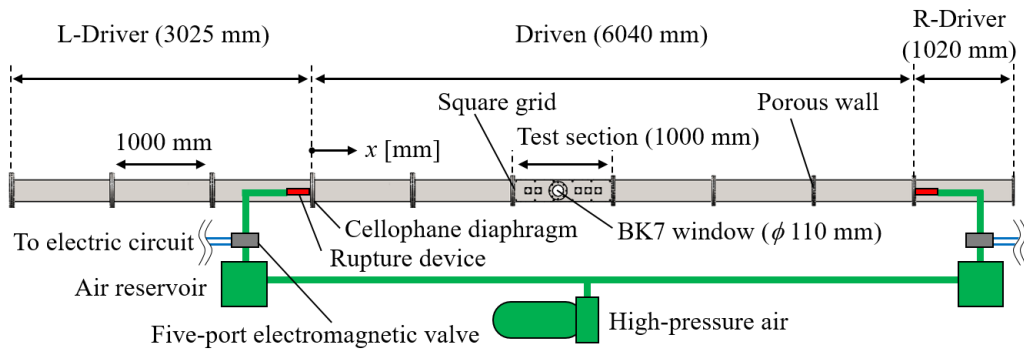


Figure 4.10 120 mm × 120 mm square counter-driver shock tube, electric circuit corresponds to Fig. 4.6.

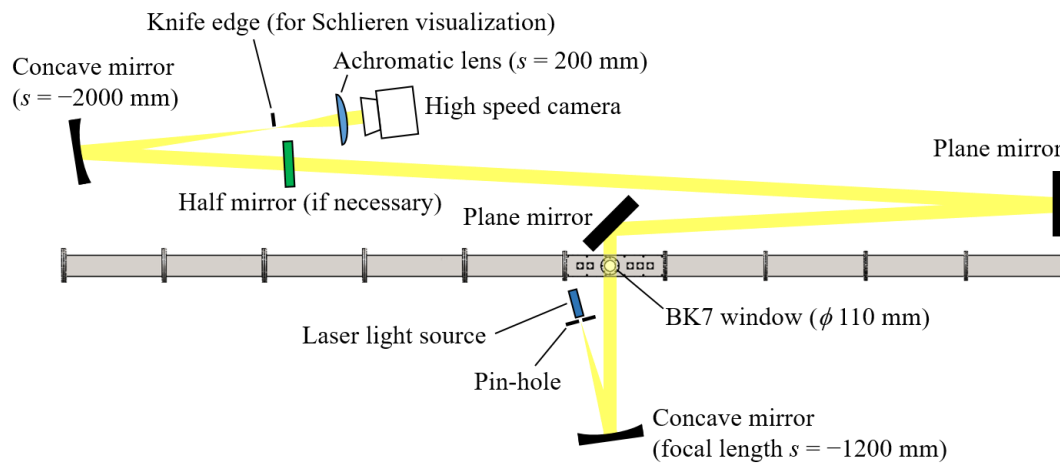


Figure 4.11 Top view of optical system of shadowgraph/Schlieren visualization (shock tube is described in side view to indicate the position of the visualization window).

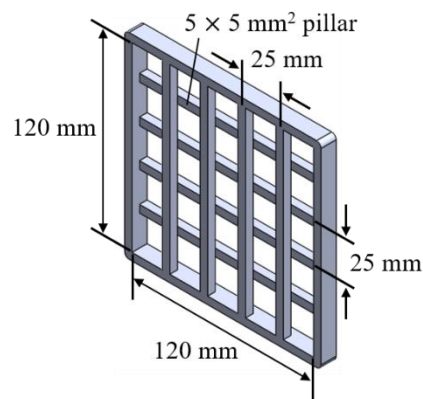


Figure 4.12 Square grid, solidity = 30.6%.

4.5 Interaction between planar shock wave and grid turbulence

4.5.1 Experimental condition

The interaction experiments between planar shock wave and grid turbulence were conducted using the CD-ST described in Section 4.4.2. Figure 4.13 shows a wave diagram under a typical condition of Case 1, where the shock Mach number of R-tSW was $M_s = 1.01$ and the estimated turbulent Mach number was $M_t = 6 \times 10^{-3}$ (see Table 4.1). From the L-Driver, L-iSW propagated to the right with L-PSF behind it. The square grid installed at $x = 2020$ mm disturbed the flow and formed grid turbulence. With an appropriate delay time, R-iSW was generated from R-Driver and propagated to the left. In this case, R-iSW was weakened by the porous wall installed at $x = 5020$ mm and then collided with L-iSW. After the collision of these two incident shock waves, L-tSW and R-tSW formed. R-tSW collided with the front of the grid turbulence at $x = x_{TU}$ and propagated to the left as it interacted with the grid turbulence. In this study, the interaction between R-tSW and the grid turbulence was optically observed at the visualization window, which had a center of $x = 2470$ mm. The interaction length, L_i , was defined as the length between x_{TU} and the center of the window on the shock fixed coordinate.

Table 4.1 shows the experimental conditions for each case. By changing the initial condition, the shock Mach number of R-tSW, M_s , and turbulent Mach number of the grid turbulence, M_t , were manipulated. It should be noted that M_t of these cases were estimated from an assumption: the velocity fluctuation, u'_{2L} , was proportional to the mean flow velocity of L-PSF, $\overline{u_{2L}}$. Under the assumption, u'_{2L} in each condition was estimated from $\overline{u_{2L}}$ obtained by an ideal shock tube relation and $u'_{2L} = 4.0$ m/s at $\overline{u_{2L}} = 102$ m/s,

which was obtained by the hot-wire anemometer as described in Section 4.4.2. In Cases 1 and 3, the porous wall was installed in the shock tube at $x = 5020$ mm to weaken the interacting shock wave. In Case 3, a different type of porous wall was applied (diameter of punched hole, 2 mm; thickness of punched plate, 2 mm; solidity, 74.0%) while the porous wall in Case 1 was that described in Section 4.3.2. Cases 1 and 3 were the cases of the interaction between relatively weak shock wave and relatively strong turbulence, in which the “broken shock” criteria $M_t \gtrsim 0.6(M_s - 1)$, proposed by the numerical study (Larsson et al., 2013), could be satisfied, and Case 2 was vice versa. For each case, the interaction length, L_i , was varied by adjusting the relative delay time of the L- and the R-Drivers.

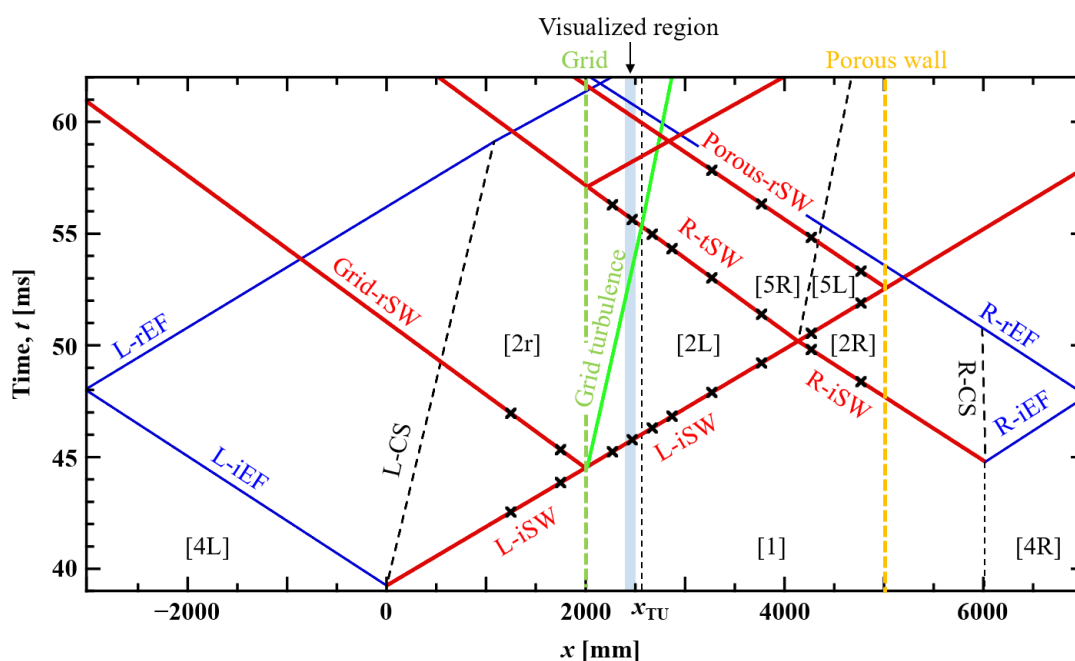


Figure 4.13 Example of $x-t$ diagram of an interaction experiment between planar shock wave and grid turbulence (Case 1, see Table 4.1); $P_{4L} = 68.0$ kPa, $P_1 = 43.0$ kPa, $P_{4R} = 50.0$ kPa; shock Mach number of R-tSW, $M_s = 1.01$; turbulent Mach number, $M_t = 6 \times 10^{-3}$ (estimation); interaction length, $L_i = 108$ mm; solid lines are calculated from an ideal shock tube relation; cross symbols are measured.

Table 4.1 Experimental conditions; turbulent Mach numbers, M_t , were estimated from an assumption of a proportional relationship between $\overline{u_{2L}}$ and u'_{2L} .

		Case 1	Case 2	Case 3
P_{4L} [kPa]		68.0	68.0	310.0
P_1 [kPa]		43.0	43.0	43.0
P_{4R} [kPa]		50.0	99.9	50.0
Porous wall		w/	w/o	w/
R-tSW, M_s [-]		1.01	1.18	1.02
Turbulence	$\overline{u_{2L}}$ [m/s]	50	50	215
	M_t [-]	6×10^{-3}	6×10^{-3}	23×10^{-3}
Visualization		Shadowgraph	Shadowgraph	Schlieren

4.5.2 Side view thickness of shock wave region

Figures 4.14 and 4.15 show the typical shadowgraph images of R-tSW for Cases 1 and 2, which were expected to satisfy and not satisfy the “broken shock” criteria, respectively. The field of view in Fig. 4.14 is relatively dark because a half-mirror was placed in the light pass of the shadowgraph system as described in Fig. 4.11; however, it did not affect the result. Figures 4.14 (a) and 4.15 (a) denote the images before the arrival of the grid turbulence in the field of view: R-tSW propagated to the left against undisturbed L-PSF ($u_{2L} = 50$ m/s). The others show R-tSW interacting with the grid turbulence with the interaction length, L_i . The available maximum L_i varied depending on the experimental conditions, which was restricted by the arrivals of L- and R-EF and Porous-rSW. It is important to note that a shadowgraph image represents the integration of density gradient of the fluid over the entire light pass. When an ideal planar shock wave is visualized by shadowgraph imaging, the density gradient along the shock wave front causes brightness variation on the shadowgraph image.

In the case that R-tSW is a relatively weak condition (Fig. 4.14), the wave front of R-tSW had dark and bright straight lines, which were the features of a planar shock wave in shadowgraph visualization (Fig. 4.14 (a)). In general, the thickness of a shock wave is the order of the mean free path of the molecules; however, it is represented by the width of several pixels when the shock wave is recorded by shadowgraph/Schlieren visualization using a digital camera. Hereafter, the region where these lines exist, which represent the density gradient due to the shock wave, is referred to as a “shock wave region.” During the interaction with the grid turbulence with the interaction length of 108 mm, the shock wave region expanded into the left and right, and its width varied locally (Fig. 4.14 (b)). In the shock wave region, more than two lines, which indicated density gradient, could be observed. Sometimes, it became difficult to identify the edge of the shock wave region because these lines were locally dispersed. These results suggested that the wave front of R-tSW “wrinkled” or was locally “broken”: the integration of the local density gradient due to the wrinkled wave front was represented as the shock wave region with a certain width on the shadowgraph images. These effects became stronger as L_i increased (Fig. 4.14 (c)). However, in the case that R-tSW was relatively strong (Fig. 4.15), the clear modulation shown in Fig. 4.14 could not be observed. When R-tSW interacted with the grid turbulence for equivalent distances to Fig. 4.14, the features of R-tSW were similar to a planar shock wave, although slight fluctuations, which represented small, local deformations of the wave front, were observed in the shock wave regions. The similar phenomenon was reported in the previous study, in which the wave front of a planar shock wave of $M_s \approx 1.2$ fluctuated as a result of the interaction with grid turbulence of $\bar{u} \approx 100$ m/s (Dosanjh, 1956). Figure 4.16 shows the Schlieren images in the case of the interaction with extremely strong grid turbulence. In this case, a relatively

stronger modulation of the shock wave was obtained: the shock wave almost collapsed and disappeared from the center of the image (Fig. 4.16 (c)).

To reveal the relationship between the interaction length and the modulation of the shock wave, the side view thickness of the shock wave region was evaluated using image processing. Based on the background-subtracted shadowgraph images, the distribution of brightness gradient of each pixel on the image was calculated using the Sobel filter (Sobel, 1968). Thereafter, the edge of the gradient was detected using the Canny edge detector (Canny, 1986) to obtain the outline of the side view thickness of the shock wave region. Figure 4.17 shows the relationship between the interaction length, L_i , and the average of the side view thickness of the shock wave region. This processing was done in the vertical range from 64 pixels to 191 pixels. It should be noted that the data at $L_i = -230$ mm represent the average of the side view thickness of R-iSW, which propagated in the stationary gas before the arrival of L-iSW with an equivalent shock Mach number to each case. In the case of a relatively weak shock wave (Fig. 4.17 (a)), the average of the side view thickness of the shock wave region was almost constant for $L_i < 0$, which was before the interaction with the grid turbulence. As mentioned above, a shock wave recorded by shadowgraph visualization has a finite thickness on shadowgraph images; therefore, the average of the thickness was not zero even before the interaction. After the interaction ($L_i > 0$), the average of the side view thickness tended to become larger with increasing L_i . It clearly indicated a correlation between the modulation of the wave front and the interaction length. In contrast, in the case of a relatively strong shock wave (Fig. 4.17 (b)), the effect of the turbulence interaction on the shock wave was relatively small because the average of the side view thickness hardly varied before and after the interaction. One of the possible reasons why the errors increased after the interaction is

the fluctuation in the shock wave region. As shown in Fig. 4.15, the shock wave region slightly fluctuated as a result of the interaction with the grid turbulence even in the case that R -tSW was relatively strong. When the side view thickness of the shock wave region was integrated, the fluctuation in the shock wave region appeared as the error in Fig. 4.17 (b). However, the result indicated that the fluctuation in the shock wave region was not enhanced by the interaction, and the shock wave front remained almost planar. This tendency that the magnitude of the shock wave modulation depended on the relative strength of the shock wave was consistent with the results obtained in the previous studies using direct numerical simulation (Lee et al., 1993; Larsson and Lele, 2009; Larsson et al., 2013).

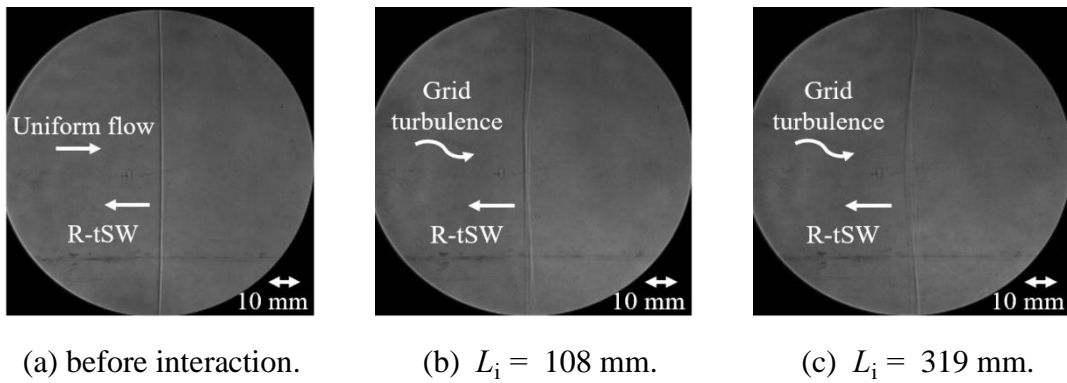


Figure 4.14 Shadowgraph images of Case 1; $M_s = 1.01$, $M_t = 6 \times 10^{-3}$ (estimation), “broken shock” criteria was satisfied; interaction length, L_i .

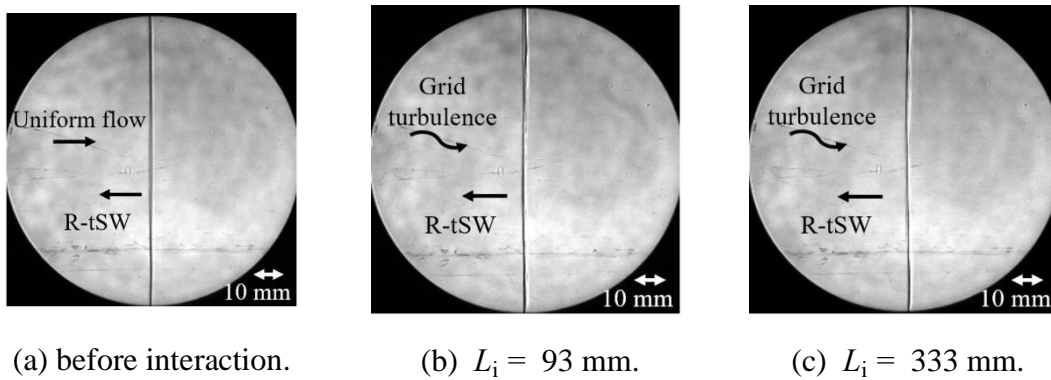


Figure 4.15 Shadowgraph images of Case 2; $M_s = 1.18$, $M_t = 6 \times 10^{-3}$ (estimation), “broken shock” criteria was not satisfied; interaction length, L_i .

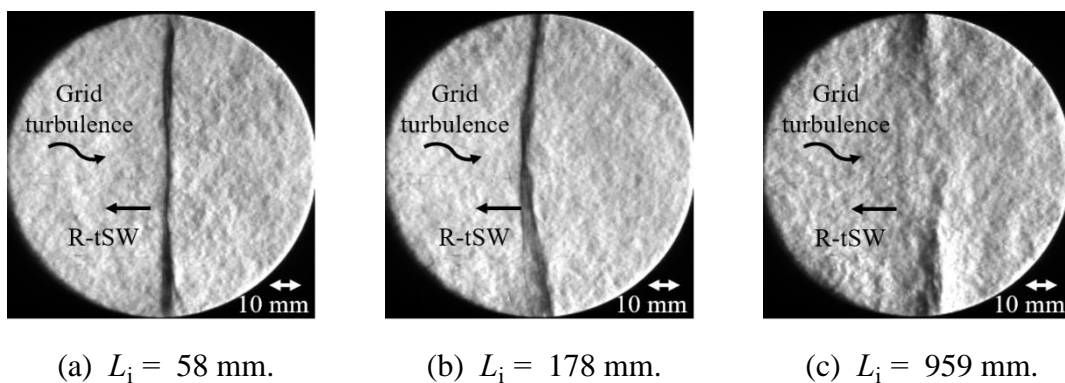
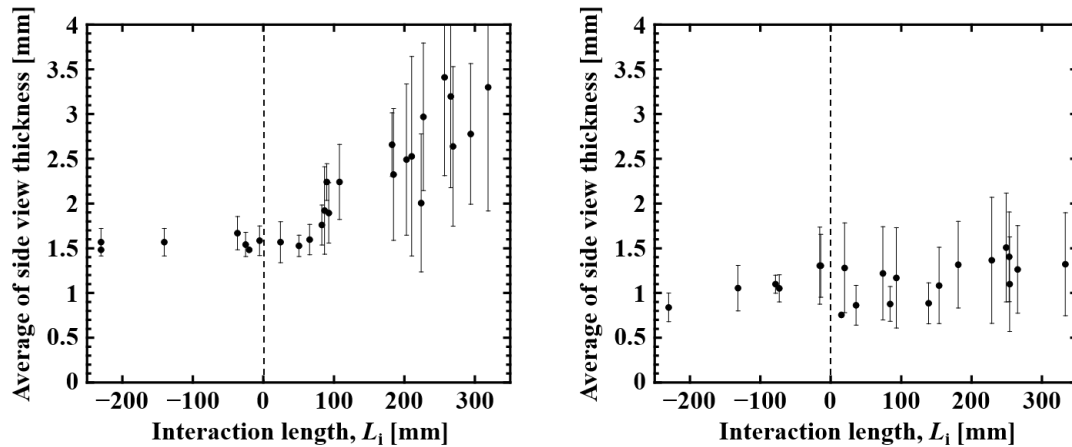


Figure 4.16 Schlieren images of Case 3; $M_s = 1.02$, $M_t = 23 \times 10^{-3}$ (estimation), “broken shock” criteria was satisfied; interaction length, L_i .



(a) Case 1 ($M_s = 1.01$), “broken shock” criteria was satisfied. (b) Case 2 ($M_s = 1.18$), “broken shock” criteria was not satisfied.

Figure 4.17 Relationship between interaction length, L_i , and average of side view thickness of shock wave region; $M_t = 6 \times 10^{-3}$ (estimation).

4.6 Summary of this chapter

In this chapter, a counter-driver shock tube (CD-ST) was developed and interaction experiments between planar shock wave and grid turbulence were conducted using the CD-ST.

- An active rupture system using cellophane diaphragm and pneumatic cylinder was developed. The operation demonstration of the CD-ST was successfully conducted using the active rupture system. The uncertainty in determining the location of the interaction was better than 1/169 of the whole shock tube length, which was small enough for the CD-ST. The system was applied to a 120 mm \times 120 mm square CD-ST.
- A method to generate a weak planar shock wave in a shock tube was developed. By attenuating a planar shock wave using a porous wall which was composed of layers of rigid punched plates, a weak planar shock wave, with the shock Mach number

$M_s = 1.01$, was produced.

- A calibration method of hot-wire anemometer for measurement of compressible flow was established. Assuming a constant shock Mach number in a shock tube, a calibration curve at a certain temperature was obtained by varying the mass flux, ρu .
- Collapse of the wave front of a planar shock wave caused by the interaction with grid turbulence was demonstrated using the CD-ST. In the case that the interacting shock wave was relatively weak compared to the grid turbulence, a significant modulation on the shock wave occurred: the average of the side view thickness of the shock wave region increased with the interaction length, and the shock wave even disappeared under a specific condition. However, in the case of a relatively strong shock wave, this modulation was comparatively small.

Chapter 5

Conclusions

In the present thesis, the modulations of a shock wave front and the pressure field behind the shock wave when local disturbance or turbulence acts on the shock waves were investigated. In each chapter, the various types of effects on shock waves were experimentally evaluated by changing the characteristics of the disturbances that interacted with the shock waves.

In Chapter 2, the effects of local density/temperature and velocity disturbance on the shock wave-boundary layer interaction region were investigated. In this study, the shock wave naturally oscillated on a laboratory coordinate system upon the interaction with the boundary layer. Local disturbance artificially generated by pulsed laser energy deposition was supplied to the shock wave-boundary layer interaction region. In the case without local disturbance (basic flow), broad oscillation spectra of the shock wave were observed. In the case with the local disturbance, the oscillation frequency of the shock wave was modulated: when the frequency of the local disturbance was 30 kHz and lower, the oscillation spectra of the shock wave had a strong peak at the repetitive frequency of the disturbance. When the frequency of the disturbance was 40 kHz and higher, the oscillation spectra modulated toward a much lower domain, while the spectra around the frequency of the local disturbance vanished.

In Chapter 3, the overpressure modulation behind a blast wave by a local turbulent flow was investigated. In this chapter, the element of disturbance was velocity fluctuation

and it interacted with the weak blast wave that propagated over a relatively long distance, on the order of several meters in the field, to weaken the shock wave and minimize the curvature effects. The pressure field behind the blast wave was modulated by the interaction with the velocity disturbance: the pressure waveforms obtained by multipoint measurements varied locally, even in the same shot. The peak overpressure was randomly varied for each shot and at each measured point by the interaction. Thus, the standard deviation of the peak overpressure increased by 7 times compared to that without the interaction.

Chapter 4 described the development of a counter-driver shock tube to investigate the interaction between a planar shock wave and grid turbulence. A new facility, called a “counter-driver shock tube,” in which a planar shock wave-grid turbulence interaction can be conducted in arbitrary conditions, was developed. Shock wave generation with temporal control was achieved by an active rupture system using a pneumatic cylinder, and an operational test of the counter-driver shock tube was conducted. Using this facility, the effects of quasi-isotropic velocity disturbance, i.e., grid turbulence, on the wave front of a planar shock wave was investigated. When the shock wave was relatively weak compared to the grid turbulence, the side view thickness of the shock wave region increased by the interaction length, and the shock wave even disappeared under a specific condition. However, in the case of a relatively strong shock wave, the modulation of the shock wave was comparatively small.

In summary, the impact of the interactions with disturbances on a shock wave was evaluated. (1) The disturbances could modulate the shock wave: when density/temperature and velocity disturbance repetitively acted on a shock wave, which naturally had instability, the interaction with the disturbance induced a regular modulation

of the shock wave front. When velocity disturbance contained randomness, the shock wave front and the pressure field behind it were randomly modulated by the interaction with the disturbance. (2) In the case that the disturbance was velocity disturbance, the magnitude of the modulation depended on the relative strength of the shock wave to the velocity fluctuation: the wave front of a relatively weak shock wave was strongly modulated by the interaction, and there existed a correlation between the magnitude of the modulation and the interaction length.

However, the effects of the interactions on the disturbances were beyond the scope of the present thesis, although the interactions are generally mutual. Not only the shock wave but also the disturbances should be modulated by the interactions, as reported in previous studies, for example on density/temperature disturbance (Adelgren et al., 2005; Kim et al., 2011) and turbulence (Agui et al., 2005; Kitamura et al., 2017). The disturbances following the interactions have the potential to affect the pressure field behind the shock wave, therefore, further investigations are required to reveal the mechanisms of the mutual interactions.

References

- Adelgren, R. G., Yan, H., Elliott, G. S., Knight, D. D., Beutner, T. J., and Zheltovodov, A. A., "Control of Edney IV Interaction by Pulsed Laser Energy Deposition," *AIAA Journal*, vol. 43, No. 2, pp. 256-269, 2005.
- Agui, J. H., Briassulis, G., and Andreopoulos, Y., "Studies of interactions of a propagating shock wave with decaying grid turbulence: velocity and vorticity fields," *Journal of Fluid Mechanics*, vol. 524, pp. 143-195, 2005.
- Barbosa, F. J., and Skews, B. W., "Experimental confirmation of the von Neumann theory of shock wave reflection transition," *Journal of Fluid Mechanics*, vol. 472, pp. 263-282, 2002.
- Barre, S., Alem, D., and Bonnet, J. P., "Experimental Study of a Normal Shock/Homogeneous Turbulence Interaction," *AIAA Journal*, vol. 34, No. 5, pp. 968-974, 1996.
- Barre, S., Alem, D., and Bonnet, J. P., "Reply by the Authors to H. S. Ribner," *AIAA Journal*, vol. 36, No. 3, p.495, 1998.
- Barter, J. W., and Dolling, D. S., "Reduction of Fluctuating Pressure Loads in Shock/Boundary-Layer Interactions Using Vortex Generators," *AIAA Journal*, vol. 33, No. 10, pp. 1842-1849, 1995.
- Barter, J. W., and Dolling, D. S., "Reduction of Fluctuating Pressure Loads in Shock/Boundary-Layer Interactions Using Vortex Generators: Part 2," *AIAA Journal*, vol. 34, No. 1: Technical Notes, pp.195-197, 1996.
- Bass, H. E., Layton, B. A., and Bolen, L. N., "Propagation of medium strength shock

- waves through the atmosphere,” *Journal of the Acoustical Society of America*, vol. 82 (1), pp. 306-310, 1987.
- Beresh, S. J., Clemens, N. T., and Dolling, D. S., “Relationship Between Upstream Turbulent Boundary-Layer Velocity Fluctuations and Separation Shock Unsteadiness,” *AIAA Journal*, vol. 40, No. 12, pp. 2412-2422, 2002.
- Briassulis, G., Honkan, A., Andreopoulos, J., Watkins, C. B., “Application of hot-wire anemometry in shock-tube flows,” *Experiments in Fluids*, vol. 19 (1), pp. 29-37, 1995.
- Britan, A., Igra, O., Ben-Dor, G., and Shapiro, H., “Shock wave attenuation by grids and orifice plates,” *Shock Waves*, vol. 16 (1), pp. 1-15, 2006.
- Bushnell, D. M., “Aircraft drag reduction—a review,” *Proceedings of the Institution of Mechanical Engineers, Part G: Journal of Aerospace Engineering*, vol. 217 (1), pp. 1-18, 2003.
- Canny, J., “A Computational Approach to Edge Detection,” *IEEE Transactions on Pattern Analysis and Machine Intelligence*, vol. PAMI-8, No. 6, pp. 679-698, 1986.
- Chafi, M. S., Karami, G., and Ziejewski, M., “Biomechanical Assessment of Brain Dynamic Responses Due to Blast Pressure Waves,” *Annals of Biomedical Engineering*, vol. 38, No. 2, pp. 490-504, 2010.
- Clemens, N. T., and Narayanaswamy, V., “Low-Frequency Unsteadiness of Shock Wave/Turbulent Boundary Layer Interactions,” *Annual Review of Fluid Mechanics*, vol. 46, pp. 469-492, 2014.
- Cozzani, V., and Salzano, E., “Threshold values for domino effects caused by blast wave interaction with process equipment,” *Journal of Loss Prevention in the Process Industries*, vol. 17 (6), pp. 437-447, 2004.

- Dolling, D. S., "Fifty Years of Shock-Wave/Boundary-Layer Interaction Research: What Next?," *AIAA Journal*, vol. 39, No. 8, pp. 1517-1531, 2001.
- Dosanjh, D. S., "Interaction of grids with traveling shock waves," *NACA TN-3680*, 1956.
- Dosanjh, D. S., and Weeks, T. M., "Interaction of a Starting Vortex as Well as a Vortex Street with a Traveling Shock Wave," *AIAA Journal*, vol. 3, No. 2, pp. 216-223, 1965.
- Dupont, P., Haddad, C., and Debieve, J. F., "Space and time organization in a shock-induced separated boundary layer," *Journal of Fluid Mechanics*, vol. 559, pp. 255-277, 2006.
- Dussauge, J.-P., Dupont, P., and Debieve, J. F., "Unsteadiness in shock wave boundary layer interactions with separation," *Aerospace Science and Technology*, vol. 10 (2), pp. 85-91, 2006.
- Erdem, E., Kontis, K., and Yang, L., "Steady energy deposition at Mach 5 for drag reduction," *Shock Waves*, vol. 23 (4), pp. 285-298, 2013.
- Erengil, M. E., and Dolling, D. S., "Unsteady Wave Structure near Separation in a Mach 5 Compression Ramp Interaction," *AIAA Journal*, vol. 29, No. 5, pp. 728-735, 1991a.
- Erengil, M. E., and Dolling, D. S., "Correlation of Separation Shock Motion with Pressure Fluctuations in the Incoming Boundary Layer," *AIAA Journal*, vol. 29, No. 11, pp. 1868-1877, 1991b.
- Estruch, D., MacManus, D. G., Richardson, D. P., Lawson, N. J., Garry, K. P., and Stollery, J. L., "Experimental study of unsteadiness in supersonic shock-wave/turbulent boundary-layer interactions with separation," *Aeronautical Journal*, vol. 144, No. 1155, pp. 299-308, 2010.

- Friedlander, F. G., "The diffraction of sound pulses I. Diffraction by a semi-infinite plane," Proceedings of the Royal Society of London A: Mathematical, Physical and Engineering Sciences, vol. 186 (1006), pp. 322–344, 1946.
- Furukawa, D., Aoki, Y., Iwakawa, A., and Sasoh, A., "Moderation of near-field pressure over a supersonic flight model using laser-pulse energy deposition," Physics of Fluids, vol. 28 (5), 051701, 2016.
- Ganapathisubramani, B., Clemens, N., T., and Dolling, D. S., "Low-frequency dynamics of shock-induced separation in a compression ramp interaction," Journal of Fluid Mechanics, vol. 636, pp. 397-425, 2009.
- Girgis, I. G., Shneider, M. N., Macheret, S. O., Brown, G. L., and Miles, R. B., "Steering Moments Creation in Supersonic Flow by Off-Axis Plasma Heat Addition," Journal of Spacecraft and Rockets, vol. 43, No. 3, pp.607-613, 2006.
- Glass, I. I., and Sislian, J. P., "Nonstationary Flows and Shock Waves," Clarendon Press, Oxford, 1994.
- Gnani, F., Zare-Behtash, H., and Kontis, K., "Pseudo-shock waves and their interactions in high-speed intakes," Progress in Aerospace Science, vol. 82, pp. 36-56, 2016.
- Goel, M. D., Matsagar, V. A., Gupta, A. K., and Marburg, S., "An Abridged Review of Blast Wave Parameters," Defence Science Journal, vol. 62, No. 5, pp. 300-306, 2012.
- Held, M., "Blast Waves in Free Air," Propellants, Explosives, Pyrotechnics, vol. 8 (1), pp. 1-7, 1983.
- Hickman, R. S., Farrar, L. C., and Kyser, J. B., "Behavior of burst diaphragm in shock tubes," Physics of Fluids, vol. 18 (10), pp. 1249-1252, 1975.
- Hollingsworth, M. A., Richards, E. J., "A Schlieren Study of the Interaction between a

- Vortex and a Shock Wave in a Shock Tube,” Aeronautical Research Council, Report 17985, Fluid Motion Sub-Committee 2323, 1955.
- Hong, Y., Wang, D., Li, Q., and Ye, J., “Interaction of single-pulse laser energy with bow shock in hypersonic flow,” *Chinese Journal of Aeronautics*, vol. 27 (2), pp. 241-247, 2014.
- Honkan, A., and Andreopoulos, J., “Rapid compression of grid-generated turbulence by a moving shock wave,” *Physics of Fluids A: Fluid Dynamics*, vol. 4 (11), pp. 2562–2572, 1992.
- Honkan, A., Watkins, C. B., and Andreopoulos, J., “Experimental Study of Interactions of Shock Wave With Free-Stream Turbulence,” *Journal of Fluids Engineering*, vol. 116 (4), pp. 763-769, 1994.
- Hubbard, H. H., Maglieri, D. J., Huckel, V., and Hilton, D. A., “Ground Measurements of Sonic-Boom Pressures for the Altitude Range of 10,000 to 75,000 feet,” NASA TR R-198, 1964.
- Ikui, T., Matsuo, K., "Investigation of the Aerodynamic Characteristics of the Shock Tubes (Part 1, The effects of Tube Diameter on the Tube Performance)," *Bulletin of Japan Society of Mechanical Engineers*, vol. 12 (52), pp. 774-782, 1969.
- Im, S.-K., Wermer, L., Baccarella, D., Liu, Q., McGann, B., and Do, H., “Ramp Separation Response to Laser-Induced Breakdown Disturbed Boundary Layer at Mach 4.5,” *Proceedings of 55th AIAA Aerospace Science Meeting*, San Diego, California, USA, 4-8 January, 2016.
- Inokuma, K., Watanabe, T., Nagata, K., Sasoh, A., and Sakai, Y., “Finite response time of shock wave modulation by turbulence,” *Physics of Fluids*, vol. 29 (5), 051701, 2017.

- Inoue, H., Ishida, H., Kishimoto, K., and Shibuya, T., “Measurement of Impact Load by using an Inverse Analysis Technique* (Comparison of Methods for Estimating the Transfer Function and its Application to the Instrumented Charpy Impact Test),” Japan Society of Mechanical Engineers International Journal Series 1: Solid Mechanics, Strength of Materials, col. 34 (4), pp. 453-458, 1991.
- Iwakawa, A., Shoda, T., Majima, R., Pham, H. S., and Sasoh, A., “Mach Number Effect on Supersonic Drag Reduction using Repetitive Laser Energy Depositions over a Blunt Body,” Transactions of the Japan Society for Aeronautical and Space Sciences, vol. 60, No. 5, pp. 303-311, 2017.
- Kane, E. J., “Some Effects of the Atmosphere on Sonic Boom,” NASA SP-147, pp. 49-63, 1967.
- Keller, J., and Merzkirch, W., “Interaction of a normal shock wave with a compressible turbulent flow,” Experiments in Fluids, vol. 8 (5), pp. 241-248, 1990.
- Kim, J.-H., Matsuda, A., and Sasoh, A., “Interactions among baroclinically-generated vortex rings in building up an acting spike to a bow shock layer,” Physics of Fluids, 23 (2), 021703, 2011.
- Kim, J.-H., Sasoh, A., and Matsuda, A., “Modulations of a weak shock wave through a turbulent slit jet.” Shock Waves, vol. 20 (4), pp. 339-345, 2010.
- Kitagawa, K., Takayama, K., and Yasuhara, M., “Attenuation of shock waves propagating in polyurethane foams,” Shock Waves, vol. 15 (6), pp. 437-445, 2006.
- Kitamura, T., Nagata, K., Sakai, Y., Sasoh, A., and Ito, Y., “Changes in divergence-free grid turbulence interacting with a weak spherical shock wave,” Physics of Fluids, vol. 29 (6), 065114, 2017.
- Kleine, H., Timofeev, E., and Takayama, K., “Laboratory-scale blast wave phenomena –

- optical diagnostics and applications,” *Shock Waves*, vol. 14 (5-6), pp. 343-357, 2005.
- Landau, L. D., and Lifshitz, E. M., “Fluid Mechanics, second edition: Volume 6 (Course of Theoretical Physics),” Butterworth-Heinemann, Oxford, 1987.
- Larsson, J., Bermejo-Moreno, I., and Lele, S. K., “Reynolds- and Mach-number effects in canonical shock-turbulence interaction,” *Journal of Fluid Mechanics*, vol. 717, pp. 293-321, 2013.
- Larsson, J., and Lele, S. K., “Direct numerical simulation of canonical shock/turbulence interaction,” *Physics of Fluids*, vol. 21 (12), 126101, 2009.
- Lee, S., Lele, S. K., and Moin, P., “Direct numerical simulation of isotropic turbulence interacting with a weak shock wave,” *Journal of Fluid Mechanics*, vol. 251, pp. 533-562, 1993.
- Lipkens, B., and Blackstock, D. T., “Model experiment to study sonic boom propagation through turbulence. Part I: General results,” *Journal of the Acoustical Society of America*, vol. 103 (1), pp. 148-158, 1998.
- Maglieri, D. J., Bobbitt, P. J., Plotkin, K. J., Shepherd, K. P., Coen, P. G., and Richwine, D. M., “SONIC BOOM, Six Decades of Research,” NASA/SP-2014-622, 2014.
- McCormick, D. C., “Shock/Boundary-Layer Interaction Control with Vortex Generators and Passive Cavity,” *AIAA Journal*, vol. 31, No. 1, pp. 91-96, 1993.
- Miller, C. G., “Expansion Tunnel Performance with and without an Electromagnetically Opened Tertiary Diaphragm,” *AIAA Journal*, vol. 15, No. 7, Technical Note, pp. 1045-1047, 1977.
- Moochhala, S. M., Shirhan, M, Lu, J., Teng, C.-H., and Greengrass, C., “Neuroprotective Role of Aminoguanidine in Behavioral Changes after Blast Injury,” *Journal of*

- Trauma: Injury, Infection, and Critical Care, vol. 56, No. 2, pp. 393-403, 2004.
- Narayanaswamy, V., Raja, L. L., and Clemens, N. T., "Control of unsteadiness of a shock wave/turbulent boundary layer interaction by using a pulsed-plasma-jet actuator," Physics of Fluids, vol. 24 (7), 076101, 2012.
- Needham, C. E., "Blast Waves, Shock Wave and high Pressure Phenomena," Springer, Berlin, Heidelberg, 2010.
- Oertel, H., "Stossrohre," Springer-Verlag, Wien-New York, 1966.
- Oguchi, H., Funabiki, K., Sato, S., and Hatakeyama, M., "A free-flight experiment of projectiles ranging from high subsonic to high supersonic Mach numbers," Shock Waves, vol. 1 (3), pp. 233-236, 1991.
- Osuka, T., Erdem, E., Hasegawa, N., Majima, R., Tamba, T., Yokota, S., Sasoh, A., and Kontis, K., "Laser energy deposition effectiveness on shock-wave boundary-layer interactions over cylinder-flare combinations," Physics of Fluids, vol. 26 (9), 096103, 2014.
- Pirozzoli, S., and Grasso, F., "Direct numerical simulation of impinging shock wave/turbulent boundary layer interaction at $M = 2.25$," Physics of Fluids, vol. 18 (6), 065113, 2006.
- Plurad, C. D., "Blast injury," Military Medicine, vol. 176 (3), pp. 276-282, 2011.
- Potapkin, A. V., and Moskvichev, D. Yu., "Reduction of the sonic boom level by heating the flow in front of the body," Shock Waves, vol. 24 (4), pp. 429-437, 2014.
- Quan, S., Hong, L. Y., Wei, C., BangQin, C., Jun, L., and Hui, D., "Shock wave-boundary layer interactions control by plasma aerodynamic actuation," Science China Technological Sciences, vol. 57 (7), pp. 1335-1341, 2014.
- Ribner, H. S., Morris, P. J., and Chu, W. H., "Laboratory simulation of development of

- superbooms by atmospheric turbulence,” *Journal of the Acoustical Society of America*, vol. 53, No. 3, pp. 926-928, 1973.
- Roach, P. E., “The generation of nearly isotropic turbulence by means of grids,” *International Journal of Heat and Fluid Flow*, vol. 8 (2), pp. 82-92, 1987.
- Saad, M. R., Zare-Behtash, H., Che-Idris, A., and Kontis, K., “Micro-ramps for hypersonic flow control,” *Micromachines*, vol. 3 (2), pp. 364-378, 2012.
- Sasoh, A., Harasaki, T., Kitamura, T., Takagi, D., Ito, S., Matsuda, A., Nagata, K., and Sakai, Y., “Statistical behavior of post-shock overpressure past grid turbulence,” *Shock Waves*, vol. 24 (5), pp. 489-500, 2014.
- Sasoh, A., Takahashi, T., Watanabe, K., Torikai, H., and Yang, Q. S., "Shock-Tube Operation with Laser-Beam-Induced Diaphragm Rupture," *AIAA Journal*, vol. 44, No. 5, Technical Notes, pp. 1110-1112, 2006.
- Satheesh, K., and Jagadeesh, G., “Experimental investigation on the effect of energy deposition in hypersonic blunt body flow field,” *Shock Waves*, vol. 18, pp. 53-70, 2008.
- Schulein, E., and Zheltovodov, A., “Effect of steady flow heating by arc discharge upstream of non-slender bodies,” *Shock Waves*, vol. 21 (4), pp. 383-396, 2011.
- Simpson, C. J. S. M., Chandler, T. R. D., and Bridgman, K. B., "Effect on Shock Trajectory of the Opening Time of Diaphragms in a Shock Tube," *Physics of Fluids*, vol. 10 (9), pp. 1894-1896, 1967.
- Sobel, I., “An Isotropic 3×3 Image Gradient Operator,” Presented at Sanford Artificial Intelligence Project, 1968.
- Souverain, L. J., and Debieve, J.-F., “Effect of air jet vortex generators on a shock wave boundary layer interaction,” *Experiments in Fluids*, vol. 49 (5), pp. 1053-1064,

2010a.

Souverein, L. J., Dupont, P., Debieve, J.-F., Dussauge, J.-P., Oudheusden, Bas W., and Scarano, F., "Effect of Interaction Strength on Unsteadiness in Turbulent Shock-Wave-Induced Separations," *AIAA Journal*, vol. 48, No. 7, pp. 1480-1493,

2010b.

Sperber, D., Eckel, H.-A., Steimer, S., and Fasoulas, S., "Objectives of Laser-Induced Energy Deposition for Active Flow Control," *Contributions to Plasma Physics*, vol. 52, No. 7, pp. 636-643, 2012.

Strack, W. C., and Morris, S. J., "The Challenges and Opportunities of Supersonic Transport Propulsion Technology," NASA-TM-100921, 1988.

Ukai, T., Ohtani, K., and Obayashi, S., "Turbulent jet interaction with a long rise-time pressure signature," *Applied Acoustics*, vol. 114, pp. 179-190, 2016.

Ullah, A., Ahmad, F., Jang, H.-W., Kim, S.-W., and Hong, J.-W., "Review of Analytical and Empirical Estimations for Incident Blast Pressure," *KSCE Journal of Civil Engineering*, vol. 21 (6), pp. 2211-2225, 2017.

Wang, J., Li, Y., Cheng, B., Su, C., Song, H., and Wu, Y., "Effects of plasma aerodynamic actuation on oblique shock wave in a cold supersonic flow," *Journal of Physics D: Applied Physics*, vol. 42, No. 16, 165503, 2009.

Webb, N., Clifford, C., and Samimy, M., "Control of oblique shock wave/boundary layer interaction using plasma actuators," *Experiments in Fluids*, vol. 54, 1545, 2013.

White, D. R., "Influence of diaphragm opening time on shock-tube flows," *Journal of Fluid Mechanics*, vol. 4 (6), pp. 585-599, 1958.

Wilcox, D. J., "Numerical Laplace transformation and inversion," *International Journal of Engines*, vol. 15 (3), pp. 247-265, 1978.

- Xanthos, S., Briassulis, G., and Andreopoulos, Y., "Interaction of Decaying Freestream Turbulence with a Moving Shock Wave: Pressure Field," *Journal of Propulsion and Power*, vol. 18 (6), pp. 1289-1297, 2002.
- Yang, J., Onodera, O., and Takayama, K., "Design and Performance of a Quick Opening Shock Tube Using Rubber Membrane for Weak Shock Wave Generation," *Transactions of the Japan Society of Mechanical Engineers Series B*, vol. 60 (570), pp. 473-478, 1994 (in Japanese).
- Yang, J., Sasoh, A., and Takayama, K., "The reflection of a shock wave over a cone," *Shock Waves*, vol. 6 (5), pp. 267-273, 1996.